207500-7-T

Technical Report

MODULATION TRANSFER FUNCTION ANALYSIS OF KELVIN WAKES AND AMBIENT WAVE IMAGES

D. LYZENGA
N. MALINAS
J. BURNS

September 1991

Office of Naval Research
800 N. Quincy Street
Arlington, VA 22217-5000
Scientific Officer: Dr. David H. Johnson
Contract No.: N00014-88-C-0355

ERIM P.O. Box 134001
Ann Arbor, MI 48113-4001

REPORT DOCUMENTATION PAGE

Form Approved
OMB No. 0704-0188

1. AGENCY USE ONLY (Leave blank)	2. REPORT DATE	3. REPORT TYPE AND DATES COVERED
	September 1991	Technical 10/1/90 - 9/30/91

4. TITLE AND SUBTITLE
Modulation Transfer Function Analysis of Kelvin Wakes and Ambient Wave Images

5. FUNDING NUMBERS
N00014-88-C-0355

6. AUTHOR(S)
D. Lyzenga, N. Malinas and J. Burns

7. PERFORMING ORGANIZATION NAME(S) AND ADDRESS(ES)
Environmental Research Institute of Michigan (ERIM)
P.O. Box 134001
Ann Arbor, MI 48113-4001

8. PERFORMING ORGANIZATION REPORT NUMBER
207500-7-T

9. SPONSORING/MONITORING AGENCY NAME(S) AND ADDRESS(ES)
Office of Naval Research
800 N. Quincy Street
Arlington, VA 22217

10. SPONSORING/MONITORING AGENCY REPORT NUMBER

11. SUPPLEMENTARY NOTES

12a. DISTRIBUTION/AVAILABILITY STATEMENT
Unlimited

12b. DISTRIBUTION CODE

13. ABSTRACT (*Maximum 200 words*)

Synthetic aperture radar (SAR) images collected during the 1989 ONR surface ship wake experiment are analyzed using a linear imaging model which includes contributions due to velocity bunching, tilt modulation and hydrodynamic modulation as well as azimuth falloff and coherent speckle effects. This model adequately predicts the overall shape of the image spectrum for ambient waves as observed from three different look directions, although there are some discrepancies for range-travelling waves which are attributed to uncertainties in the tilt and hydrodynamic modulation. Inversion of the model to yield estimates of the Kelvin wake and ambient wave heights appears to be successful, although the results are sensitive to the value assumed for the surface decorrelation time.

14. SUBJECT TERMS
Synthetic Aperture Radar, Ocean Waves, Ship Signatures

15. NUMBER OF PAGES
99

16. PRICE CODE

17. SECURITY CLASSIFICATION OF REPORT	18. SECURITY CLASSIFICATION OF THIS PAGE	19. SECURITY CLASSIFICATION OF ABSTRACT	20. LIMITATION OF ABSTRACT
Unclassified	Unclassified	Unclassified	Unlimited

CONTENTS

FIGURES

FIGURES (Continued)

FIGURES (Continued)

FIGURES (Continued)

FIGURES (Continued)

TABLES

1.0 INTRODUCTION

The purpose of this project was to determine the extent to which quantitative information on Kelvin wakes can be obtained from synthetic aperture radar (SAR) images. The method used for extracting this information was to model the wave imaging process as a linear system, as described in the following section. The wave spectrum is then estimated by making corrections for the SAR ocean wave modulation transfer function and for coherent speckle effects. The methodology was applied to both the Kelvin wakes and the ambient wind waves observed during the 1989 ONR Surface Ship Wake experiment. This data set is briefly summarized and the subset of images analyzed during this project is described in more detail in section 3. The results are presented in section 4 and our conclusions are discussed in section 5 of this report.

2.0 ANALYSIS METHODOLOGY

The relationship between the SAR image intensity and the conditions at the ocean surface is not necessarily unique, because of the possibility of nonlinearities in the imaging process. However, under a limited range of conditions, the imaging process can be considered as a linear or quasi-linear system and under these conditions the system response can be described by means of a modulation transfer function as discussed in section 2.1 below.

Variations in image intensity are also caused by coherent speckle effects, and corrections for these effects must be made in order to extract quantitative information from the images. These effects are discussed in section 2.2.

The main focus of this investigation was on the extraction of information about the Kelvin wakes produced by surface ships. The general characteristics of these wakes, and the specific methods used to extract information about them, are discussed in section 2.3. The methodology was applied to the data set described in section 3, and the results are presented in section 4.

2.1. LINEARIZED IMAGING MODEL

An analytical expression for the Fourier transform of the SAR image intensity was given by Lyzenga (1988) in terms of the radar cross section $\sigma_o(x,y)$ and the temporal correlation function $\rho(x,y,\tau)$ of the surface reflectivity. Assuming a nominal processor focus setting, this expression reduces to

$$\langle F_f(K_x,K_y)\rangle = \int\int \sigma_o(x,y)\rho(x,y,\tau)e^{-j(K_x x + K_y y)}dxdy \qquad (1)$$

where $\tau = RK_x/2kV$, R is the range distance, k is the radar wavenumber and V is the platform velocity. The radar cross section and the reflectivity correlation function in this case are average values over the SAR integration time. The reflectivity correlation function can be further modeled as

$$\rho(x,y,\tau) = e^{-\tau^2/2\tau_c^2}\, e^{-j2kV_r(x,y)\tau} \qquad (2)$$

where τ_c is the scene coherence time and $V_r(x,y)$ is the mean radial velocity of the surface within the resolution cell located at the along-track coordinate x and the across-track coordinate y. The first term in this equation describes the azimuth falloff effect, which limits the range of along-track wavenumbers which can be imaged due to the resolution degradation caused by random surface motions. The second term leads to the velocity bunching effect, which enables waves to be imaged because of the orbital motions associated with these waves.

When either the R/V ratio, the azimuth wavenumber K_x, or the radial velocity V_r is small enough so that $2kV_r\tau = RK_xV_r/V << 1$, the approximation $\exp(j2kV_r\tau) \approx 1 + j2kV_r\tau$ can be made. If, in addition, the variations in radar cross section are sufficiently small we can write $\sigma_o(x,y) = \sigma_o[1 + f(x,y)]$ where $f(x,y) << 1$ and

$$\sigma_o(x,y)\rho(x,y,\tau) \approx \sigma_o[1+f(x,y)+j2kV_r(x,y)\tau]e^{-\tau^2/\tau_c^2} \quad (3)$$

neglecting the second-order cross-product terms. Substituting this into the first equation we obtain the linearized expression

$$\langle F_I(K_x,K_y)\rangle = \sigma_o\delta(K_x,K_y) + \frac{\sigma_o}{\sqrt{2}}[R(K_x,K_y)\psi(K_x,K_y) + R^*(-K_x,-K_y)\psi^*(-K_x,-K_y)] \quad (4)$$

where $R(K_x,K_y)$ is the SAR modulation transfer function defined below, and

$$\langle\psi(K_x,K_y)\psi^*(K_x',K_y')\rangle = S_w(K_x,K_y)\delta(K_x-K_x')\delta(K_x-K_y') \quad (5)$$

where $S_w(K_x,K_y)$ is the wave height spectrum, normalized so that its integral over all wavenumbers is the height variance, and $\delta(K)$ has the properties

$$\int\delta(K)dK = 1 \quad and \quad \delta(0)=L/2\pi \quad (6)$$

where L is the scene length. The SAR modulation transfer function can be written as

$$R(K_x,K_y) = m_h K \sin^2\phi - \frac{R}{V}\Omega K \cos\phi \cos\theta + i(m_t K \sin\phi + \frac{R}{V}\Omega K \cos\phi \sin\phi \sin\theta) \quad (7)$$

where $m_h \approx 4.5$ is the hydrodynamic modulation transfer function, K is the magnitude of the wavenumber, Ω is the wave frequency, $\phi = \tan^{-1}(K_y/K_x)$ is the wave propagation direction, θ is the incidence angle, and

$$m_t \approx \frac{4 \cot\theta}{1 \pm \sin^2\theta} \quad (8)$$

is the tilt modulation transfer function, where the (+) sign holds for vertical polarization and the (-) sign holds for horizontal polarization (Lyzenga, 1986).

2.2. COHERENT SPECKLE EFFECTS

We define the image spectrum as $S_I(K_x,K_y) = (2\pi/L)^2 |F_I(K_x,K_y)|^2$ where $F_I(K_x,K_y)$ is the Fourier transform of the image intensity, i.e.

$$F_I(K_x,K_y) = \int\int i(x,y) i^*(x,y) e^{-i(K_x x + K_y y)}\, dxdy \quad (9)$$

where i(x,y) is the complex image. Assuming that the real and imaginary parts of the complex image are gaussian-distributed random variables, and applying the gaussian moment theorem (Reed, 1962), the expected value of the image spectrum can be written as

$$\langle S_I(K_x,K_y)\rangle = |\langle F_I(K_x,K_y)\rangle|^2 + \iint |\langle i(x,y)i^*(x+x',y+y')\rangle|^2 e^{-j(K_x x' + K_y y')} dx dy dx' dy' \qquad (10)$$

where the first term represents the contribution of the resolved wave field, as modeled in the previous section, and the second term represents the contribution of coherent speckle effects to the image spectrum.

A necessary preliminary step in attempting to extract wave height information from the image spectrum is to remove the speckle contribution, as represented by the second term in the above equation. The removal of this speckle contribution becomes especially important at the edges of the effective azimuth bandpass region where the SAR modulation transfer function becomes very small due to the azimuth falloff effect.

One method of removing the speckle level from the spectra is by means of an algorithm first described by Cordey and Macklin (1989). This algorithm is discussed in the following section. Another possible approach is to use the tri-spectrum or fourth-order moment sequence of the complex data. This algorithm, which is discussed in section 2.2.2, has not to our knowledge been previously applied to SAR data, but is analogous to the technique used in the NRL three-frequency radar (Schuler et al, 1985) to remove the bias term from the spectrum.

2.2.1. Cordey and Macklin Speckle Removal Method

A method of speckle removal has been described in a recent paper by Cordey and Macklin (1989). In this method, which is based on an image model attributed to Oliver (1986), the speckle contribution is estimated by computing the complex image autocorrelation function $\langle i(x,y)\, i^*(x+x',y+y')\rangle$, squaring this function and Fourier transforming it. The result is basically equivalent to the speckle term obtained in the

analysis presented at the beginning of this section. Thus, subtracting this function effectively removes the additive contribution of speckle from the image spectrum. However, as shown by Oliver and discussed by Cordey and Macklin, this function may also be used to estimate the rolloff of the spectrum due to the stationary-scene impulse response function of the SAR. Thus dividing the image spectrum by this function also corrects for this rolloff effect (although not for the azimuth falloff effect induced by random surface motions).

A flowchart of the speckle filtering process is shown in Figure 2-1 from Cordey and Macklin (1989). The estimate of the power spectrum (the right arm of the flowchart) is formed in the usual manner by forming the intensity image and taking the Fourier transform. The estimate of the speckle filter (the left arm of the flowchart) is formed by computing the normalized autocorrelation function of the complex image. This autocorrelation function is obtained by multiplying the Fourier transform of the complex image by its conjugate, and then taking the inverse transform. The autocorrelation function is then normalized, multiplied by its complex conjugate, and Fourier transformed again to give an estimate of the speckle filter.

The filtered power spectrum is formed by dividing the power spectrum by the speckle filter. The expected value of the speckle component of the power spectrum is now unity. This value can now be subtracted from the filtered power spectrum to yield a remainder which is proportional to the wave height spectrum, assuming the imaging process is within the linear regime, as discussed in section 2.1 above.

This speckle correction algorithm was applied to synthetic data to quantitatively assess whether the algorithm functioned properly. To simulate a speckled image of a known signal, a 256 x 256 complex array of data was formed using the equation

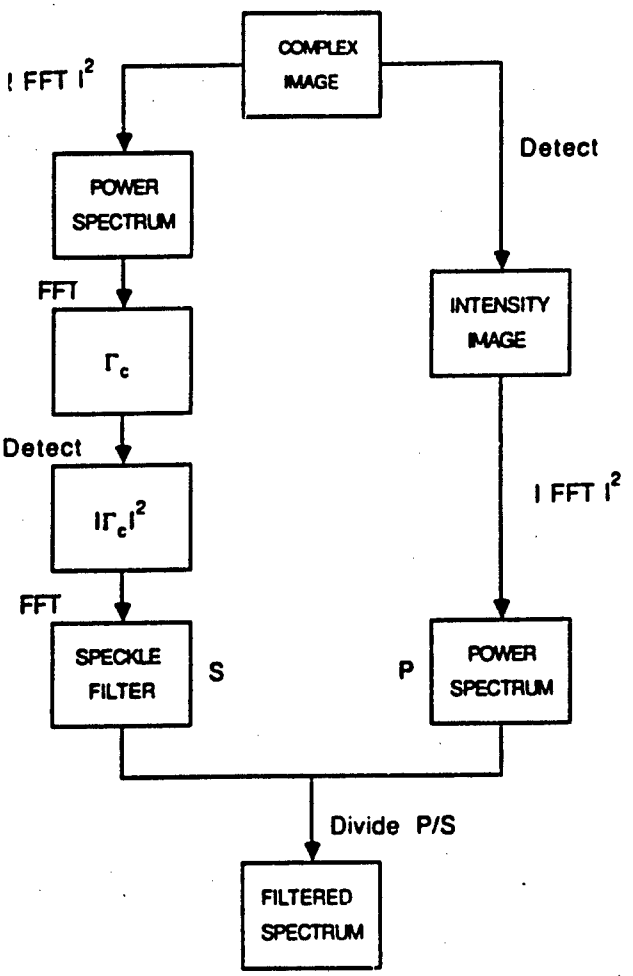

Figure 2-1. Processing Scheme Implemented for Speckle Filtering Using Complex Imagery (Extracted From Cordey and Macklin [1989])

$$i(x,y)=[1+\ a\ \cos(kx)]n(x,y) \qquad (11)$$

where a=0.5, k=π/32, and n(x,y) is a complex random variable whose real and imaginary parts are zero-mean Gaussian random variables with unit variance.

Figure 2-2 shows the magnitude of a cut through the signal with no noise present, i.e. with n=1. Figure 2-3 shows the power spectrum of the signal with no noise. Note that the horizontal axis of the figure is in wavenumber bins, and that the spectrum has been quadrant swapped so that zero wavenumber appears at the center (wavenumber bin 129) of the figure. Figure 2-4 shows the magnitude of a cut through the signal with noise present, and Figure 2-5 shows the corresponding power spectrum. The signal components in Figure 2-5 are obvious, but note that even though the level of the noise in the spectrum is fairly low, the amplitudes of the signal components have been modified.

The speckle filter obtained using the method described above is shown in Figure 2-6. Since the noise is uncorrelated in this example, the filter is constant with frequency except in the locations of the signal components. Figure 2-7 shows the filtered power spectrum. Note that the mean of the noise floor is approximately 0 dB, or unity, as expected. The mean of the noise floor was estimated by finding the mean of the first 100 frequeny bins, and this value was subtracted from the filtered power spectrum. Following the procedure described by Rotheram and Macklin (1985), the filtered power spectrum was then thresholded at a value three times the mean value, i.e. if the value of the power spectrum was less than threshold value, the value was set to zero. Figure 2-8 shows the thresholded power spectrum.

Finally, the thresholded power spectrum was multiplied by the speckle filter to recover the original values of the signal component, which are shown in Figure 2-9. Comparing Figure 2-9 with Figure 2-3, it can be seen that a power spectrum

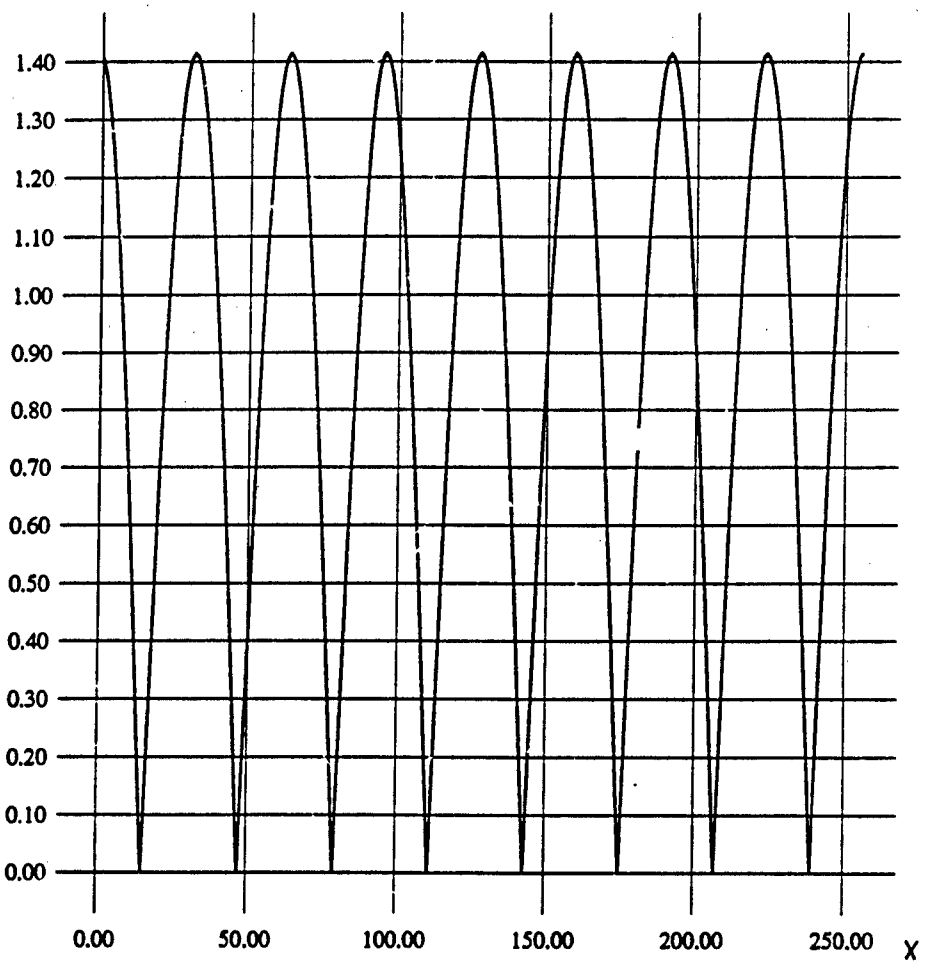

Figure 2-2. Magnitude of a Cut Through the Synthetic Signal With No Noise

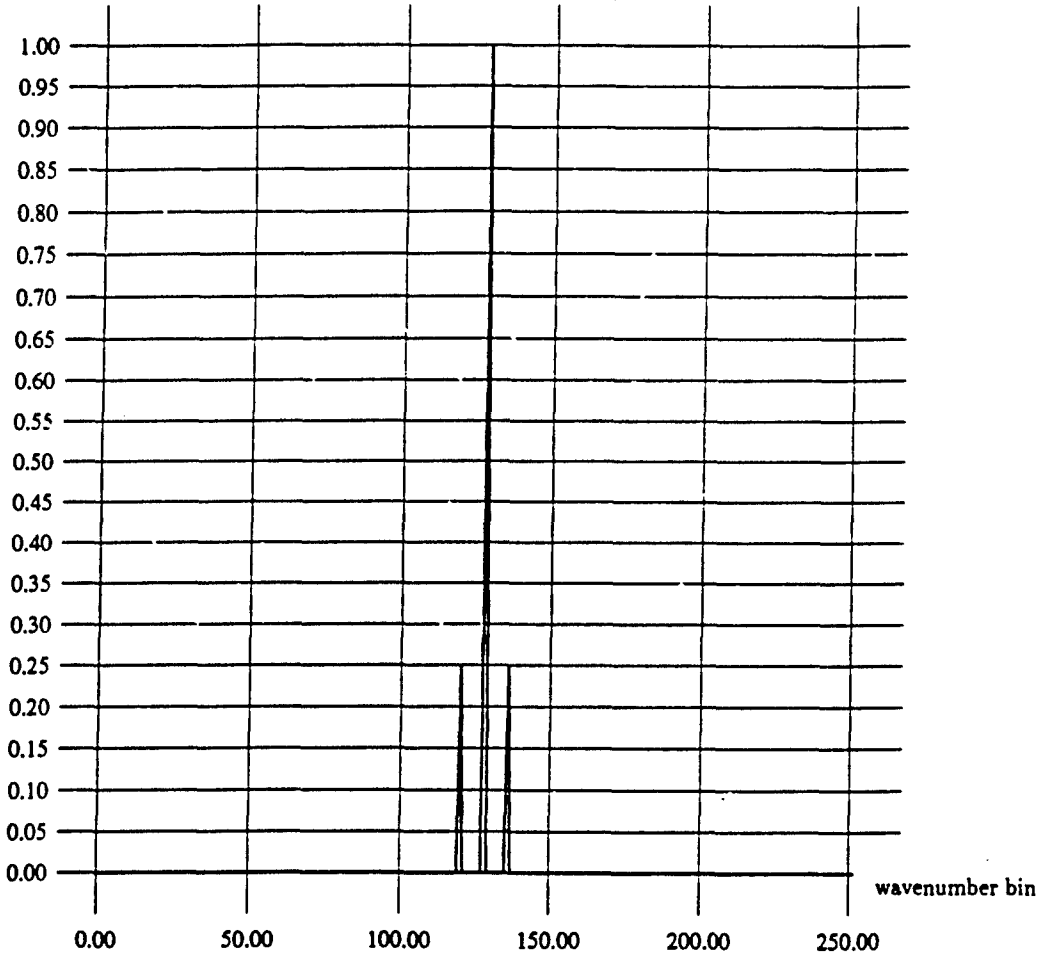

Figure 2-3. A Cut Through the Power Spectrum of the Synthetic Signal With No Noise

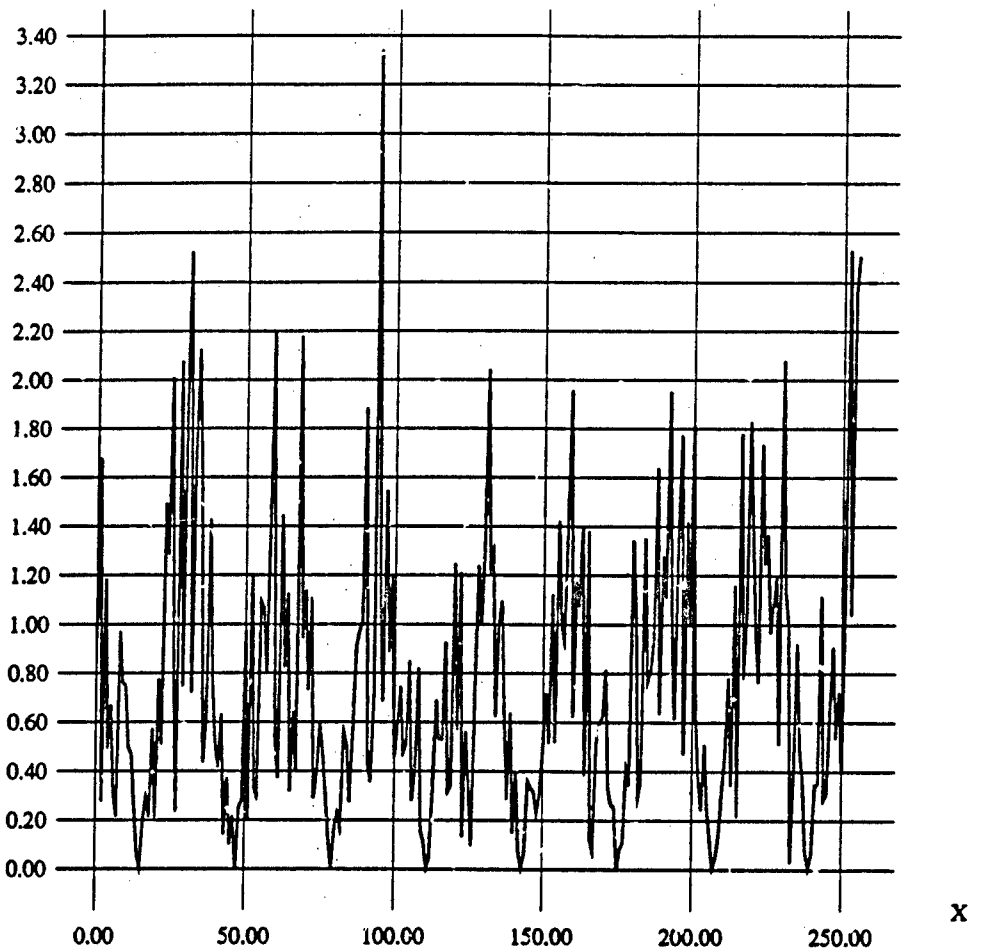

Figure 2-4. Magnitude of a Cut Through the Synthetic Signal With Noise

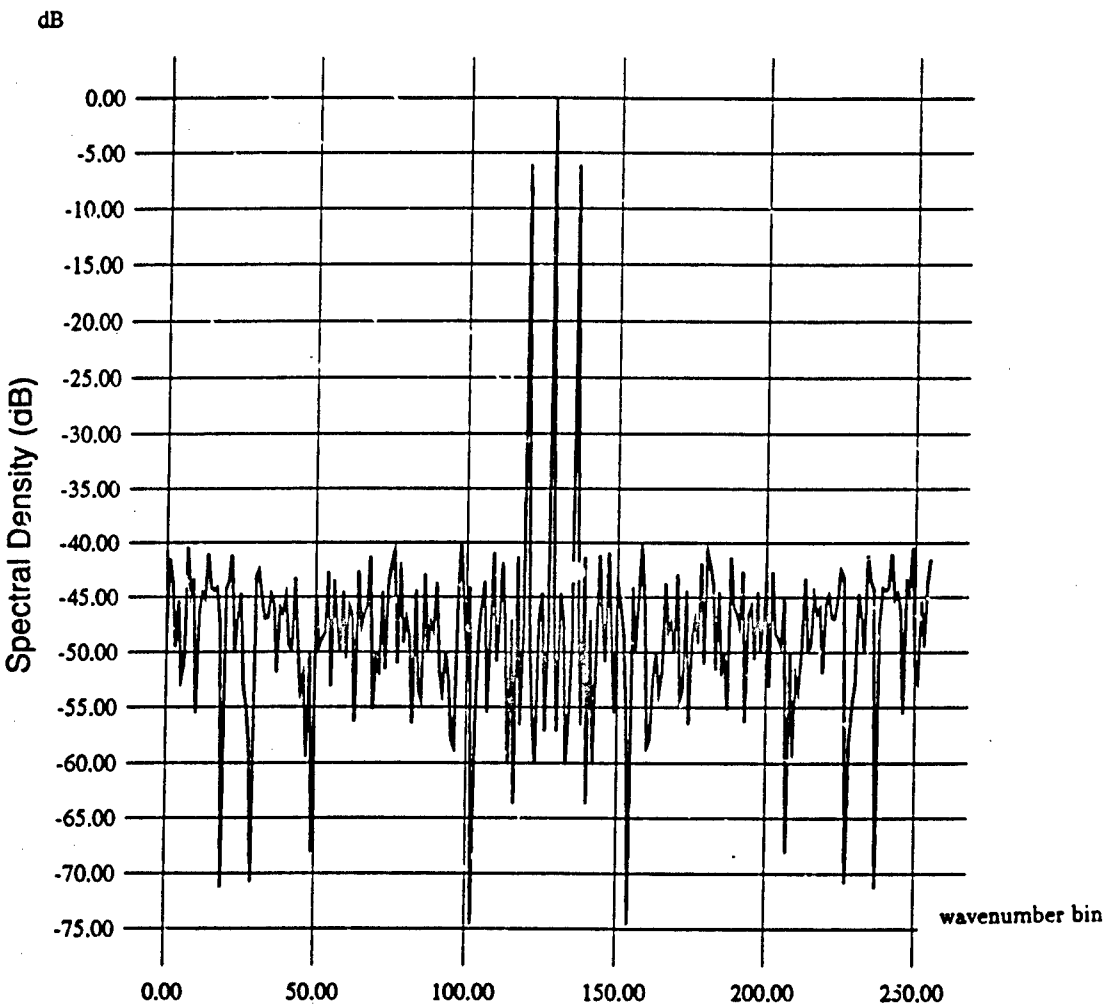

Figure 2-5. A Cut Through the Power Spectrum of the Synthetic Signal With Noise

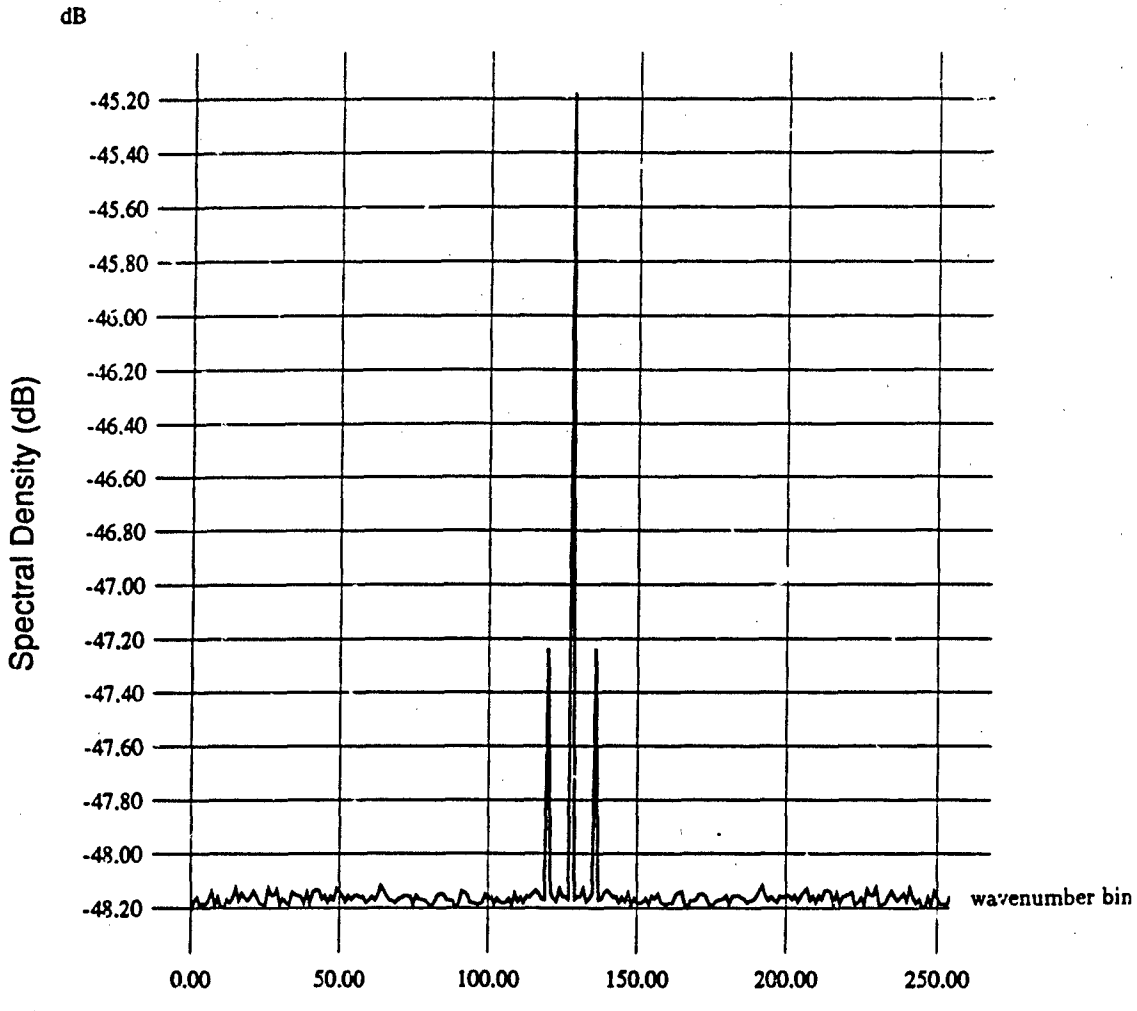

Figure 2-6. A Cut Through the Speckle Filter Formed From the Synthetic Signal With Noise

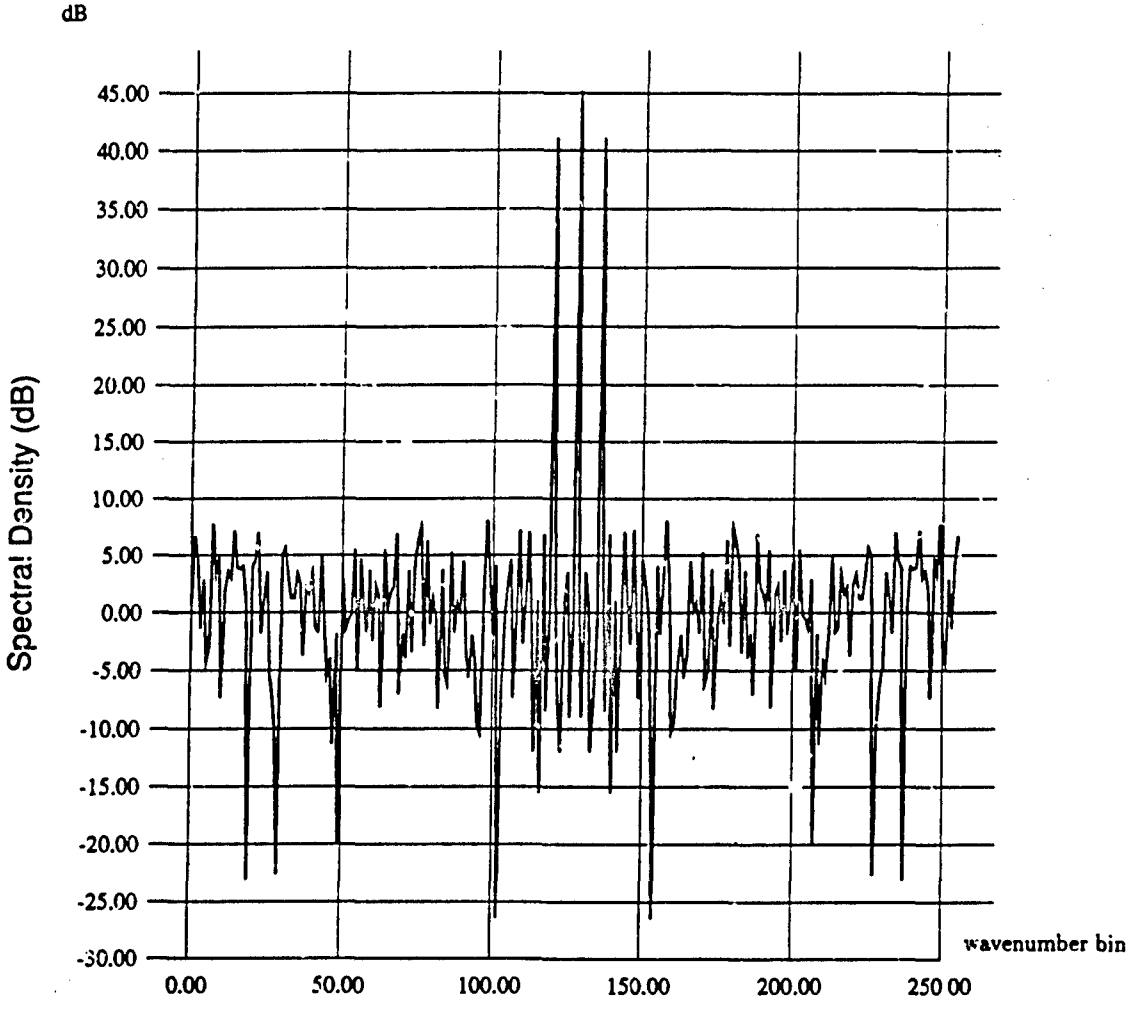

Figure 2-7. A Cut Through the Filtered Power Spectrum of the Synthetic Signal With Noise

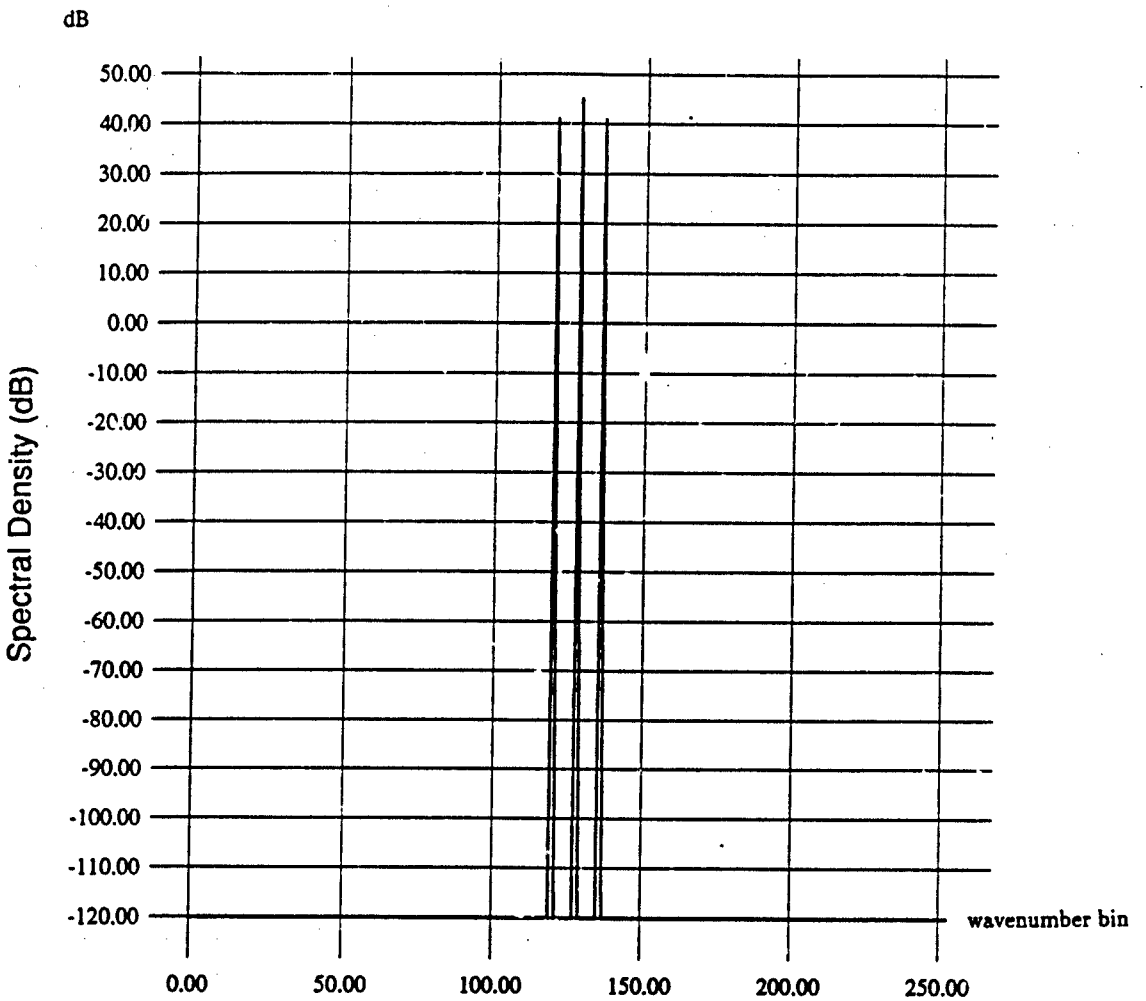

Figure 2-8. A Cut Through the Filtered Power Spectrum of the Synthetic Signal With Noise After Thresholding

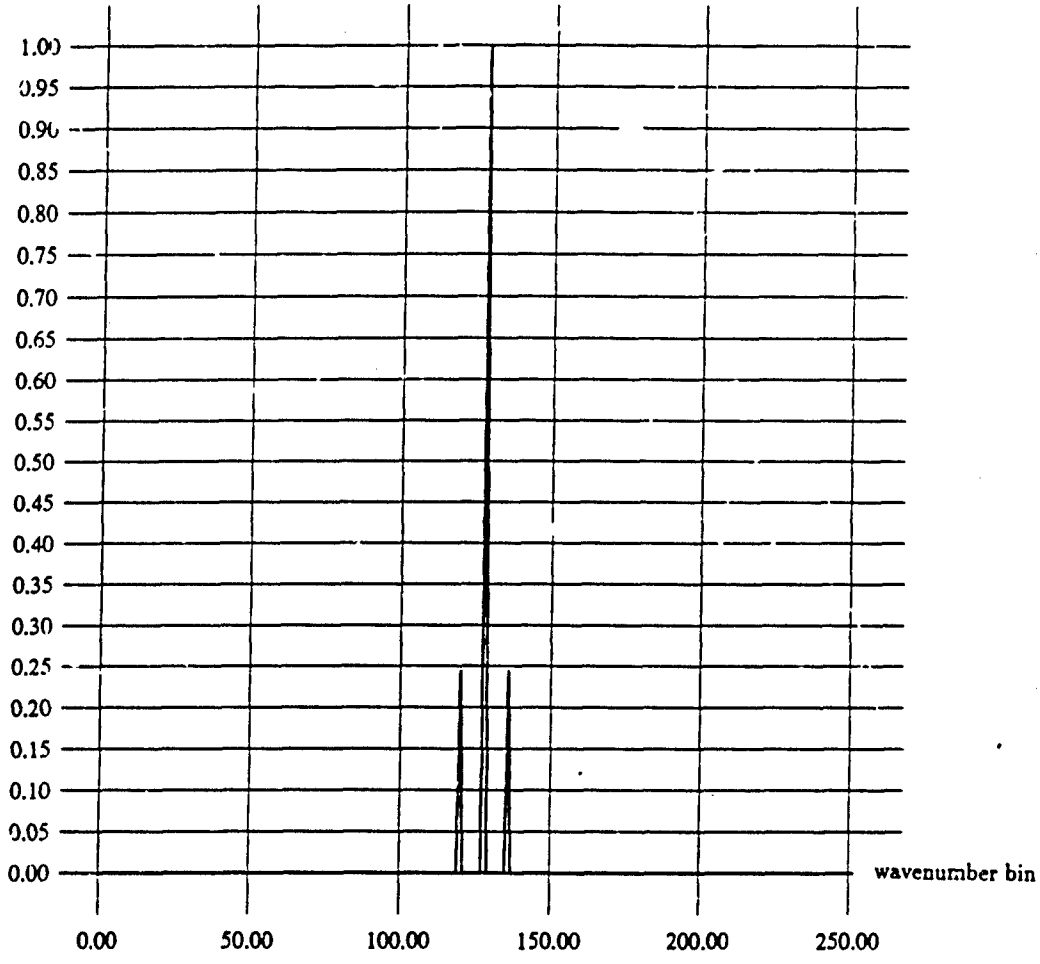

Figure 2-9. A Cut Through the Filtered Power Spectrum of the Synthetic Signal With Noise After Thresholding and Multiplication by the Speckle Filter

essentially equivalent to the power spectrum of the signal without noise is obtained. The results of this example suggest that the speckle correction method can be used to quantitatively estimate the signal component of the image spectrum.

2.2.2. Trispectrum Algorithm

Another approach to the problem of removing speckle effects was investigated during this study, using an alternative algorithm for estimating the image spectrum. The method bears some similarity to the NRL three-frequency technique (Schuler et al, 1985) in that the expected value of the spectral estimate is simply proportional to the wave spectrum, and has no background or speckle contribution. However, the method has some other disadvantages which appear to limit its usefulness, as discussed below.

Using the Fourier transform product or convolution theorem, the Fourier transform of the image intensity can be written as

$$F_I(K_x,K_y)=\int\int f(K_x',K_y')f^*(K_x'-K_x,K_y'-K_y)\ dK_x'dK_y' \qquad (12)$$

where $f(K_x,K_y)$ is the Fourier transform of the complex image $i(x,y)$. Thus, the image spectrum can be written as

$$S(K_x,K_y)=\iiint f(K_x',K_y')f^*(K_x'-K_x,K_y'-K_y)f^*(K_x'',K_y'')f(K_x''-K_x,K_y''-K_y)dK_x'dK_y'dK_x''dK_y'' \quad (13)$$

Applying the gaussian moment theorem to the integrand, the expected value of this spectrum can be seen to consist of a "signal" component and a bias term as discussed at the beginning of section 2.2. However, if we define the quantity

$$S_T(K_x,K_y)=\iint f^*(K_x'-K_x,K_y'-K_y)f^2(K_x',K_y')f^*(K_x'+K_x,K_y'+K_y)\ dK_x'dK_y' \quad (14)$$

and apply a similar analysis, we find that the gaussian moment decomposition results in two identical terms, both of which are proportional to the "signal" spectrum under the assumption that

$$\langle f(K_x',K_y')f^*(K_x'-K_x,K_y'-K_y)\rangle = \langle f(K_x',K_y')f^*(K_x'+K_x,K_y'+K_y)\rangle^* = \langle F_I(K_x,K_y)\rangle \quad (15)$$

which follows from the above definitions. Thus, the quantity $S_T(K_x,K_y)$, which we refer to as the "tri-spectrum" below, can be used as an unbiased estimator of the wave spectrum, i.e. no corrections for speckle effects need to be applied.

This method was tested using one-dimensional simulated data generated using the same model as discussed in section 2.2.1 but with 128 points and values of a=0.2 and 0.5. Figures 2-10 and 2-11 show comparisons between the tri-spectrum and the conventional spectrum for these cases, averaged over 128 realizations. The peak due to the sinusoid appears in the same spectral location for both methods and also has

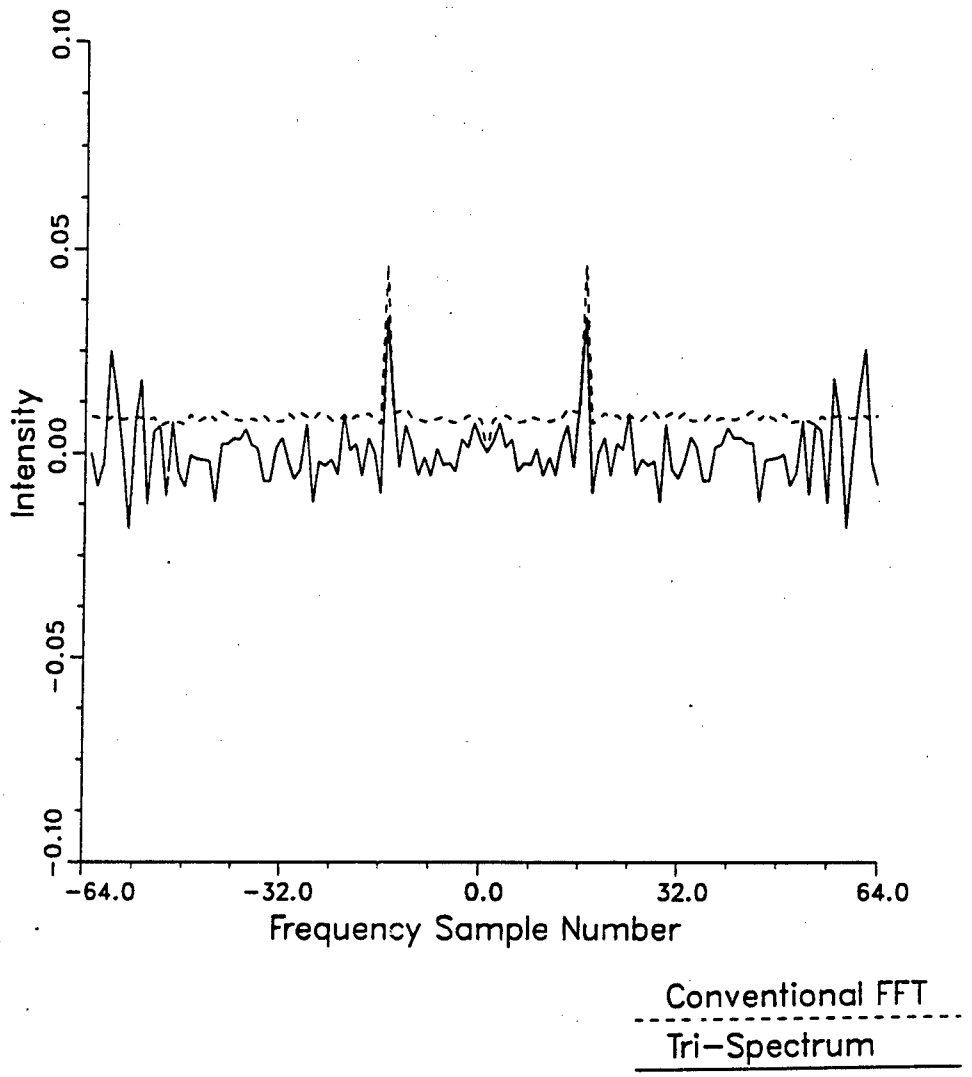

Figure 2-10. Comparison of Conventional Power Spectrum and Tri-Spectrum for Simulated Data With a = 0.2

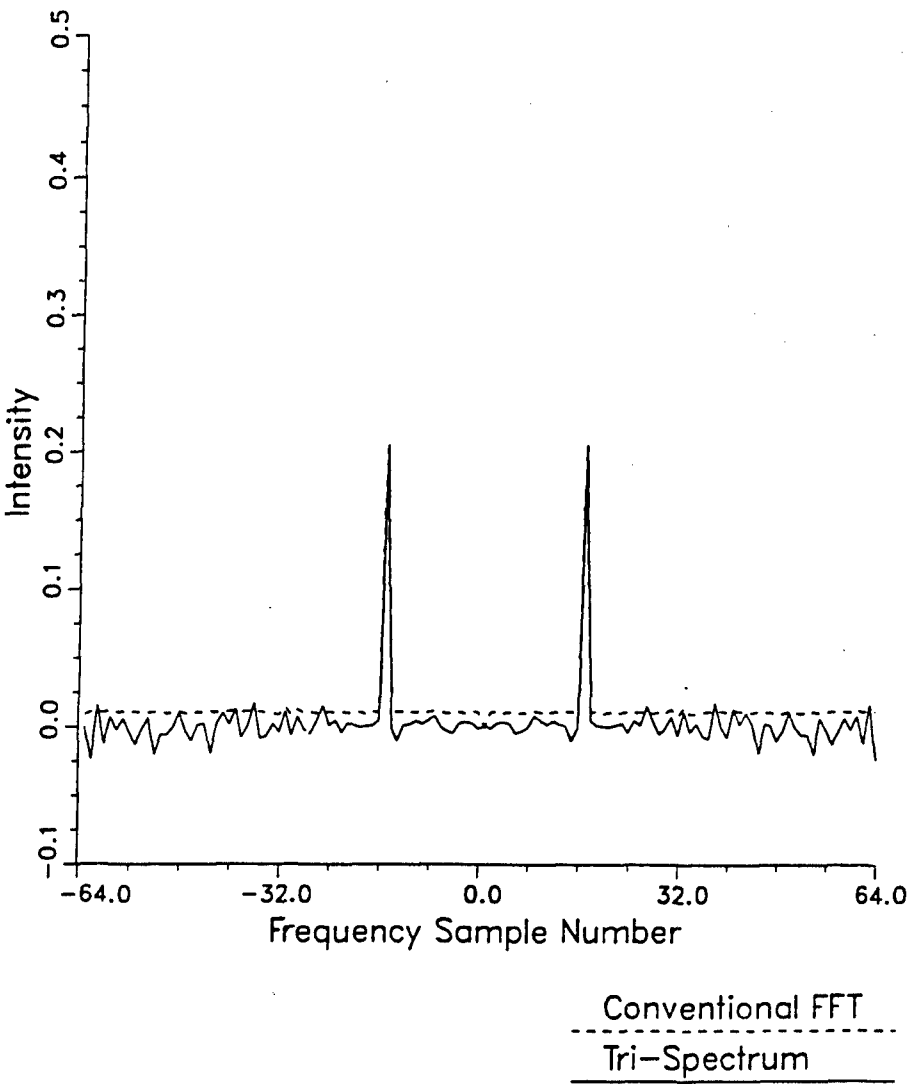

Figure 2-11. Comparison of Conventional Power Spectrum and Tri-Spectrum for Simulated Data With a = 0.5

about the same amplitude. The DC component for both spectral forms has been removed.

As these figures illustrate, the average background level is non-zero for the conventional spectrum and essentially zero for the tri-spectrum. However, it is also clear from these figures that the variance of the background is significantly increased for the tri-spectrum. Therefore, it does not appear that the tri-spectrum method has any practical advantage over the conventional spectrum with an estimate of the bias removed as discussed in section 2.2.1.

2.3. KELVIN WAKE MODEL

The basic condition which defines the stationary pattern of waves generated by a moving ship is that

$$V_p = V_s \cos \phi \tag{16}$$

where V_p is the phase velocity of any given wave component, ϕ is the propagation direction of this wave component relative to the ship track, and V_s is the ship speed. This relationship can also be written in the form

$$\mathbf{V}_s \cdot \mathbf{K} = \Omega = \sqrt{(gK)} \tag{17}$$

where $\mathbf{V}_s$ is the ship velocity vector, $\mathbf{K}$ is the wavenumber vector, $\mathbf{V}_s \cdot \mathbf{K}$ denotes the dot product of these two vectors, and $\Omega = \sqrt{(gK)}$ is the wave frequency. The set of waves making up the Kelvin wake, as defined by either of these equations, is shown graphically in Figure 2-12 for a range of ship speeds.

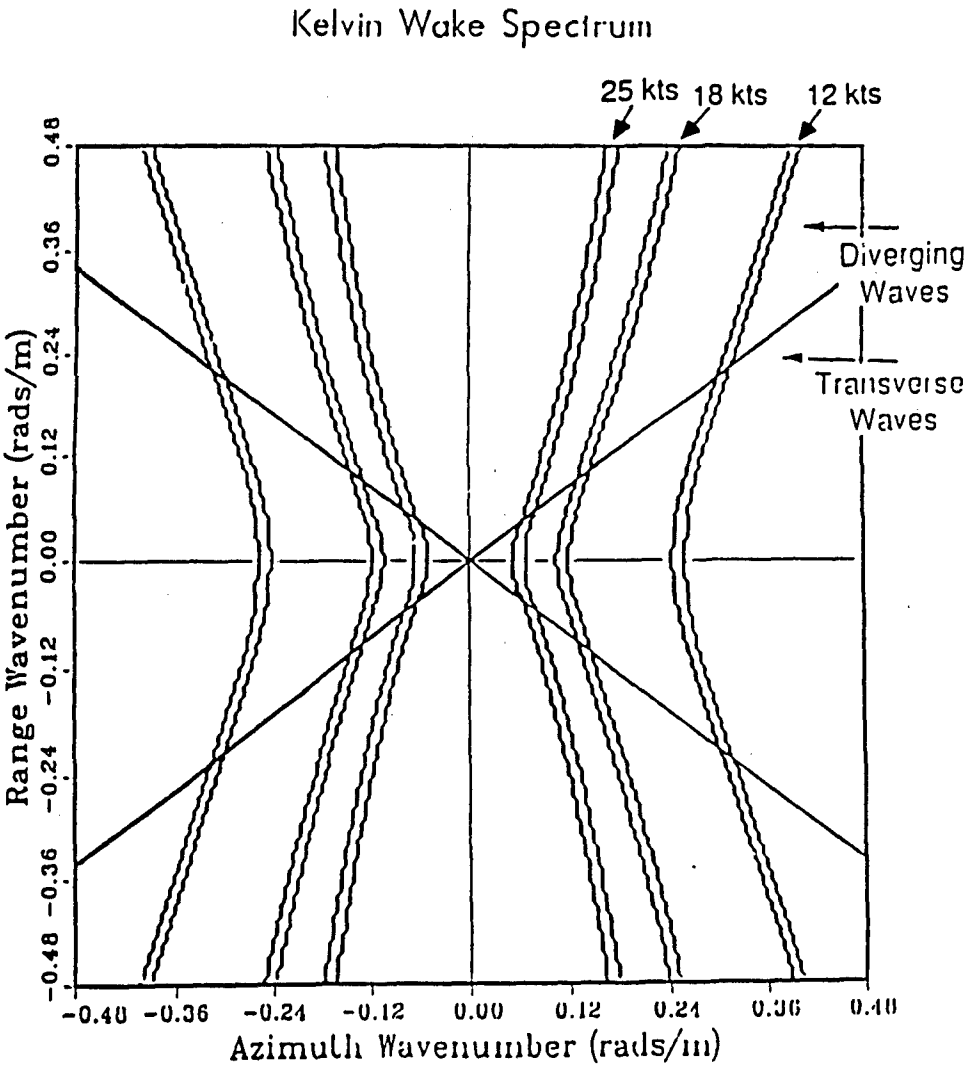

Figure 2-12. Schematic of Kelvin Wake Energy Locations in Spectral Space

A further analysis involving the group velocity of the waves can be carried out (e.g. Tricker, 1964) in order to determine the position of each wave component in the wake pattern. Such an analysis shows that the waves which propagate furthest from the track, in terms of angular position relative to the ship, are those having a propagation direction of $\phi = \pm 35.26°$ relative to the ship's heading. Waves with smaller values of ϕ are referred to as transverse waves, and those with larger values of ϕ are called the diverging components. At any given instant of time, the entire wake pattern is spatially confined to a wedge having a half-angle of 19.47 degrees with its apex at the ship's position.

The kinematic analysis summarized above determines the locus of points in wavenumber space which make up the Kelvin wake for a given ship speed, as shown in Figure 2-12. However, it does not specify the amplitude of these components. In general, the amplitude distribution along the lines shown in Figure 2-12 depends on the ship hull size and shape, as well as the ship speed. Modeling of this amplitude distribution is clearly beyond the scope of this report.

3.0 DATA SET DESCRIPTION

The data analyzed in this report was collected during a two-week ship wake experiment conducted off the California coast in January and February 1989 (see Chapman, 1989) for a description of this experiment). The experiment utilized 6 different ship types and the data was collected over a wide range of environmental conditions. A total of eight data collection flights consisting of 113 passes were conducted with the ERIM/NADC P-3/SAR system. The P-3/SAR system consists of a three frequency polarimetric SAR installed in a Naval Air Development Center (NADC) P-3 aircraft. The system is a fully focused side-looking SAR capable of looking out either side of the aircraft. The system can operate simultaneously at X- ,C-, and L-band (9.4, 5.3, and 1.2 Ghz, respectively). The system transmits either horizontally - (H) or vertically-polarized (V) pulses and can receive either or both polarizations. The P-3 was navigated during SAR data collection by an Inertial Navigation System (INS) updated by a LORAN-C. A more complete description of the P-3/SAR system is given by Sullivan, et. al. (1987).

During the ship wake experiment, the P-3 SAR was operated in the configuration shown in Table 1. Detailed analyses were carried out during the present study using four data sets collected on 28 January 1989, designated as runs 4-1, 6-4, 7-2 and 7-4. The pertinent aircraft and ship operating parameters for these runs are given in Table 2. The ship used during these runs was the USS Chandler (DDG).

During run 4-1, which was collected at approximately 11:11 PST, the winds reported by the Chandler were about 5 knots in the area just south of Santa Cruz Island where the data was collected. The other runs were collected further offshore, as shown in Figure 3-1, at approximately 14:20 PST (run 6-4), 15:27 PST (run 7-2) and 16:02 PST (run 7-4). The winds during this time interval were fairly constant, as measured by the R/V McGaw, at about 10 knots from 300°N (Gasparovic and

TABLE 1

P-3/SAR CONFIGURATION DURING SHIP WAKE FLIGHTS

Mode	X_{VV}, L_{VV}, C_{VV}, L_{HH}
Altitude	10 Kft
Ground Speed	250 Kts (nominal)
Resolution	2.5 m (range) x 2.1 m (azimuth)
Swath Width	9.8 km (slant-range)
Range Samples	4096
Slant-Range Sampling Rate	2.4 m
Along-Track Sampling Rate	0.54 m

TABLE 2

SAR AIRCRAFT AND SHIP PARAMETERS
FOR DATA SETS ANALYZED IN THIS REPORT
(28 JANUARY 1989)

RUN/PASS	A/C HEADING	SHIP HEADING	A/C SPEED	SHIP SPEED
4-1	090	270	146.7 m/s	25 kts
6-4	210	210	143.6 m/s	18 kts
7-2	255	345	155.5 m/s	25 kts
7-4	165	345	123.2 m/s	25 kts

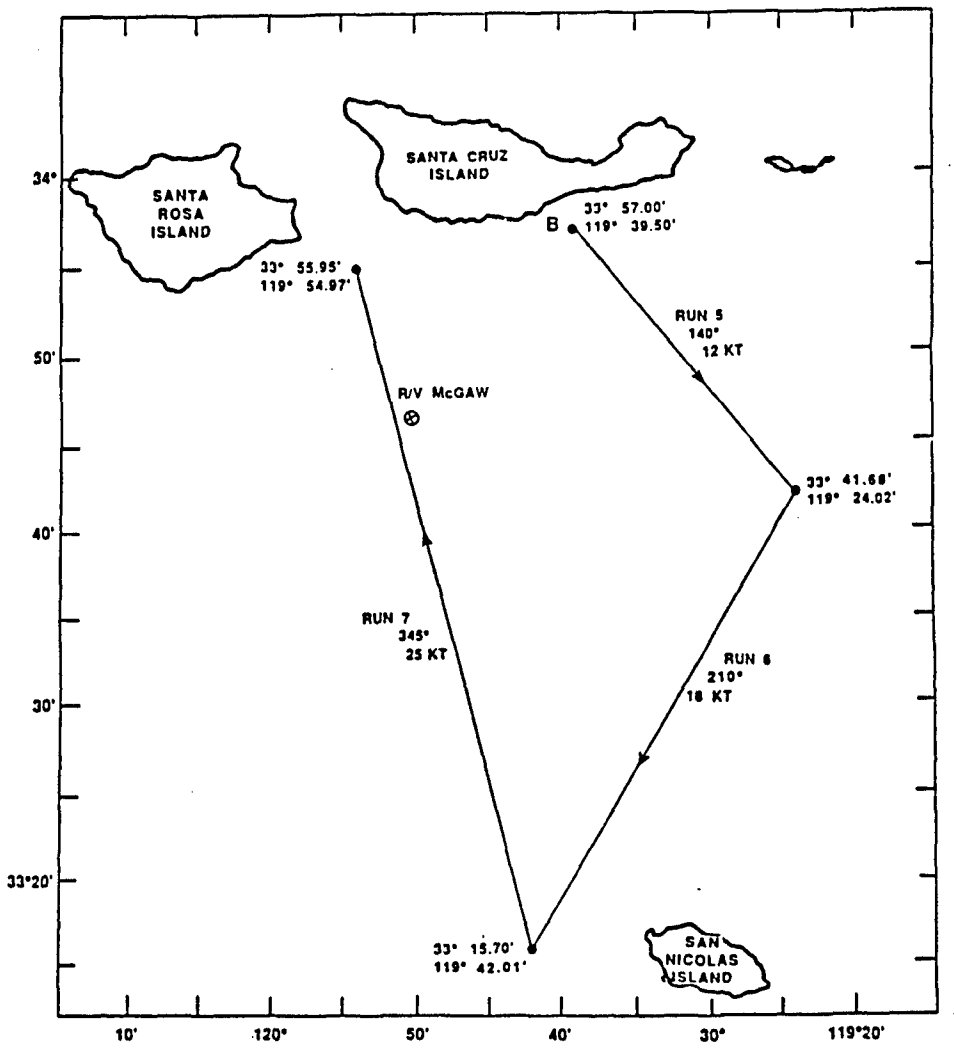

Figure 3-1. Target Ship Track for Ocean Operations

Drummond, 1989). Ambient wave spectra were also measured with a spar buoy launched by the R/V McGaw (Gasparovic, 1989). The spectrum measured during the time interval from 15:05-15:25 is shown in Figure 3-2. This spectrum, which is very similar to the one measured during the previous period from 14:30-14:50, shows two peaks of roughly the same amplitude at frequencies of 0.06 Hz and 0.125 Hz, corresponding to wavelengths of 430 meters and 100 meters, respectively. The significant wave height was approximately 1 meter.

The X-band (VV) and L-band (VV) images for these three passes are shown in Figures 3-3 through 3-6. These images have been artificially flattened to enhance feature visibility. The spaital coverage of these images is 6 km in azimuth (left to right) and 10 km in slant range. Further processing and analysis of these images is discussed in the following section.

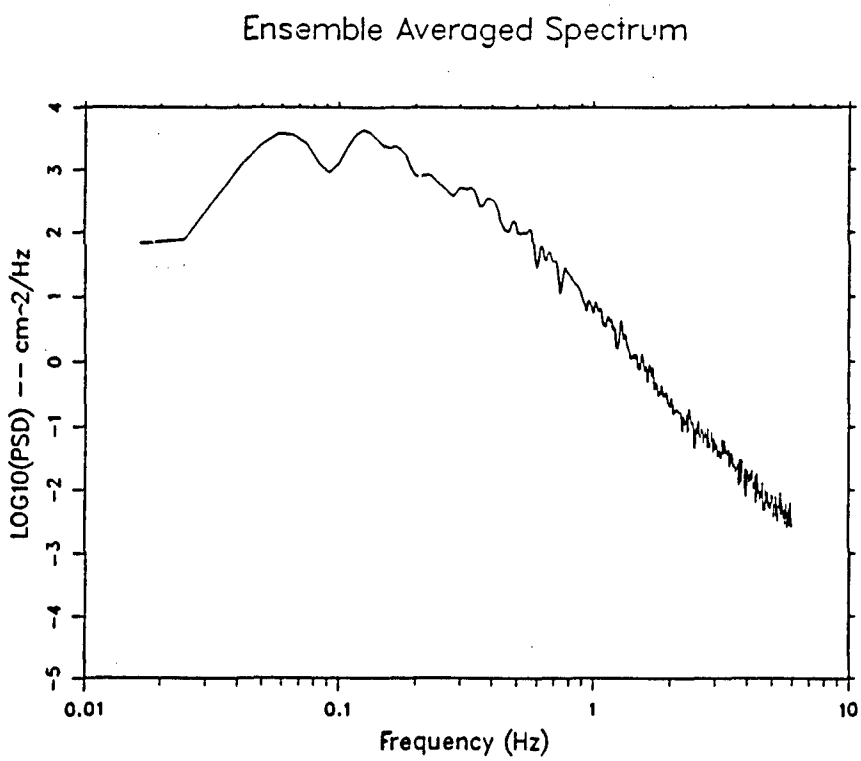

Selmac Wave Buoy Data

Sample length -- 0:02:00	Ensembles -- 10 spectra
28 JAN 1989	Frequency smoothing -- 2.50000E-02 Hz
15:05:00 - 15:25:00	3 bins
Sample rate -- 20.000 Hz	Degrees of freedom -- 60
No. data flags -- 0	Standard deviation -- 22.893 cm

Figure 3-2. Ambient Wave Height Spectrum Measured by APL Near the R/V Mc Gaw (From Gasparovic, 1989)

Pt. Mugu January 28,1989
DDG Run 4-1 X-VV

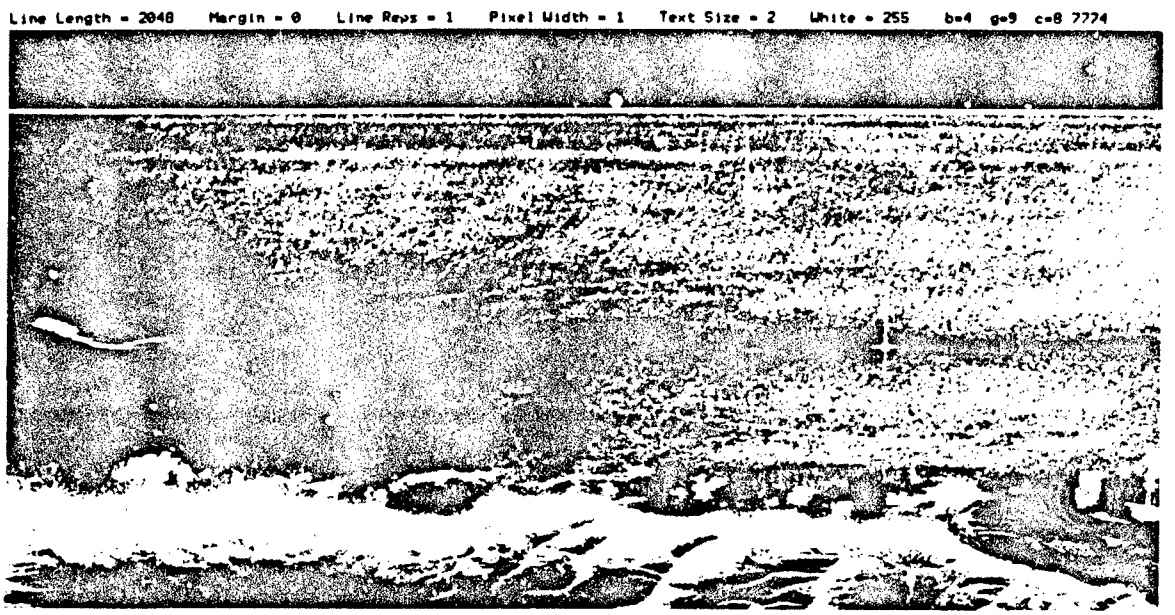

Pt. Mugu January 28,1989
DDG Run 4-1 L-VV

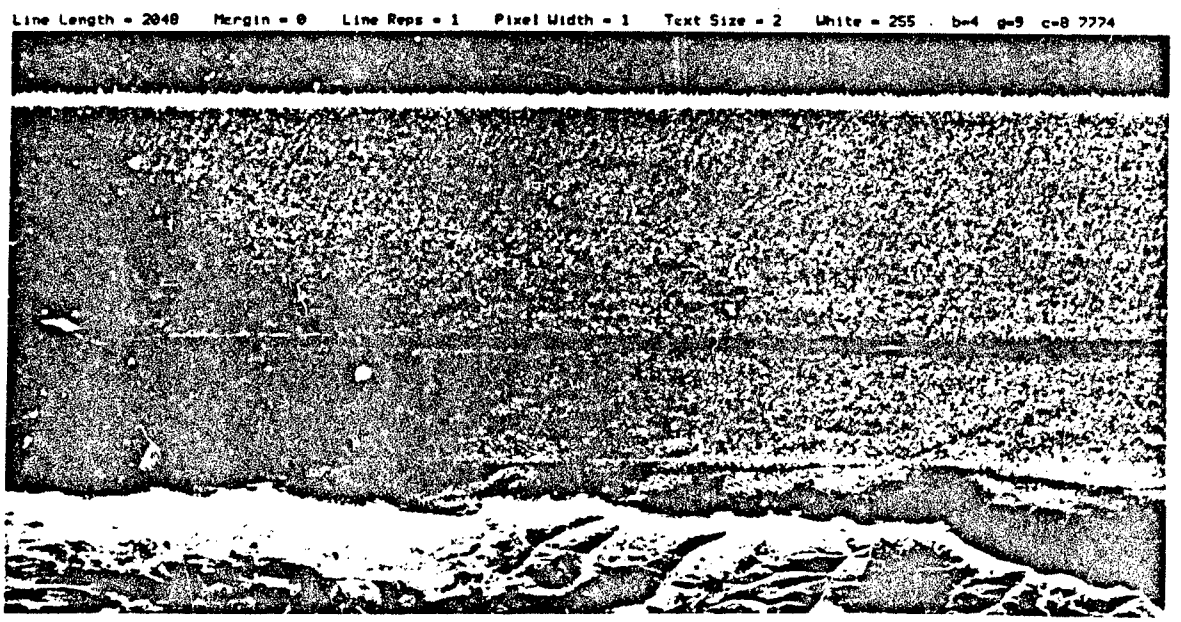

Figure 3-3. X-VV and L-VV Images for Pass 4-1

Pt. Mugu January 28,1989
DDG Run 6-4 X-VV

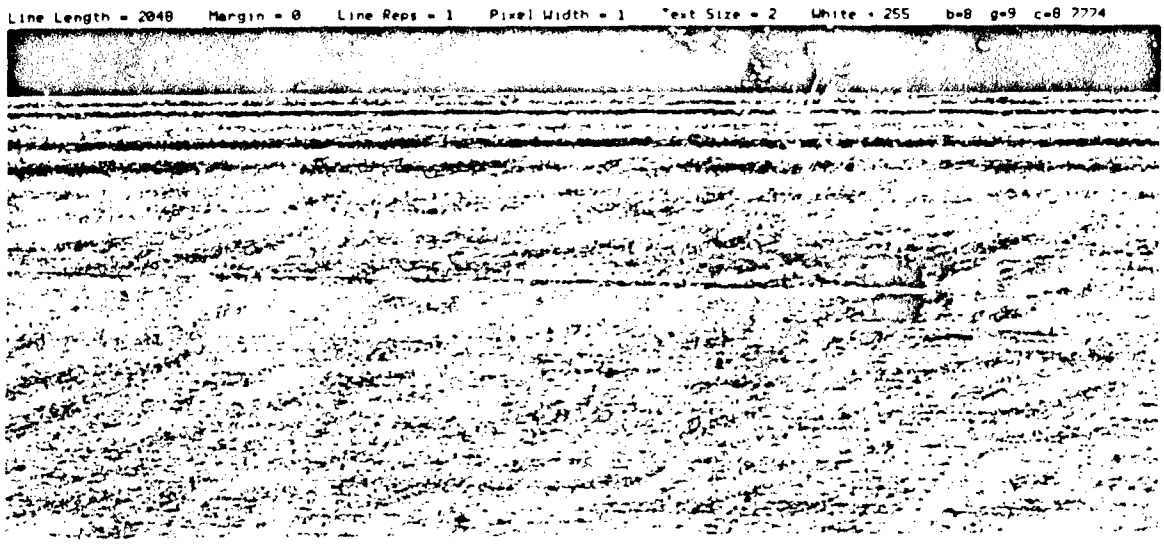

Pt. Mugu January 28,1989
DDG Run 6-4 L-VV

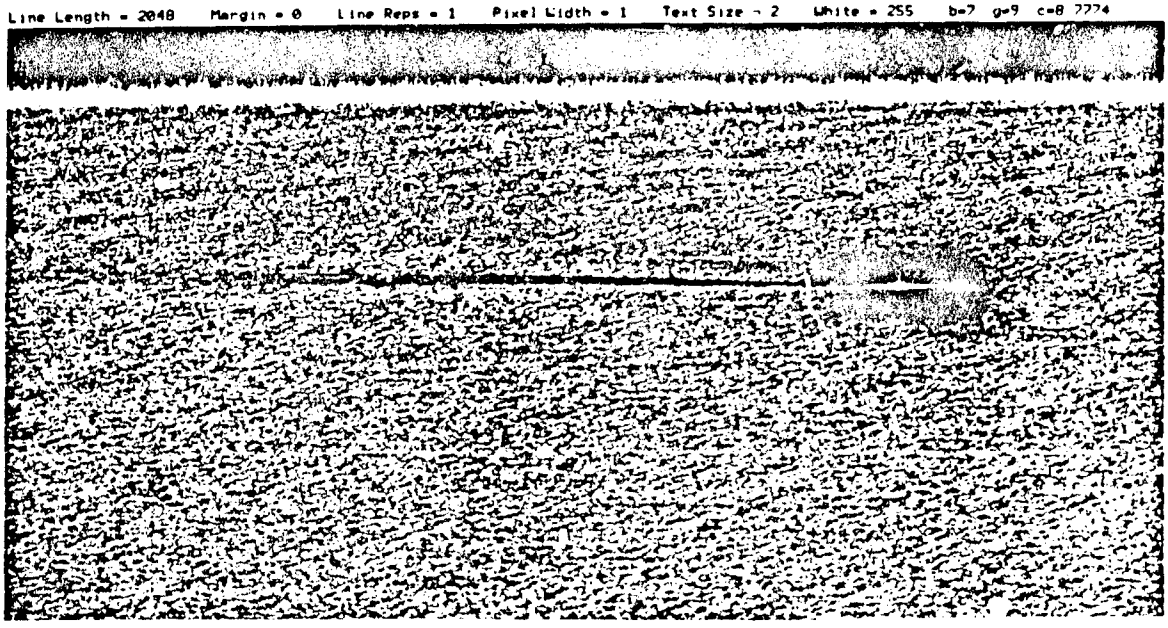

Figure 3-4. X-VV and L-VV Images for Pass 6-4

Pt. Mugu January 28,1989
DDG Run 7-2 X-VV

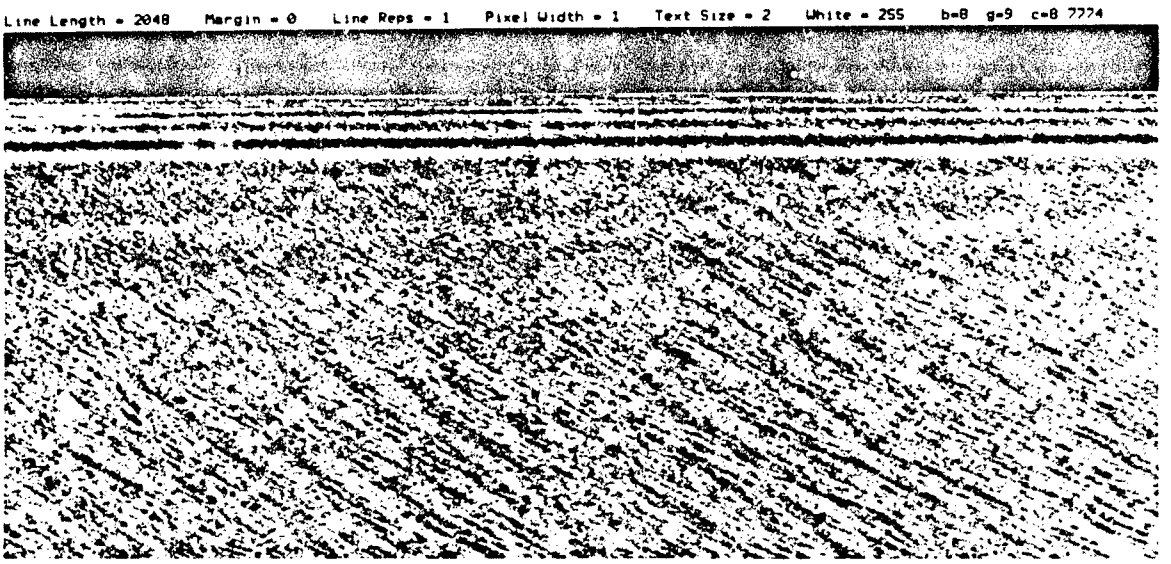

Pt. Mugu January 28,1989
DDG Run 7-2 L-VV

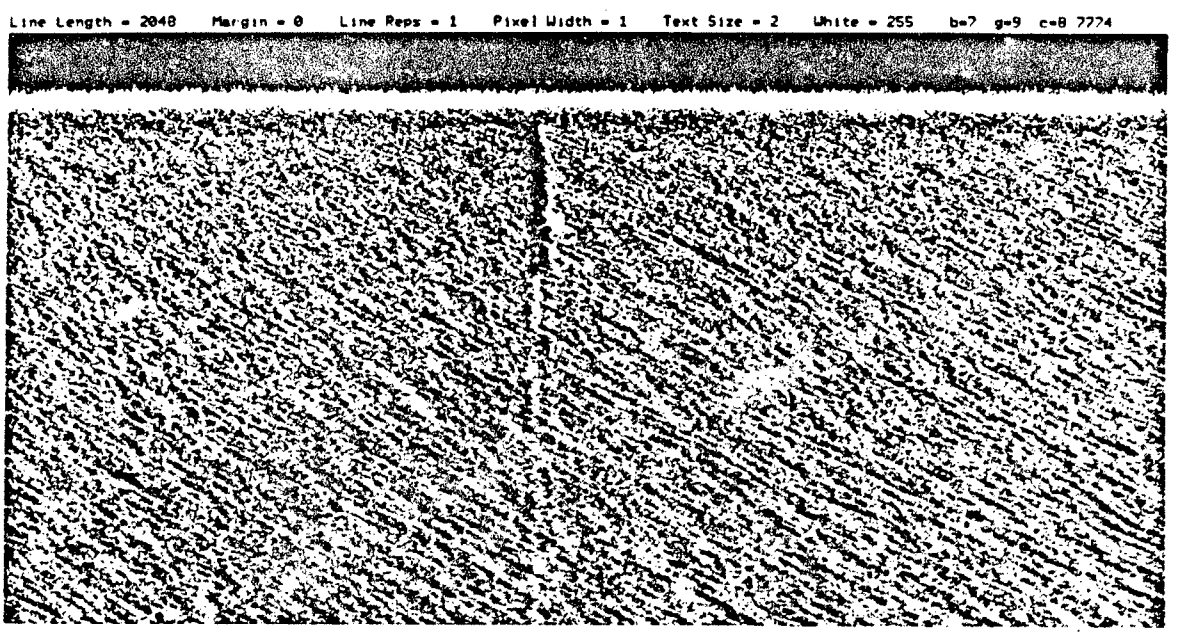

Figure 3-5. X-VV and L-VV Images for Pass 7-2

Pt. Mugu January 28,1989
DDG Run 7-4 X-VV

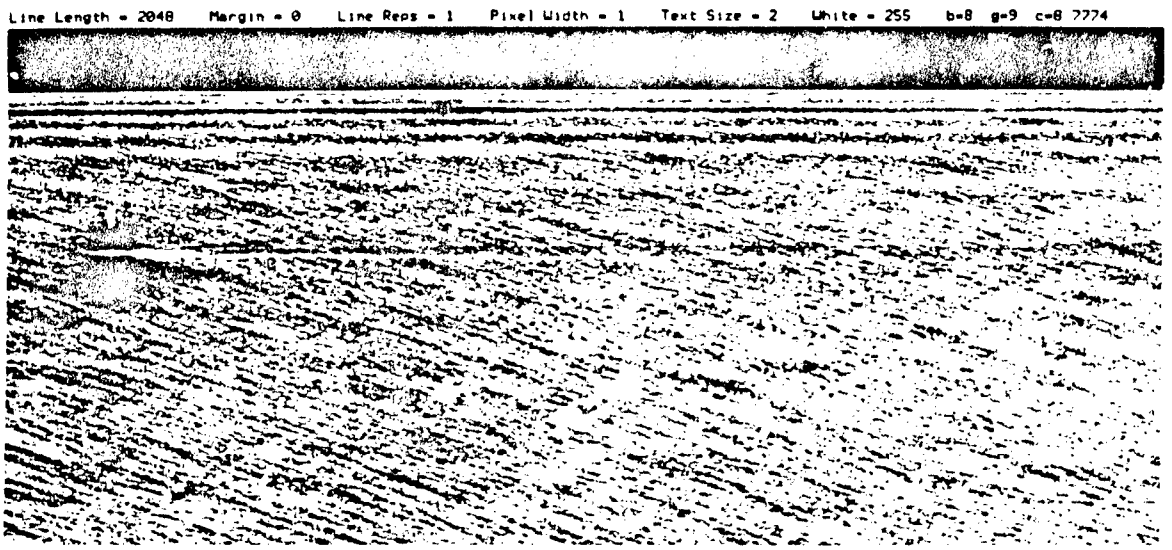

Pt. Mugu January 28,1989
DDG Run 7-4 L-VV

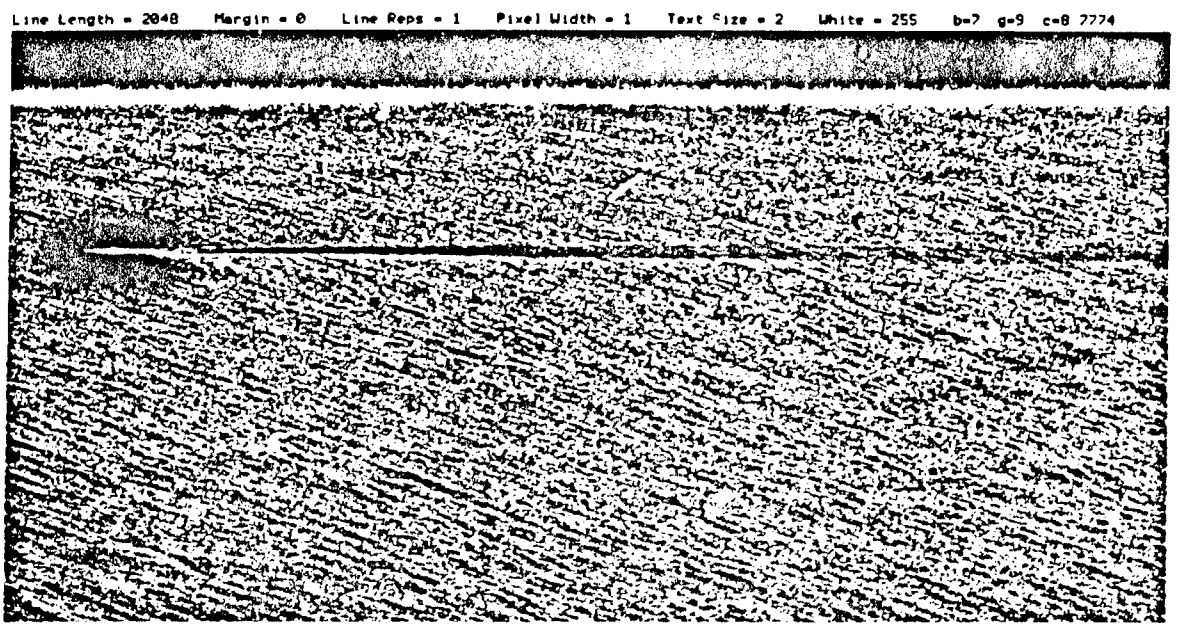

Figure 3-6. X-VV and L-VV Images for Pass 7-4

4.0 DATA ANALYSIS AND RESULTS

Image intensity spectra were generated from the SAR data sets described in the previous section, over areas containing the Kelvin wake from the USS Chandler and in background areas containing only the ambient waves. Several types of analysis were then carried out to extract wave height information from both the wake and the ambient waves. Section 4.1 describes an analysis performed on the ambient wave spectra in order to determine the adequacy of the linear imaging model discussed in section 2. This section also describes the application of the Cordey-Macklin speckle correction algorithm to this data set. Section 4.2 then addresses the inverse problem of estimating wave amplitudes from SAR imagery by correcting for the modulation transfer function.

4.1. MODEL VALIDATION

The ambient wave data set was used to test the Cordey-Macklin speckle correction algorithm, as discussed in the following section. The image spectra for passes 6-4, 7-2 and 7-4 were then compared with predictions from the linear imaging model discussed in section 2 in order to test this model. This comparison is presented in section 4.1.2 below.

4.1.1. Speckle Correction

The speckle reduction algorithm described in section 2.2.1. was applied to a 512 x 512 pixel subset of the L-band VV polarization SAR image for pass 6-4 in order to test the algorithm. The pixel spacings in the image were 2.4 m in range and 1.62 m in azimuth. The complex image was first normalized such that the mean of the

intensity image was unity. The power spectrum of the image was then formed by taking the squared magnitude of the complex image, Fourier transforming this image intensity, and taking the squared magnitude of the Fourier transform. Figure 4-1 shows a cut through the power spectrum along the azimuth wavenumber axis, and Figure 4-2 shows a cut along the range wavenumber axis. The horizontal axis in the figures is in wavenumber bins, and the spectral quantities have been quadrant swapped such that zero wavenumber is in the center of the range (wavenumber bin 257). Note that in both figures the noise floor falls off with increasing wavenumber due to the correlation between pixels in the image.

A two-dimensional color representation of the power spectrum is shown in the upper left hand corner of Figure 4-3. The range direction is vertical, and the azimuth direction is horizontal. The color scale used in the image (and in all images that will be presented in this section) is a 60 dB scale fixed at the maximum value in the image. The color scale runs from black and purple at the low end of the scale to red at the high end. Green represents the midpoint of the scale. The power spectrum in Figure 4-3 shows strong signal returns aligned in the range direction. The surrounding noise-dominanted part of the spectrum falls off radially with frequency. The variation of the noise component of the spectrum with frequency makes it hard to estimate and remove, which is the motivation for the algorithm discussed here.

A speckle filter for the image was formed in the manner described in section 2.2.1. Figure 4-4 shows a cut through the speckle filter along the azimuth wavenumber axis, and Figure 4-5 shows a cut along the range wavenumber axis. A two-dimensional color representation of the speckle filter is shown in the upper right hand corner of Figure 4-3. Note that the slow variation of the speckle filter with frequency has roughly the same shape as the variation of the noise floor in the power spectrum.

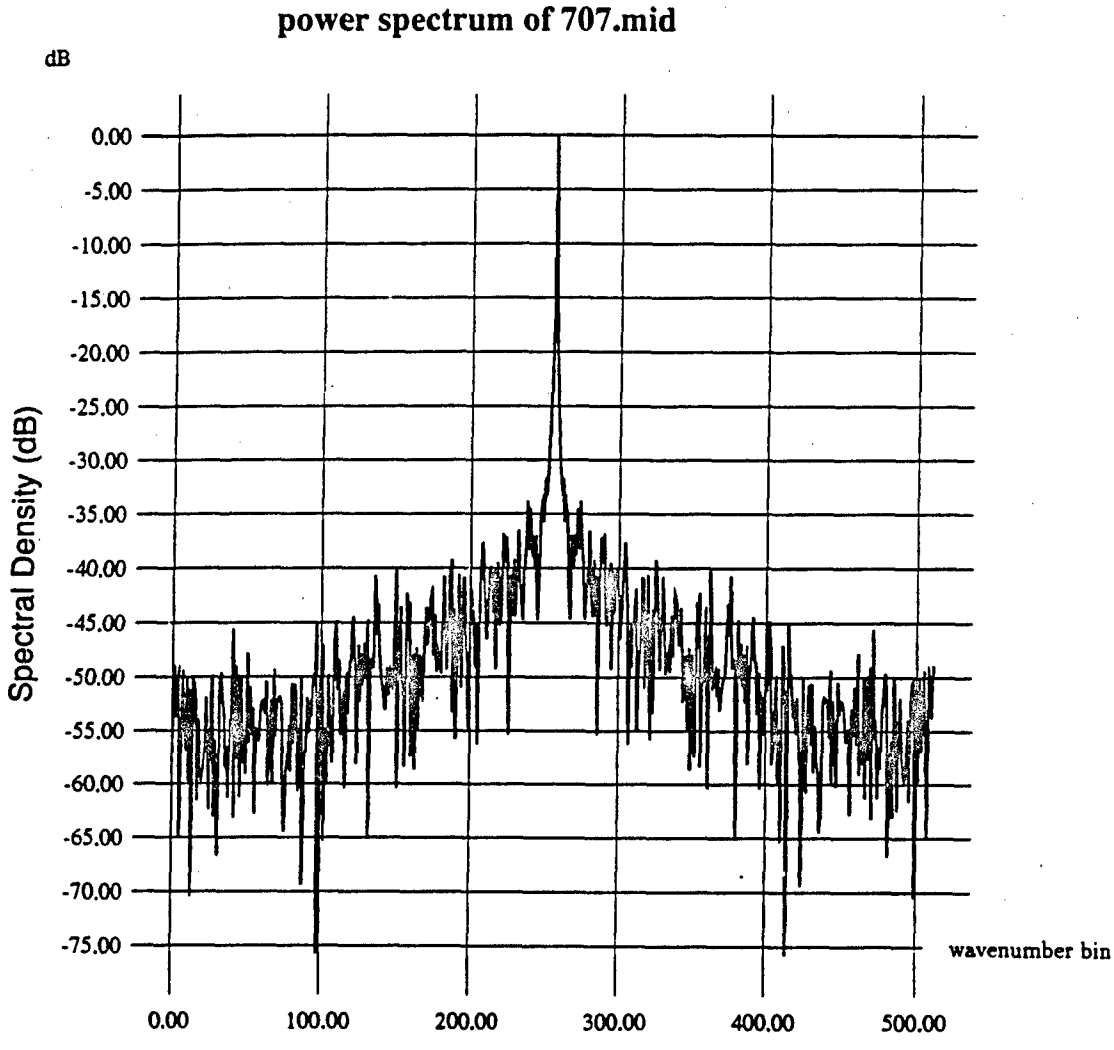

Figure 4-1. A Cut Through the Collected SAR Image Power Spectrum Along the Azimuth Wavenumber dc

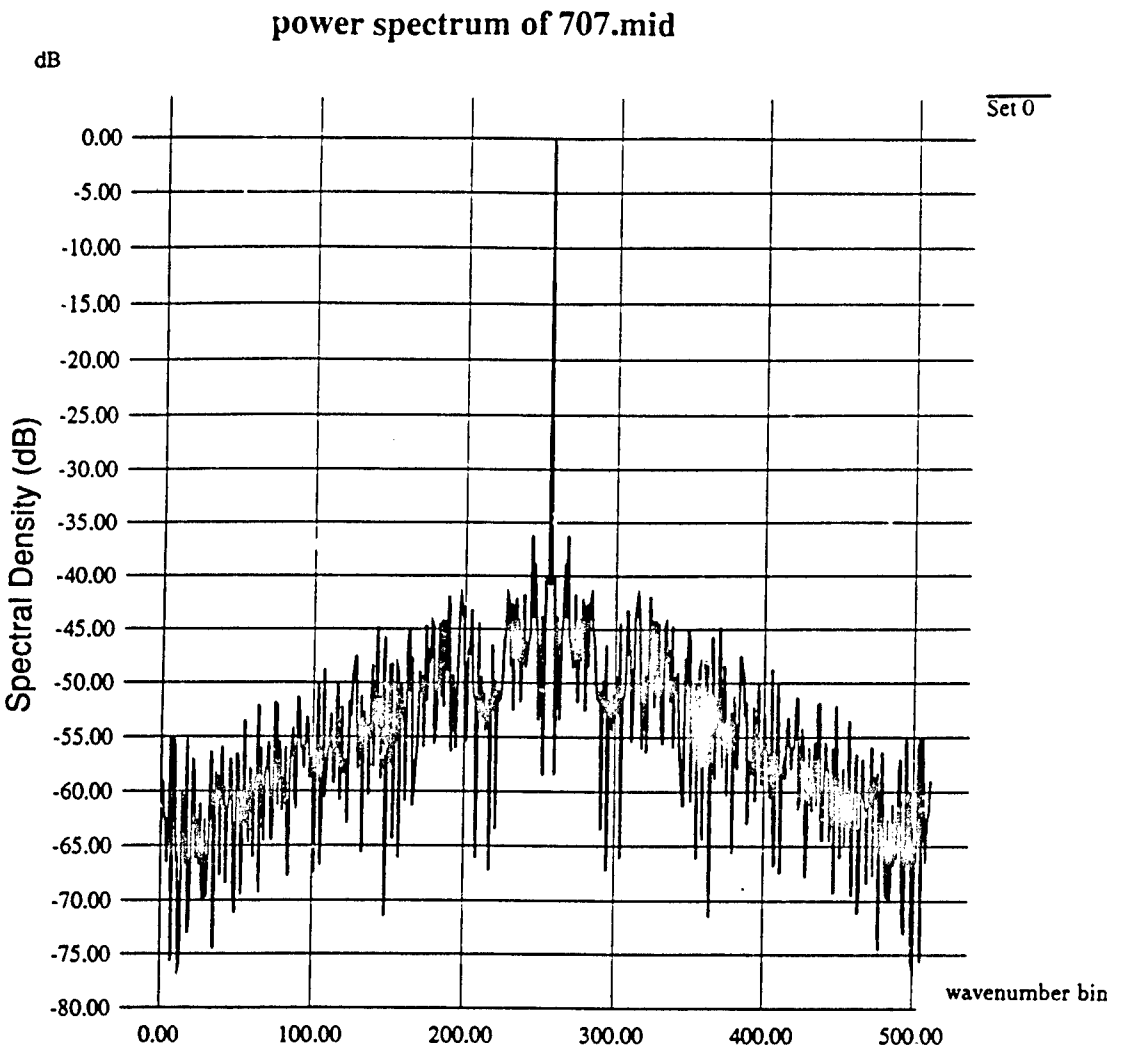

Figure 4-2. A Cut Through the Collected SAR Image Power Spectrum Along the Range Wavenumber dc

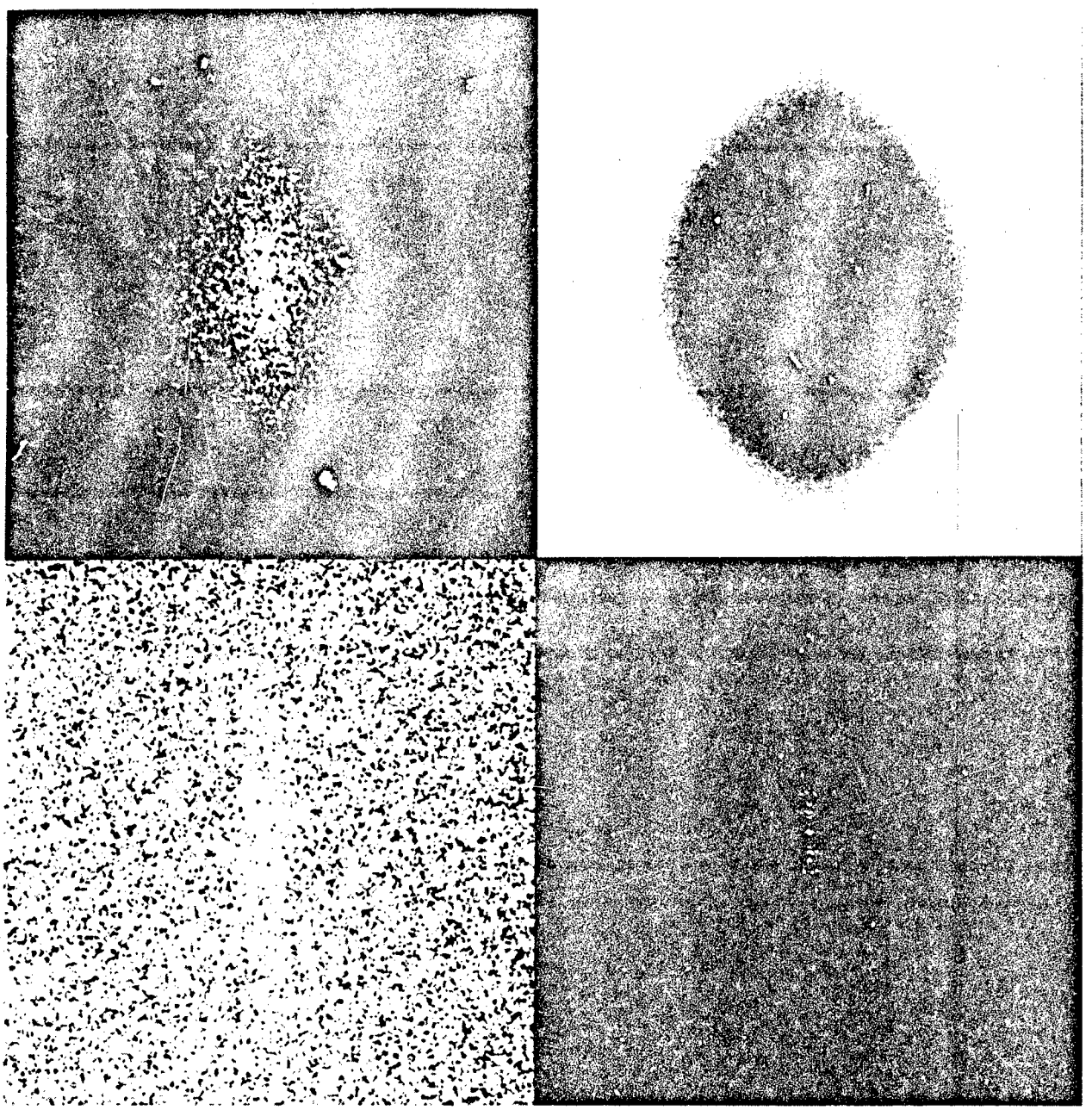

Figure 4-3. Collected SAR Image (Upper Left) Power Spectrum, (Upper Right) Speckle Filter, (Lower Left) Filtered Power Spectrum, and (Lower Right) Filtered Power Spectrum After Thresholding. All Data are Displayed on a 60 dB Scale Fixed at the Maximum in the Individual Data Set. The Color Scale Runs From Black and Purple at the Low End to Red at the High End. Green is in the Middle of the Scale.

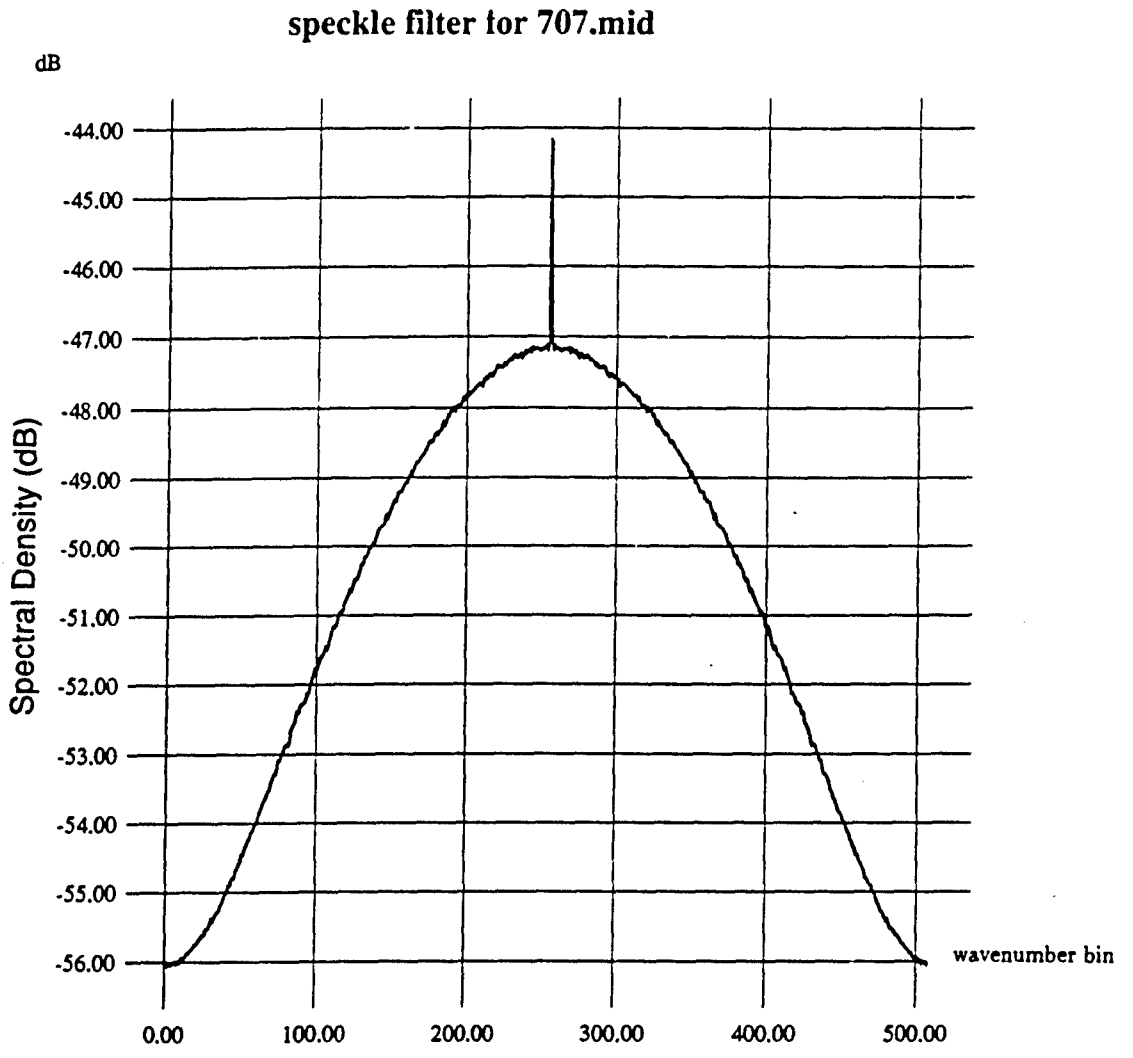

Figure 4-4. A Cut Through the Collected SAR Image Speckle Filter Along the Azimuth Wavenumber

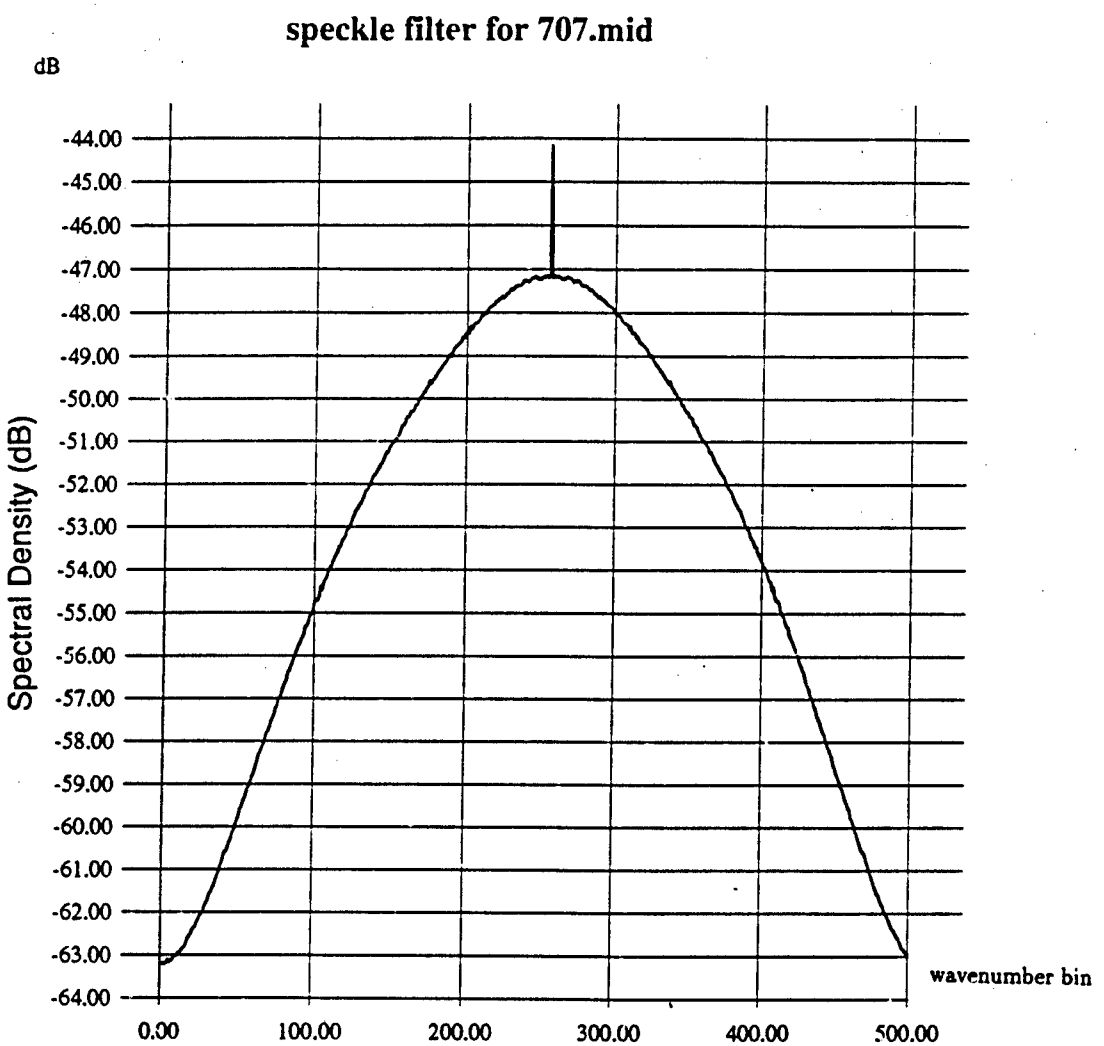

Figure 4-5. A Cut Through the Collected SAR Image Speckle Filter Along the Range Wavenumber

A filtered power spectrum was formed by dividing the power spectrum by the speckle filter. Figure 4-6 shows a cut through the filtered power spectrum along the azimuth wavenumber axis, and Figure 4-7 shows a cut along the range wavenumber axis. A two-dimensional color representation of the filtered spectrum is shown in the lower left hand corner of Figure 4-3. Note in these figures that the noise floor is now relatively constant with frequency, with the mean of the noise floor approximately 0 db (unity). The cut along the azimuth wavenumber axis (Figure 4-6) does show more variation with frequency than the cut along the range wavenumber axis (Figure 4-7), suggesting that the filter works better in range than in azimuth.

Now that the variation of the noise floor with frequency is relatively constant, it can be more reliably estimated. Two estimates of the noise floor were obtained by finding the mean of power spectrum values for azimuth frequency bins less than 50 and less than 100. As discussed above, the expected value should theoretically be unity. The average of bins less than 50 yielded 1.05, and the average of bins less than 100 yielded 1.08. 1.08 was chosen as the mean and was subtracted from the filtered power spectrum.

The next step in the process is to threshold the resulting filter power spectrum. The correct threshold value is a subject of research. To investigate the effects of changing the threshold, the filter power spectrum data were thresholded at values one, three, five and seven times the estimated mean value of the noise floor. Figure 4-8 shows the resulting spectra. The upper left spectrum was thresholded at the estimated mean value of the noise floor, the upper right spectrum was thresholded at three times the estimated mean value of the noise floor, the lower left spectrum was thresholded at five times the estimated mean value of the noise floor, and the lower right spectrum was thresholded at seven times the estimated mean value of the noise floor. Qualitatively, it appears that thresholding the filter power spectrum at one times the mean is too low since much of the noise remains. On the other hand, thresholding the

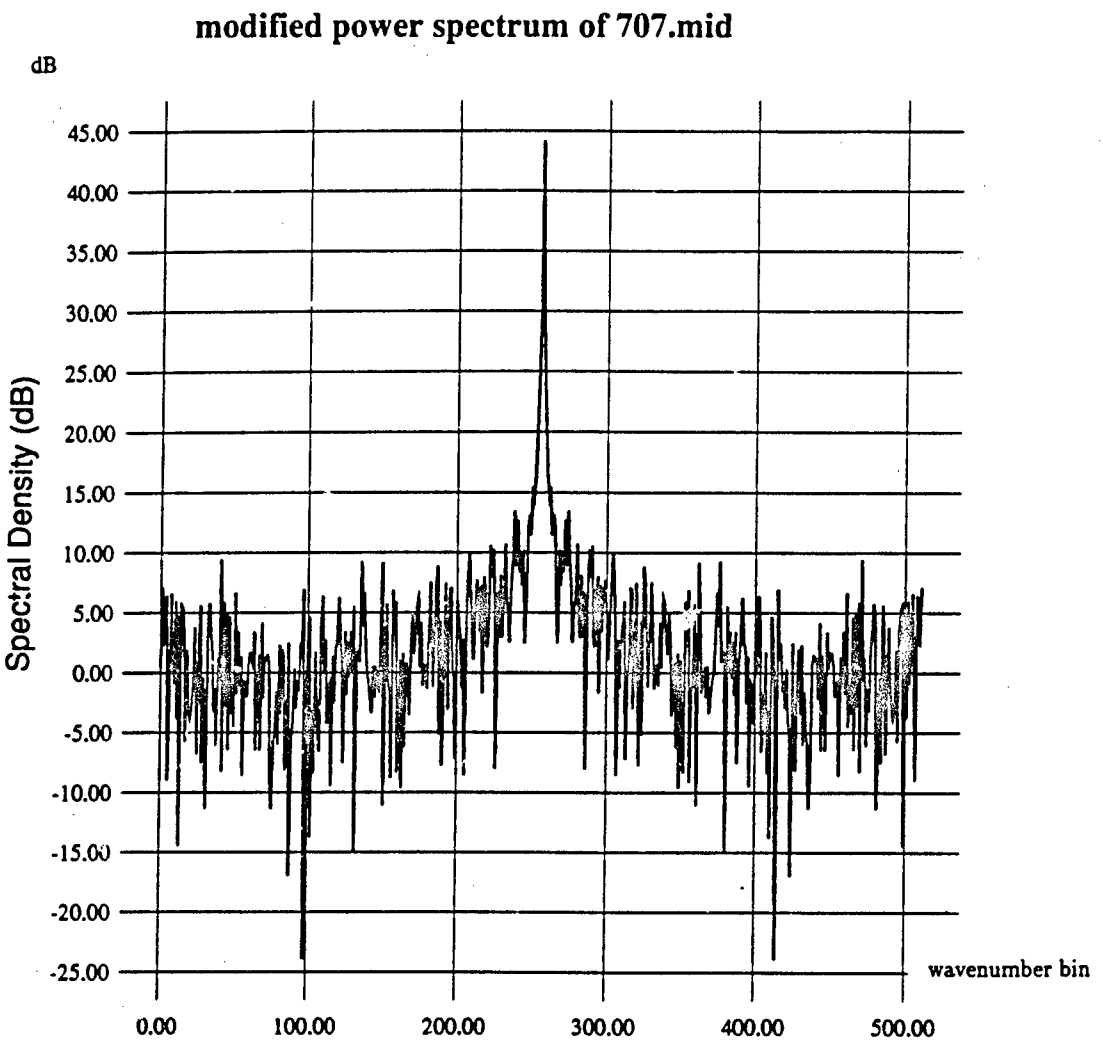

Figure 4-6. A Cut Through the Collected SAR Image Filtered Power Spectrum Along the Azimuth Wavenumber

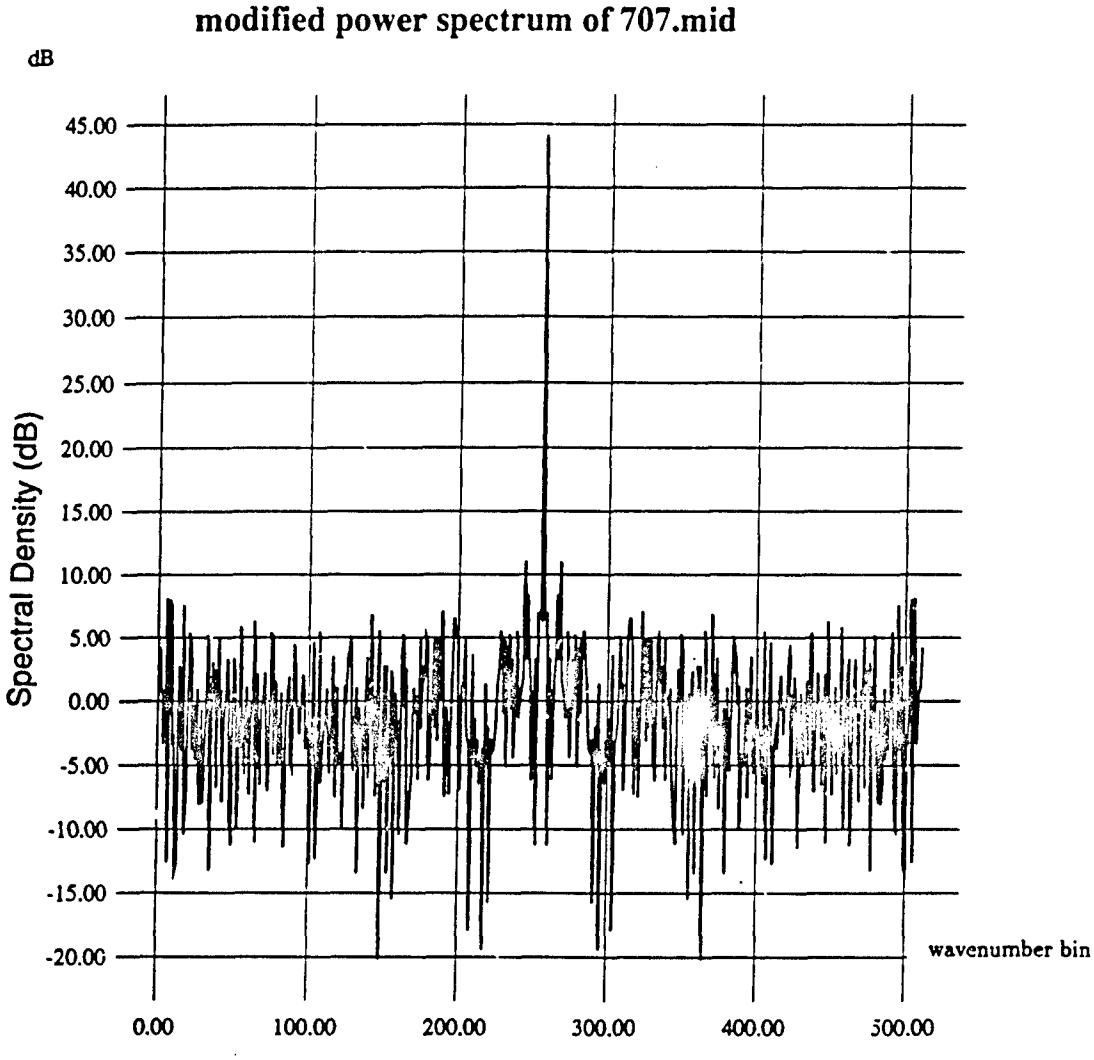

Figure 4-7. A Cut Through the Collected SAR Image Filtered Power Spectrum Along the Range Wavenumber dc

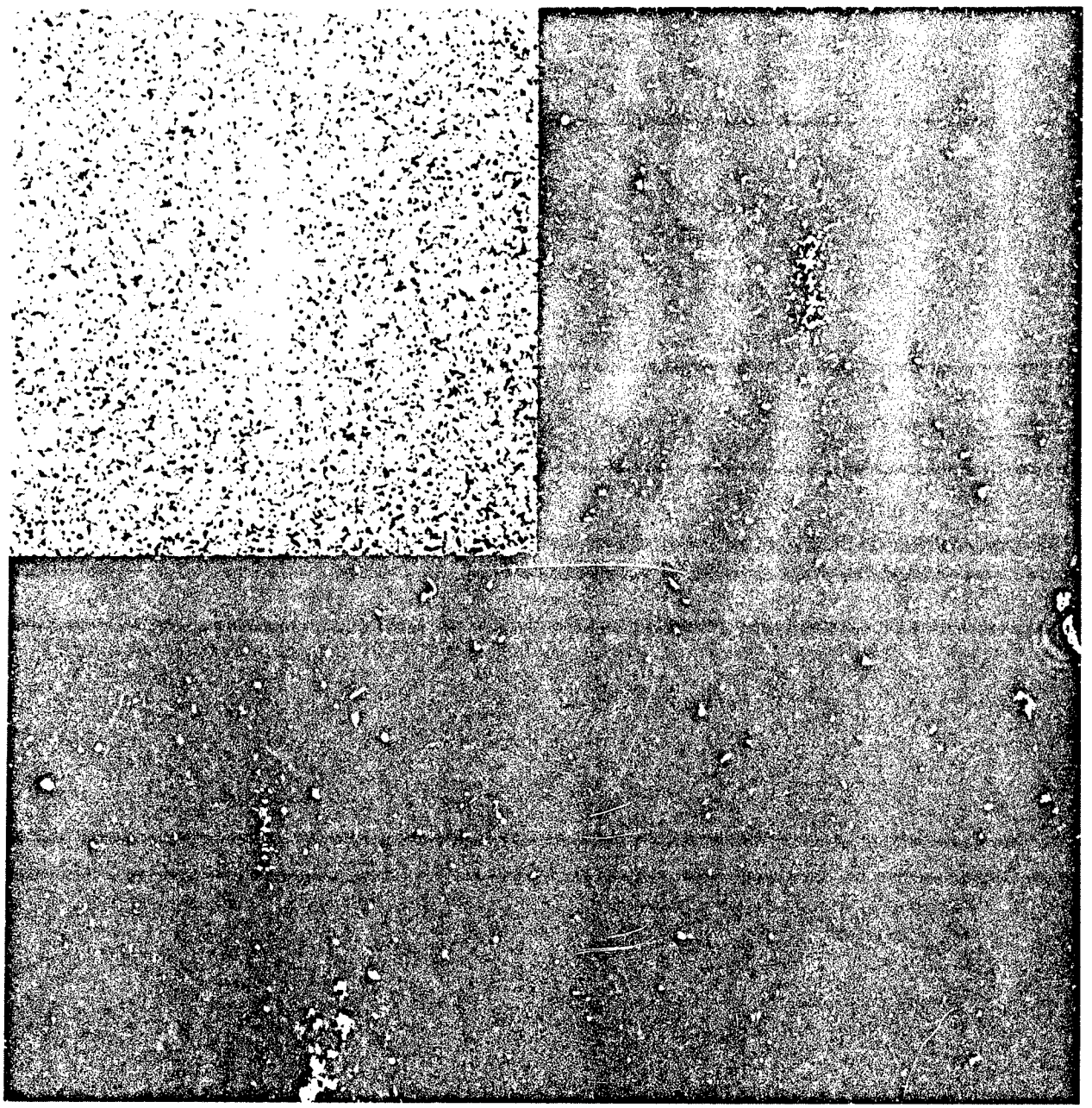

Figure 4-8. Filtered SAR Image Power Spectrum After Thresholding at (Upper Left) One, (Upper Right) Three, (Lower Left) Five, and (Lower Right) Seven Times the Estimated Mean Value of the Noise Floor. All Data are Displayed on a 60 dB Scale Fixed at the Maximum in the Individual Data Set. The Color Scale Runs From Black and Purple at the Low End to Red at the High End. Green is in the Middle of the Scale.

filtered power spectrum at seven times the mean may remove some signal component. More work needs to be done to determine the optimum threshold level.

4.1.2. MTF Analysis

The two-dimensional image spectra for the ambient waves in passes 6-4, 7-2, and 7-4 on 28 January 1989 are shown in Figures 4-9 through 4-11. These spectra were obtained from image subsets centered at an incidence angle of approximately 55 degrees, and a range distance of about 5.4 km in each image. The primary difference from pass to pass is the orientation of the flight path with respect to the direction of the dominant wave pattern, which appears to be roughly coincident with the wind direction of 300°. Thus, the dominant wave direction was approximately in the range direction during run 6-4, and was roughly 45 degrees on either side of the range direction during runs 7-2 and 7-4. Both HH and VV imagery were collected during all three runs. Since the ambient wave spectrum was roughly the same for all three passes, the differences among the image intensity spectra can be attributed to variations in the SAR response function with collection geometry and polarization.

The behavior of the image intensity spectrum was investigated as a function of azimuth angle and polarization. To examine this behavior, the image intensity spectrum was integrated over wavenumber and plotted as a function of azimuth angle. The spectra were integrated in wavenumber between $2\pi/150$ rad/m and $2\pi/50$ rad/m in order to encompass the peak wavenumber. The integrated spectra for HH and VV polarization are given in Figures 4-12 and 4-13 respectively. As can be seen from the figures, the integrated spectra have distinctly different shapes for different look directions and polarizations.

One particularly interesting feature of the integrated spectra is the deep null observed near the range wavenumber axis in run 6-4. This effect was first observed

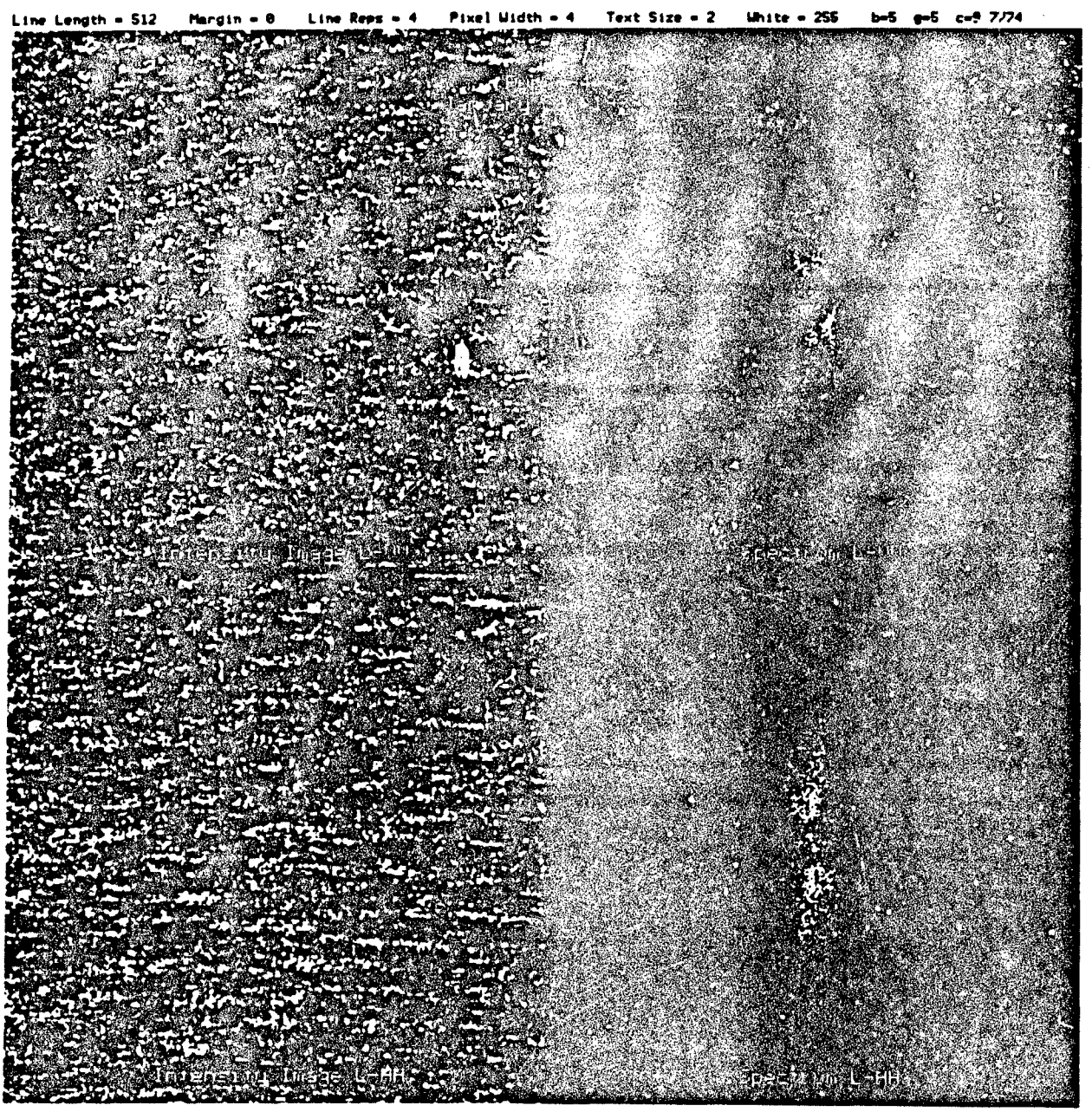

Figure 4-9. L-VV and L-HH Image Subsets and Image Spectra Extracted From Run 6-4

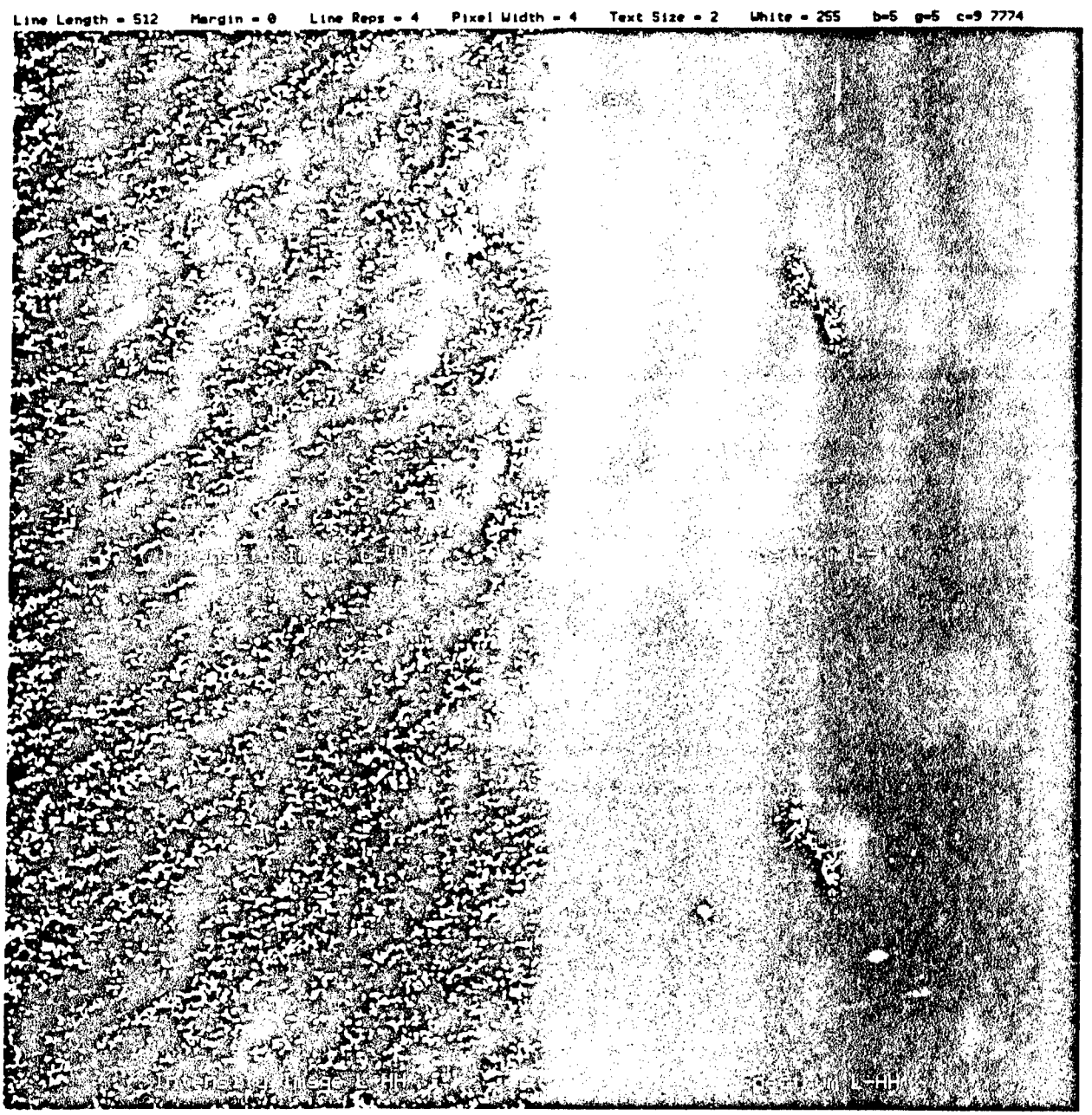

Figure 4-10. L-VV and L-HH Image Subsets and Image Spectra Extracted From Run 7-2

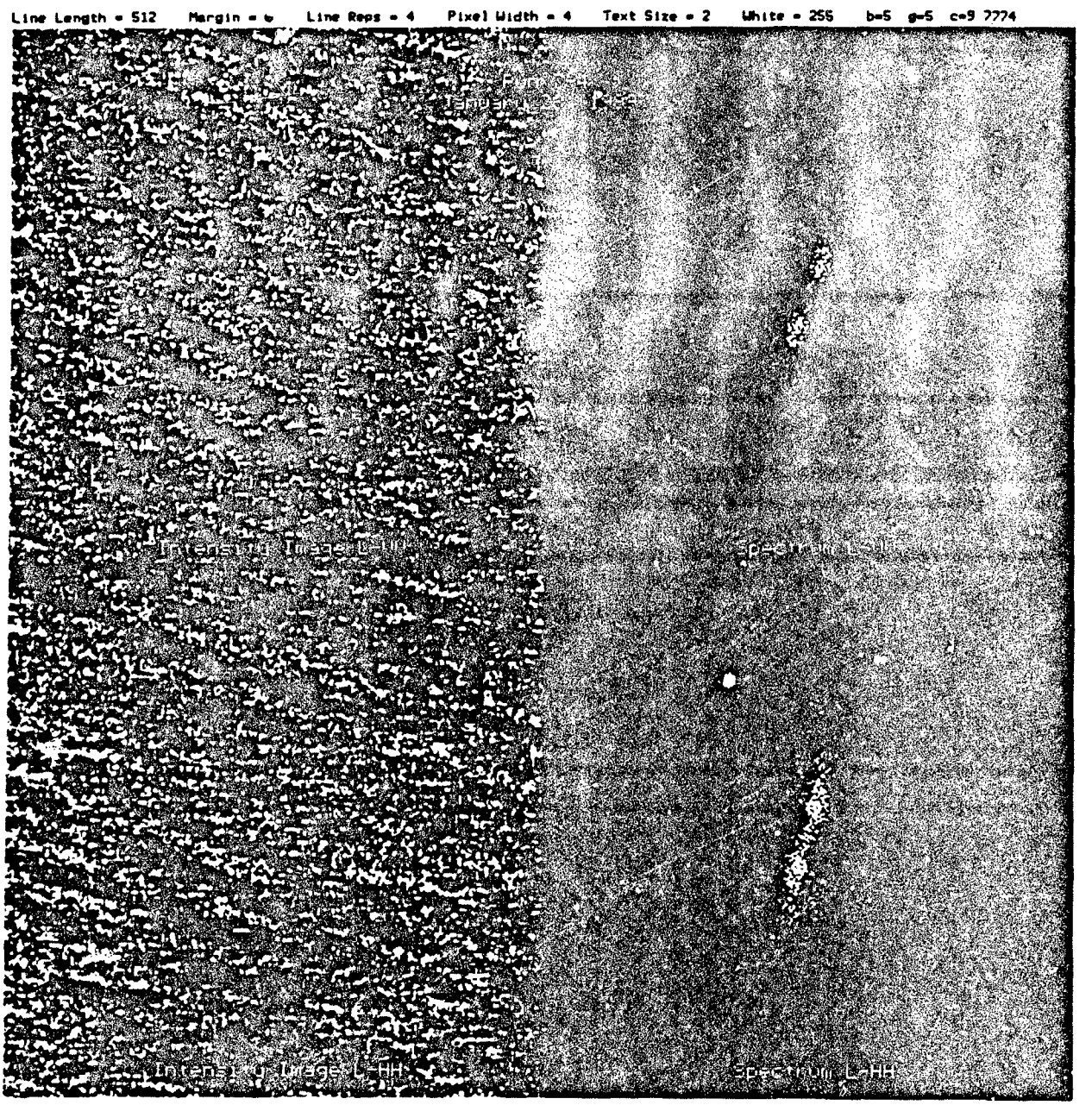

Figure 4-11. L-VV and L-HH Image Subsets and Image Spectra Extracted From Run 7-4

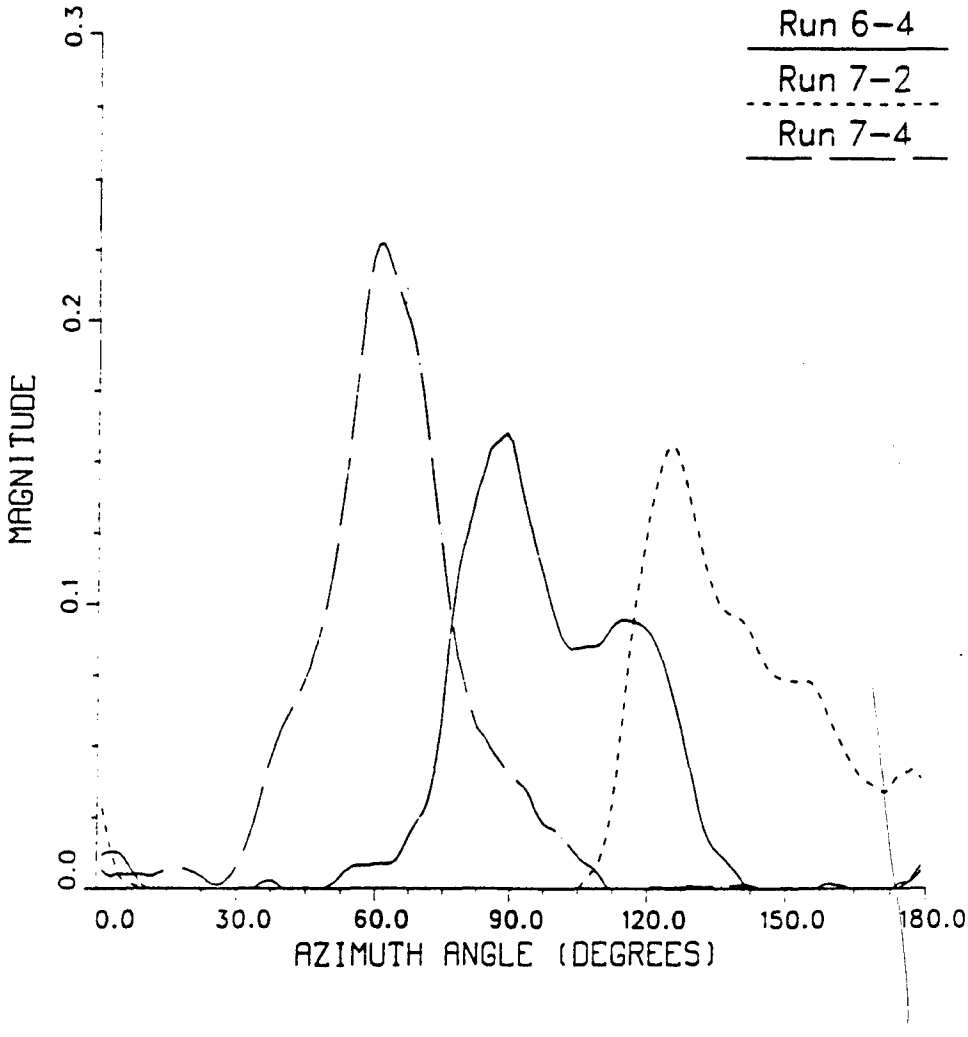

Figure 4-12. Empirical HH Image Spectra From Runs 6-4, 7-2 and 7-4 Integrated Over Wavenumber

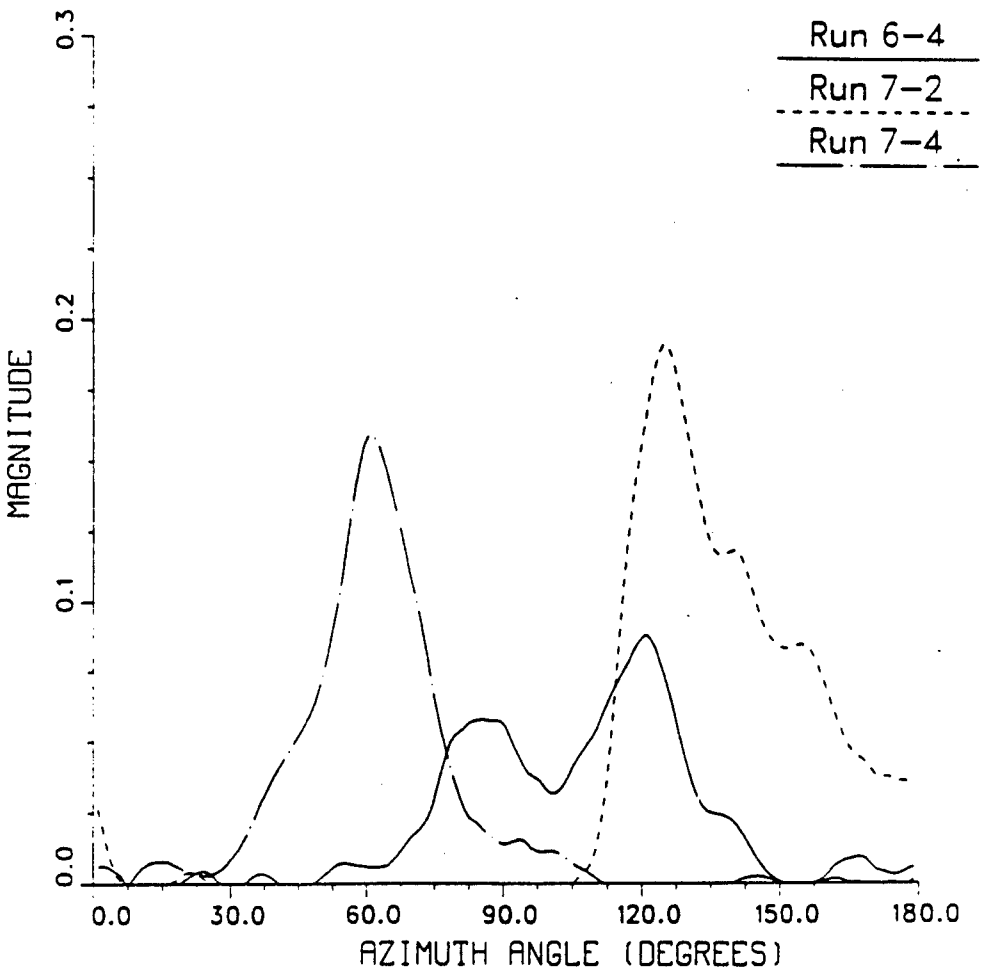

Figure 4-13. Empirical VV Image Spectra From Runs 6-4, 7-2 and 7-4 Integrated Over Wavenumber

by Bruning et al (1988) and was attributed to an interference effect in the SAR modulation transfer function (MTF). Note that the null in the VV spectrum is deeper than that in the HH spectrum. Another observation is that the peaks of the integrated spectra for runs 7-2 and 7-4 are less than 90° apart, indicating that these spectra are rotated toward the range direction.

To investigate the angular variations of the image intensity spectra shown in Figures 4-12 and 4-13, the image intensity spectrum was simulated by assuming a simple form for the wave height spectrum and multiplying by the SAR MTF discussed in section 2.1. The same height spectrum was used to simulate the intensity spectrum for all three passes, thus variations in the shape of the intensity spectrum that we calculate using this procedure are due to variations in the MTF. From the discussion in section 2.1, we would expect this procedure to be valid if $RK_xV_r/V < 1/2$.

The R/V ratios for the image subsets used to calculate the spectra in Figures 4-12 and 4-13 are 37.8 sec for run 6-4, 35.3 sec for run 7-2, and 43.4 sec for run 7-4, the variation being due primarily to differences in the platform velocity. An estimate of the maximum radial velocity can be obtained by noting that for a Pierson-Moskowitz spectrum the ratio of the velocity variance σ_v^2 to the height variance σ_h^2 is approximately 60 f_o^2 where f_o is the peak frequency. Using $f_o=0.125$ Hz and $\sigma_h=0.25$ m, we obtain $\sigma_v=0.24$ m/sec. Equating σ_v with V_r, the parameter $\alpha=RK_xV_r/V$ has the value 0.46 at the peak of the spectrum for run 7-4, which is the "worst case" (largest R/V). We can therefore expect the linear imaging model to be valid for wavenumbers near the spectral peak, although it is approaching the limits of its validity in some cases.

In order to test the predictions of this theory, the wave height spectrum was modeled as a simple gaussian function

$$S_w(K_x,K_y) = A \exp\{-[(K_x-K_{xo})^2+(K_y-K_{yo})^2]/2\sigma_k^2\} \quad (18)$$

having a width σ_K and centered at the wavenumbers $K_{xo}=K_c\cos\phi_o$ and $K_{yo}=K_o\sin\phi_o$, where K_o is the peak wavenumber and ϕ_o is the peak direction. The peak wavelength was chosen as 80 meters, based on the observed location of the peak in the image spectrum, and the other parameters were iterated to yield the best fit to the observed angular spectra. This iteration resulted in ϕ_o being chosen as 5° from the nominal wind direction, and the spectral width being chosen as $\sigma_K=0.0313$ rad/m. The amplitude A was taken as 1.0×10^{-3} m^4. The modeled wave height spectra integrated over wavenumber are plotted in Figure 4-14 as a function of the azimuth angle relative to the flight direction for each pass.

To model the image intensity spectrum, the wave height spectrum was multiplied by the squared magnitude of the SAR MTF defined in section 2.1. The coherence time τ_c was taken to be 0.05 sec. The resulting integrated image intensity spectra for HH and VV polarization are shown in Figures 4-15 and 4-16, respectively. Note that qualitatively, the behavior of the spectra as a function of azimuth angle and polarization in Figures 4-15 and 4-16 is essentially the same as the behavior of the spectra in Figures 4-12 and 4-13. The shape and relative amplitude of the modeled spectra show the same variation with polarization and azimuth angle as the spectra extracted from the actual imagery. Most notably, the modeled spectra for Run 6-4 show the null about the range direction, with the null in the VV spectrum being deeper than the null in the HH spectrum.

The behavior of the spectra as a function of azimuth angle and polarization can be simply explained by examining the HH and VV modulation transfer functions, which are shown in Figures 4-17 and 4-18 respectively. Both the HH and VV MTF show a null about the range direction, and both have gentle humps on either side of the range

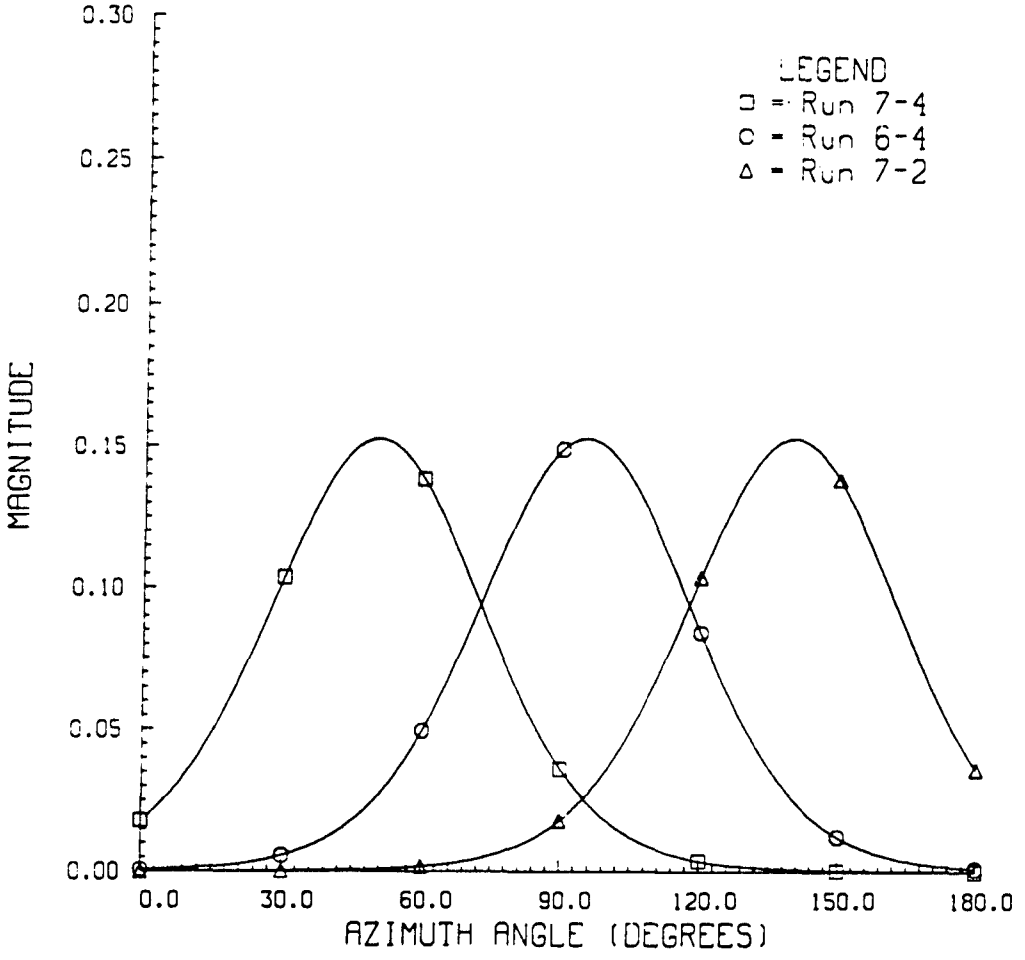

Figure 4-14. Wave Height Spectrum Model for Runs 6-4, 7-2 and 7-4 Integrated Over Wavenumber

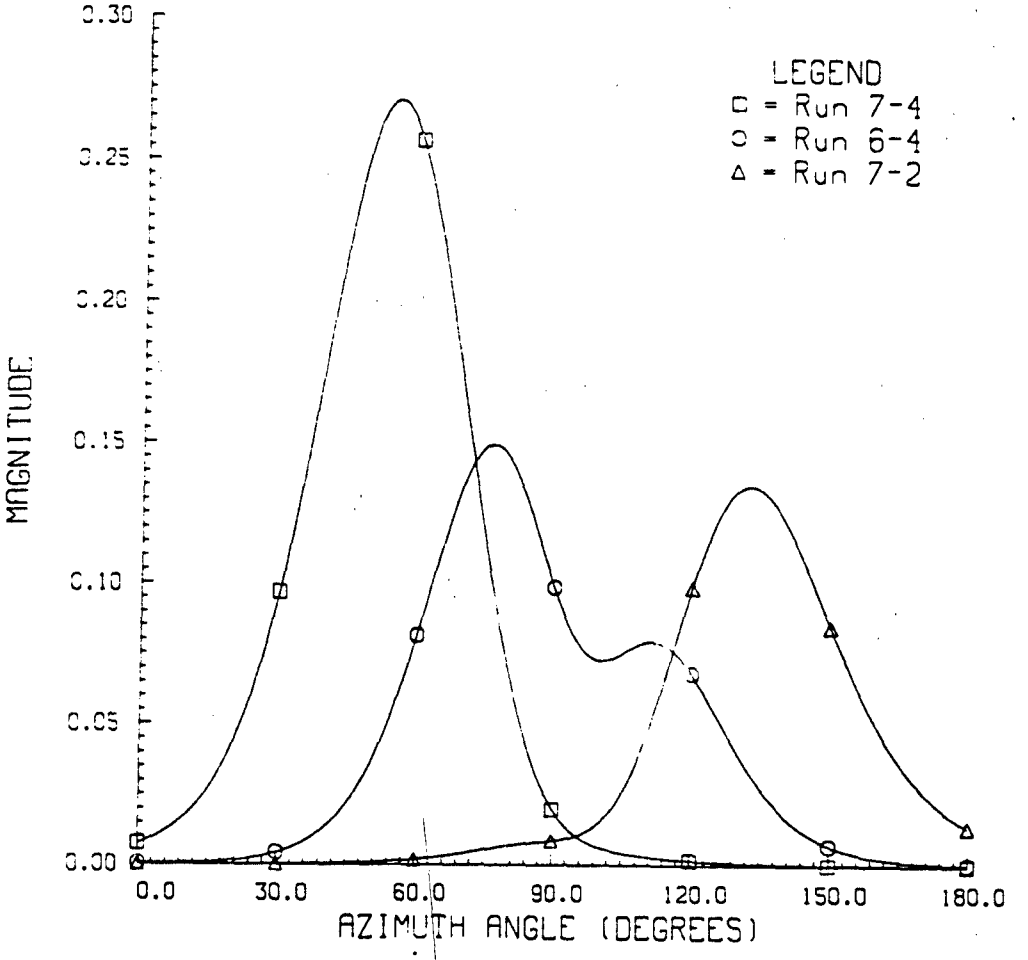

Figure 4-15. Modeled HH Image Spectra for Runs 6-4, 7-2 and 7-4 Integrated Over Wavenumber

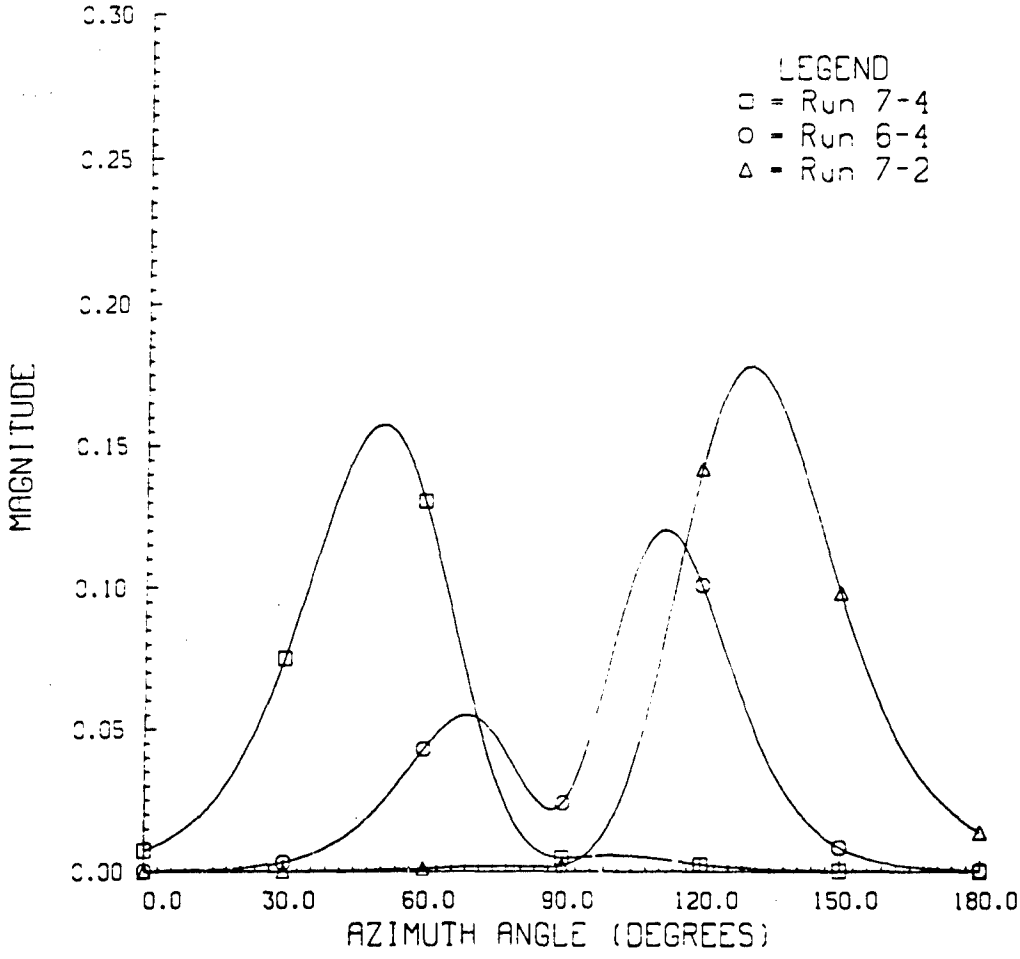

Figure 4-16. Modeled VV Image Spectra for Runs 6-4, 7-2 and 7-4 Integrated Over Wavenumber

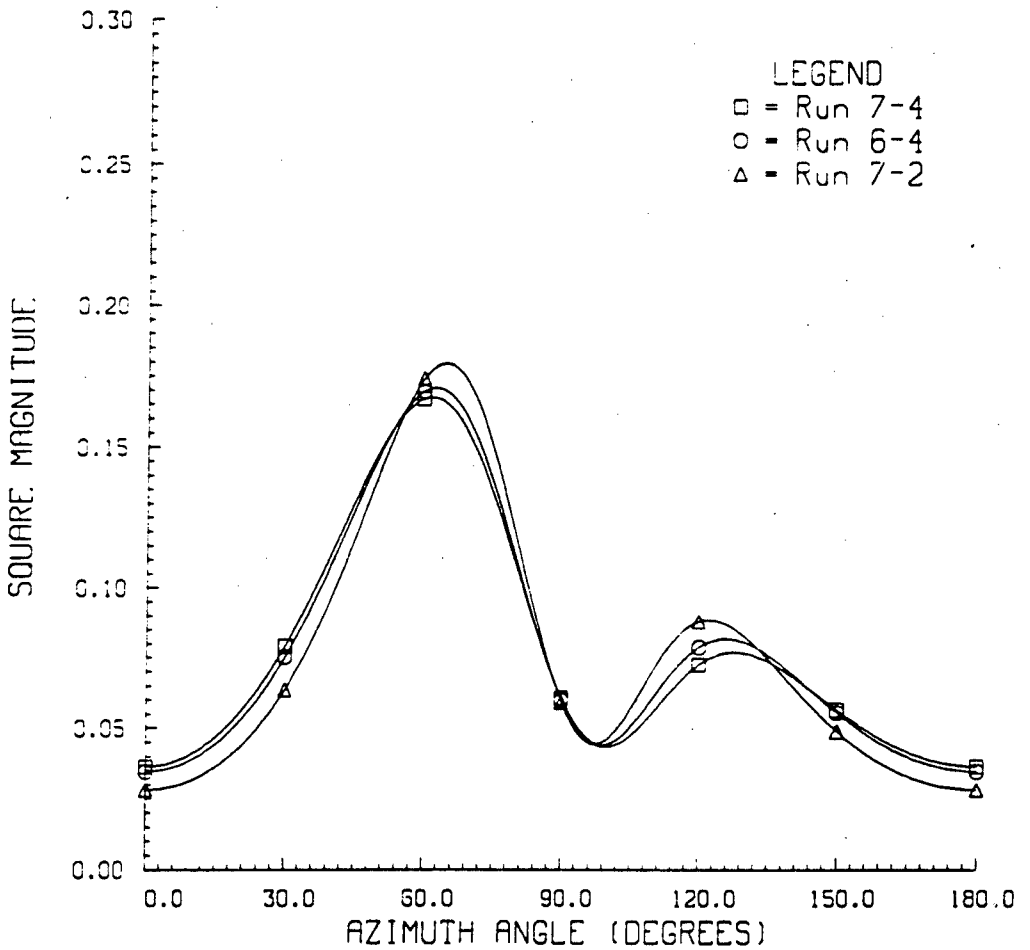

Figure 4-17. Magnitude Squared of HH MTF for Runs 6-4, 7-2 and 7-4 Integrated Over Wavenumber

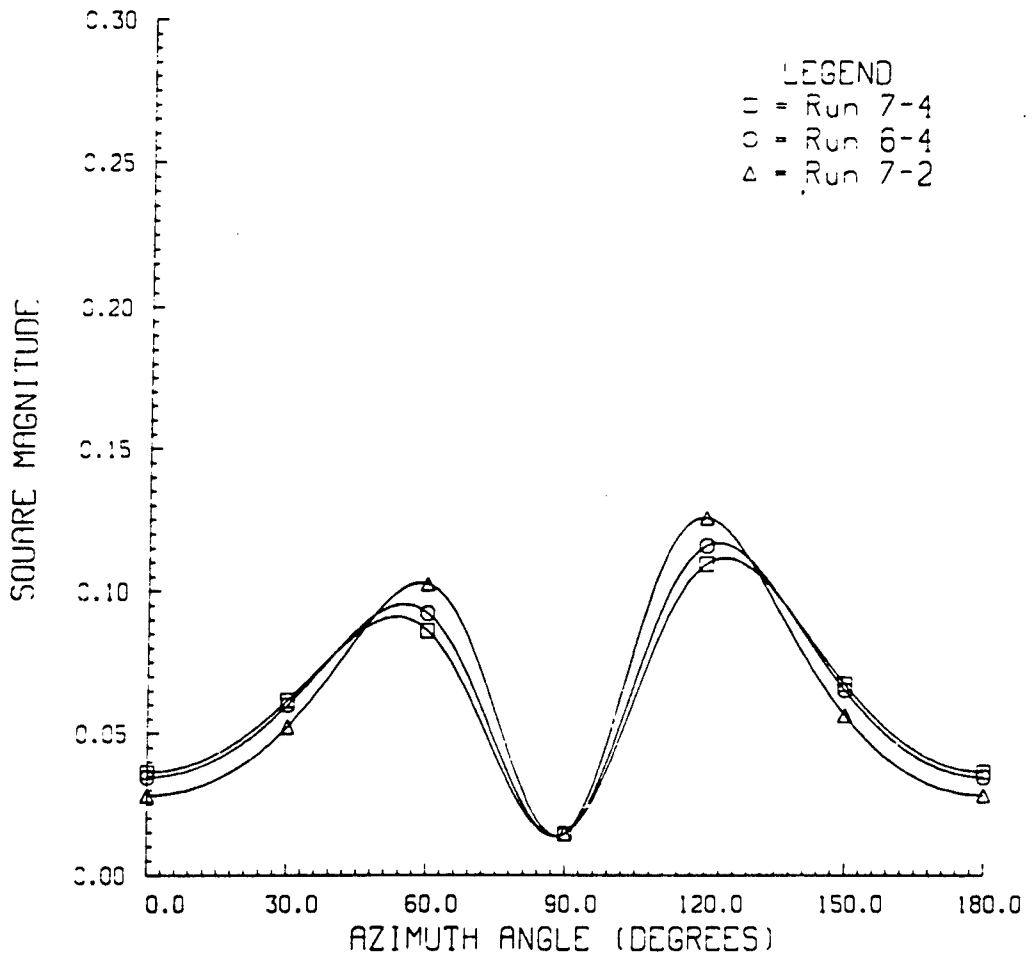

Figure 4-18. Magnitude Squared of VV MTF for Runs 6-4, 7-2 and 7-4 Integrated Over Wavenumber

direction. The hump for angles less than 90° is larger than the hump for angles greater than 90° in the case of HH polarization, while the opposite is true for VV polarization.

Comparing Figures 4-16 and 4-18 with Figures 4-15 and 4-16 respectively, it can be seen that there is a direct correlation between the angular behavior of the image spectra and the angular behavior of the MTFs. For instance, the peak of the HH image spectra for Run 7-4 is larger than that for Run 7-2 since the HH MTF is larger for azimuth angles less than 90°. Similarily, the null in the Run 6-4 VV image spectrum is deeper than the null in the HH image spectrum since the null in the VV MTF is deeper than that in the HH MTF.

The asymmetrical behavior of the MTFs as a function of azimuth angle is interesting since the magnitude of the individual components of the MTF are symmetric about the range direction, as shown in Figure 4-19. The asymmetrical sum of the component MTFs results from the phasing of the individual components. Tests showed that the angular behavior of the MTF, and thus the angular behavior of the image spectrum, could be significantly altered by simply varying the phasing of the individual MTF components.

4.2. WAVE AMPLITUDE ESTIMATION

Having gained some confidence in the linear imaging model as well as the parameters entering this model, we now consider the inverse problem of estimating wave amplitudes from SAR images. The general procedure we followed was to Fourier transform the image intensity, make corrections for the SAR MTF in the wavenumber domain while maintaining the phase of the Fourier transform, and then inverse transform to obtain an estimate of the surface height field. However some

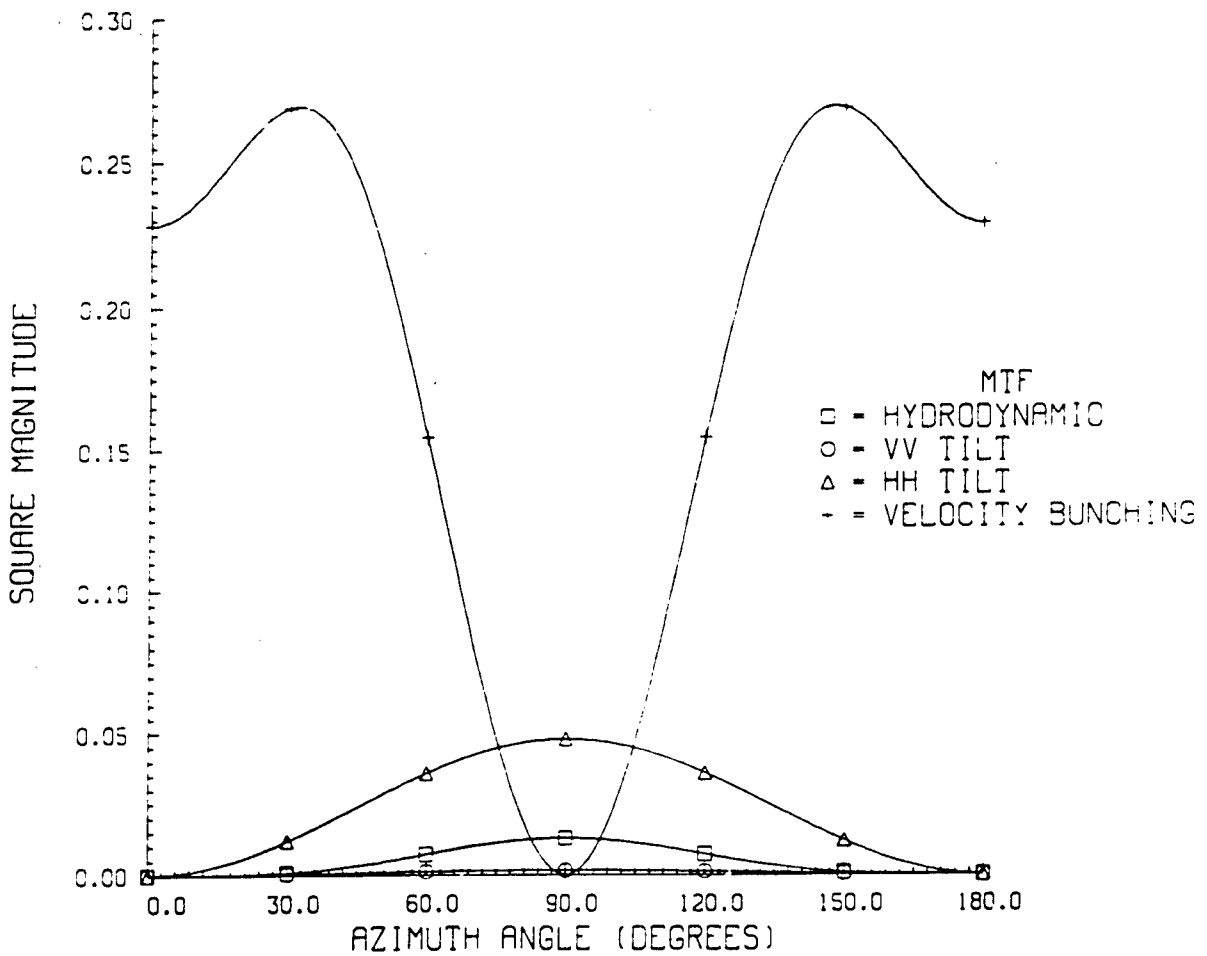

Figure 4-19. Magnitude Squared of Component MTFs for Run 6-4 Integrated Over Wavenumber

preliminary processing steps were also required, as described in the following paragraph.

The received SAR intensity (magnitude squared) image I(x,y) is first resampled from the slant plane to the ground plane. This ground-sampled data is then passed through a median filter to estimate the large scale trends which appear in the imagery due to either antenna pattern weighting or large scale scattering changes across the image. The application of the median filter is simply a moving box across the image in which the value of the center pixel of the box is replaced with the median value of the surrounding data. For this analysis, the moving box had an extent of about 200 meters in azimuth and 200 meters in range. The images used for this analysis cover approximately 3 kilometers in the azimuth direction and 3 kilometers in the range direction. A median filter was used as opposed to a boxcar filter because the median filter retains sharpness of features (e.g. the centerline wake) whereas the boxcar filter smooths these features out. The unfiltered image is then divided by the filtered image on a pixel-by-pixel basis to generate a "flattened" image. Clearly this process removes low frequency information from the image, however, the range of wavenumbers occupied in the Fourier space by the Kelvin wake is far above those filtered. This filtered image is then normalized to have unity mean and the FFT is generated.

Recall from Section 2.3 that the Kelvin wake occupies a narrow hourglass shape in the spectrum whose position is described by the ship speed and heading. To estimate the Kelvin wave height, the spectral energy due to the Kelvin wake needs to be extracted so that the inverse transform can be taken to generate a "waveheight image". The algorithm for extracting the Kelvin spectral energy is straightforward. The energy along the Kelvin wake is summed as a function of wavenumber along the wake response. Note that the ship velocity displaces the hourglass shape closer to and further away from the DC for higher and lower ship speeds respectively. A one-half

knot width surrounding the actual ship speed will sufficiently contain the Kelvin energy in the spectrum (i.e. for a ship traveling at 22 knots, the energy is summed over a wavenumber range corresponding to a velocity of 22 $\pm$ .25 knots at the specified heading). This energy is summed separately for both positive and negative propagation angles, (i.e. both arms of the wake). Once the energy is calculated as a function of wavenumber, the values in each wavenumber bin are normalized for the number of contributors to that bin so that an average energy level is calculated for the spectrum. In a likewise manner, the Kelvin waveheight spectrum can be calculated as a function of spectral angle $\phi = \tan^{-1}(K_y/K_x)$ as well.

A correction was also made to remove any spectral bias present that might contribute energy to the Kelvin spectral response. If the spectra of interest were from wavefields with a distributed range of wavenumber components one might refer to the algorithms described earlier to estimate the spectral bias. Because the Kelvin wake has a very narrow spectral response, the approach for estimating the Kelvin waveheight spectrum can be extended to estimate the ambient spectrum. The approach taken is to generate an ambient spectrum over the Kelvin hourglass shape, but at speeds which are the known ship speed $\pm$ 2 knots. It is assumed that the ambient spectrum will not change significantly over the 4 knot width used to estimate the different waveheight spectra. This assumption has been validated for the data examined. Note that for different ship speeds, the range of wavenumbers covered by the hourglass shape vary. To allow for a direct comparison between the different waveheight estimates (both the wake and the background estimates) it is necessary to normalize the different spectra to have equivalent wavenumbers. This is accomplished by scaling the wavenumbers for each spectrum by

$$k' = kV_s^2/g. \tag{19}$$

This normalization allows direct comparison to be made between the different waveheight spectra. If the data is generated as a function of spectral angle, no normalization is necessary. Once the background waveheight spectra have been generated, they are averaged together to generate a single spectral background estimate. This background estimate is smoothed and subtracted from the slightly smoothed Kelvin wake waveheight spectrum to generate a final waveheight spectrum estimate. An example of the waveheight spectra as a function of angle is shown in Figure 4-20 where the energy calculated over the Kelvin response is shown along with the ambient spectrum estimate. The same spectrum plotted as a function of normalized wavenumber, k', is shown in Figure 4-21.

To generate the actual 2-dimensional waveheight image it is necessary to use the two dimensional complex FFT. The 2-D FFT is bandpassed over the Kelvin hourglass shape with a spectral width corresponding to the $\pm$ 0.25 knots described earlier. The spectral background estimate is then subtracted over this band to generate the final two-dimensional FFT. Because the FFT is complex and contains essential phase information, the subtraction is performed using the intensity of the data. This data is then converted back to complex form by taking the square root of the intensity and applying the phase of the original FFT to each pixel.

At this point the correction for the SAR MTF is finally made. Because the MTF is not symmetric it is important to know which quadrants of the modeled transfer function are effecting the actual spectrum. Each quadrant of the MTF represents a particular wave direction. A visual examination of the data indicates which quadrants of the MTF should be used (based on the ship heading) and a Hermitian version of the MTF is generated by mirroring the chosen quadrants and conjugating. This MTF is coherently divided out of the existing wake spectrum to generate a final estimate of the 2-D Kelvin waveheight spectrum. The data is inverse transformed after zeroing out the DC term and the real part of the output represents the actual waveheight.

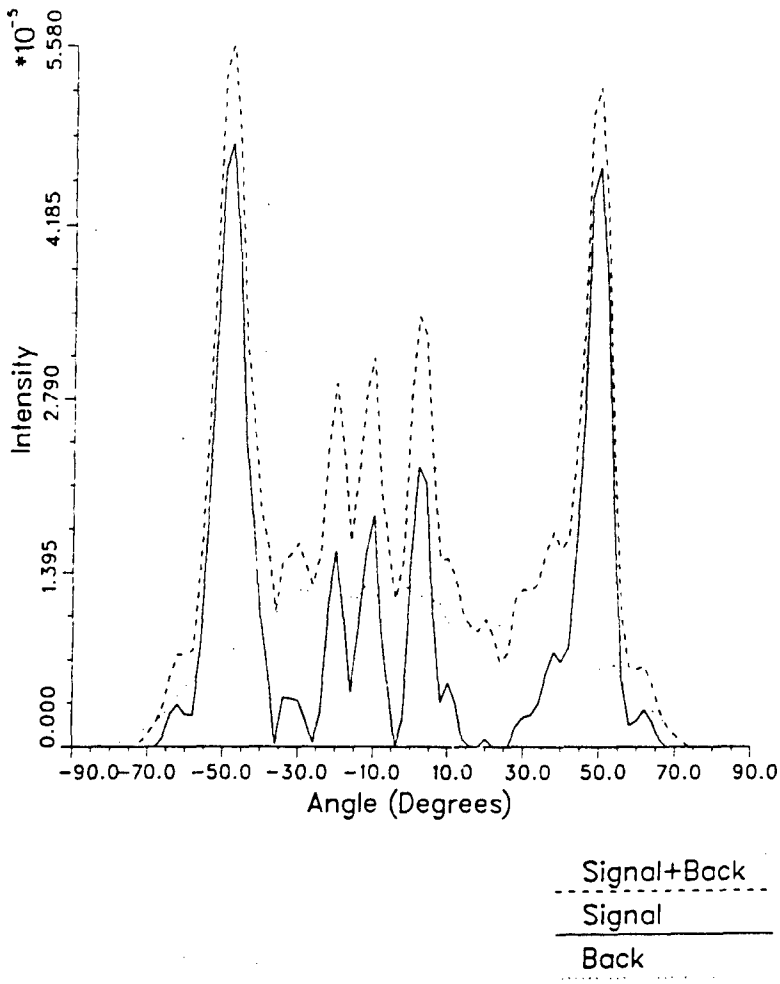

Figure 4-20. Image Spectral Densities Along Kelvin Wake, Plotted Versus Wake Angle

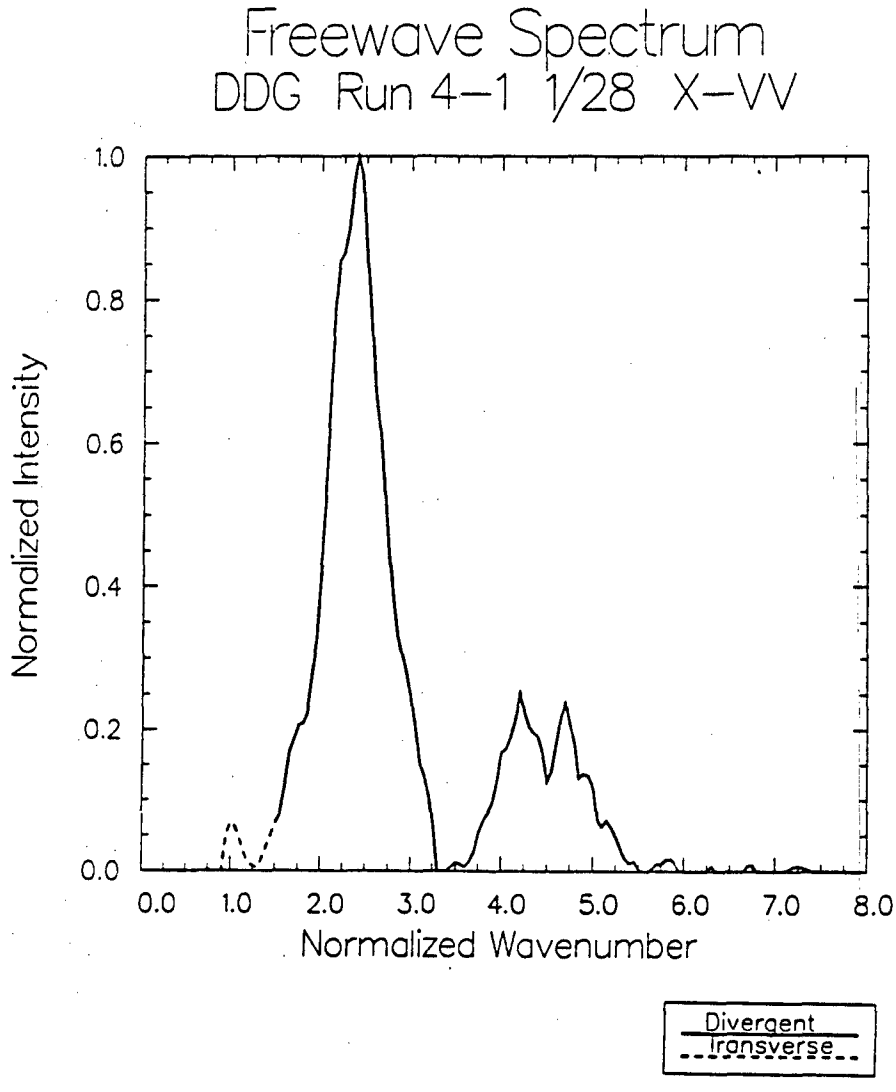

Figure 4-21. Image Spectral Densities Along Kelvin Wake, Plotted Versus Normalized Wavenumber

Scans are generated over the wake feature to examine the waveheight (which is in units of meters) over the cusps of both wake arms.

4.2.1. Ambient Wave Results

A measurement of the ambient surface waveheight was made using the described algorithm to verify its capability. The ambient data for Run 7-4 was chosen as a test case because a relatively large wave field could be extracted without interference from the Kelvin wake. The data set for this test was extracted at a 61 degree incidence angle with an R/V ratio of 42 seconds. The spatial extent of this data is 1.5 km in azimuth and 2.5 km in ground range.

The normalized image intensity was generated for both X-band and L-band data as described above. The Fourier transform was generated and a mean background level was removed from the spectra to compensate for the speckle contribution. This background value was calculated as the mean spectral value in a homogeneous area near the peak spectral response. Naturally, the speckle level will be over-estimated at the higher wavenumbers and under-estimated at the lower wavenumbers due to the system impulse response. This will not effect the measurement significantly, however, because the bandpass region chosen is taken over the spectral peak and has a small wavenumber extent. The estimated SAR MTF effects are removed using the previously described model. The data is symmetrized and a bandpass region is chosen which surrounds the peak ambient spectral response. The peak wavelength was measured to be 88 m at an angle of 65 degrees from azimuth. The bandpass for this data was taken to be a small spectral box surrounding the peak spectral response with an azimuth wavenumber extent of 0.057 rads/m and a range wavenumber extent of 0.038 rads/m. The data was then inverse transformed to form the waveheight image. The original image intensities are shown in figures 4-22 and 4-23 with the

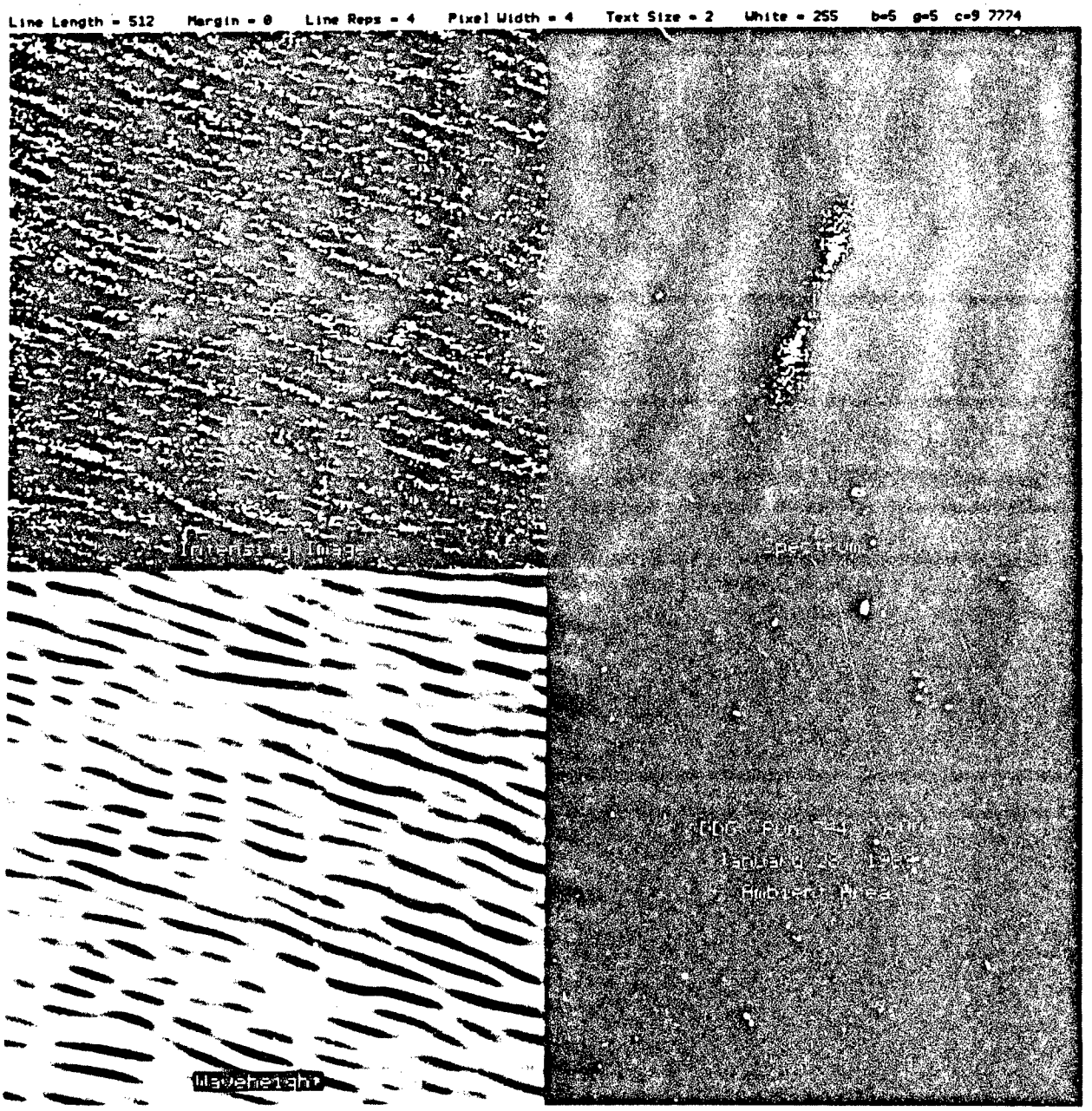

Figure 4-22. (a) Image Subset, (b) Image Spectrum, and (c) Wave Height Image for Run 7-4, X-VV

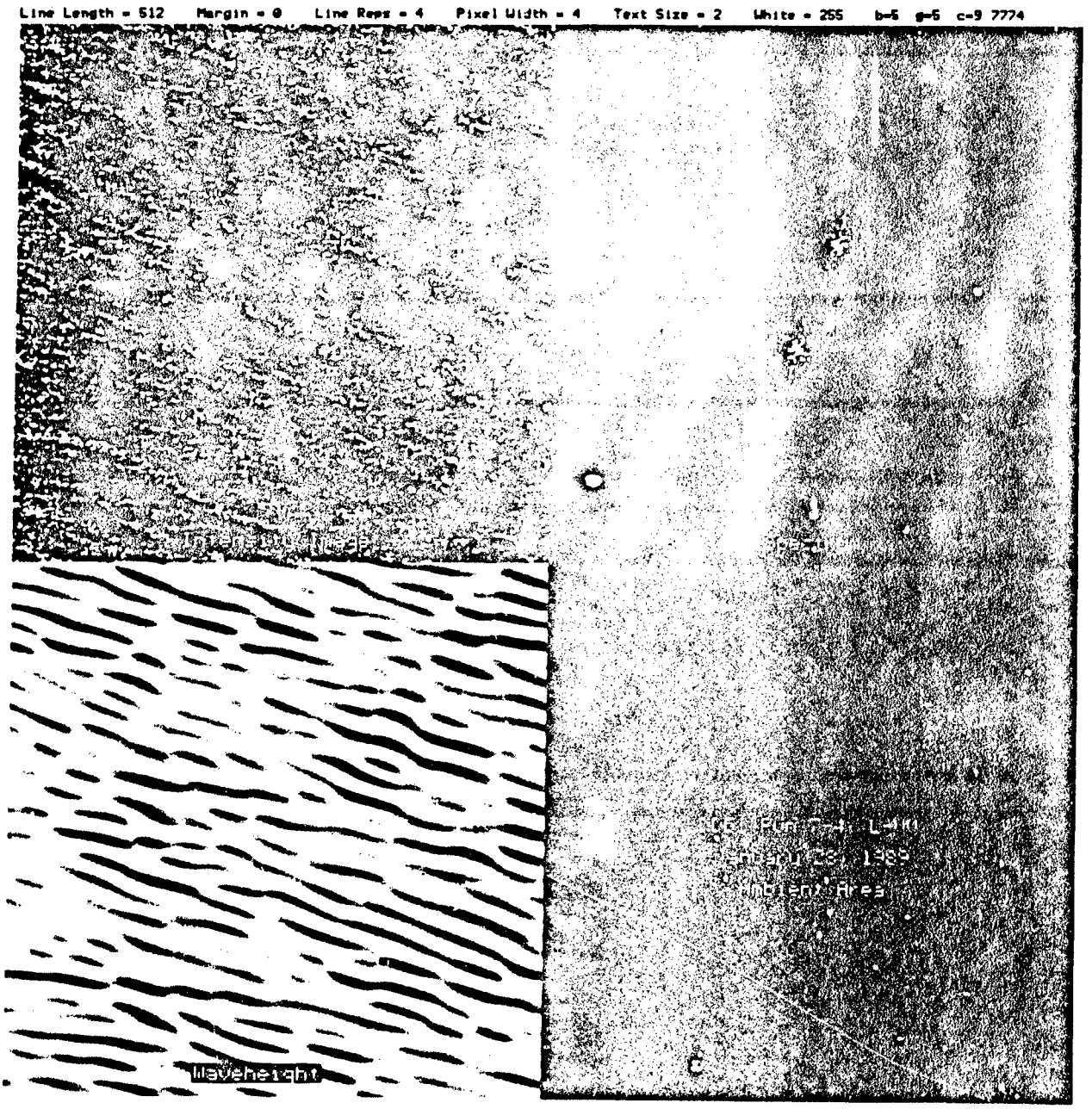

Figure 4-23. (a) Image Subset, (b) Image Spectrum and (c) Wavcheight Image for Run 7-4, L-VV

resulting spectra and waveheight images. The RMS value of the waveheight is calculated over the entire image to be 0.222 m at X-band and 0.200 m at L-band. These values compare well with the value of 0.23 m measured *in situ* (Gasparovic, 1989). The waveheight estimated from the X-band image data compares well to the waveheight measured *in situ* although the L-band estimate is slightly lower than the *in situ* values. Scans through this wavefield are shown in Figures 4-24 and 4-25. A possible cause for the reduced waveheight may be a misfocussing of the waves due to larger integration times at L-band.

An important parameter in the MTF model is the standard deviation of the r.m.s. surface velocity, σ_v which is a function of windspeed and affects the azimuthal cutoff of the spectrum. This value is unknown for this data set and as a result, waveheight measurements were generated for a range of σ_v values at X-band to determine how sensitive the measured waveheight is to σ_v. Figure 4-26 shows how the MTF amplitude changes as a function of σ_v. Note that the azimuth bandwidth (azimuth is horizontal) decreases quickly with increasing σ_v which indicates that as the wind speed increases, the shorter-scale azimuth-travelling waves cannot be resolved. Figure 4-27 contains the measured waveheight as a function of σ_v. This curve indicates that the measured long-scale waveheight is somewhat insensitive to r.m.s. velocity variations. This result is obtained because the waves are close to range traveling in direction. As the wavefronts become more azimuth traveling, the azimuth cut-off would significantly effect the ability to resolve the shorter waves.

4.2.2. Kelvin Wake Results

The algorithm was applied to three data sets which contain Kelvin wakes. These data sets all contain destroyer (DDG) wakes with two containing azimuth traveling ships (one being near-shore, one off-shore) and the last, a range-traveling case.

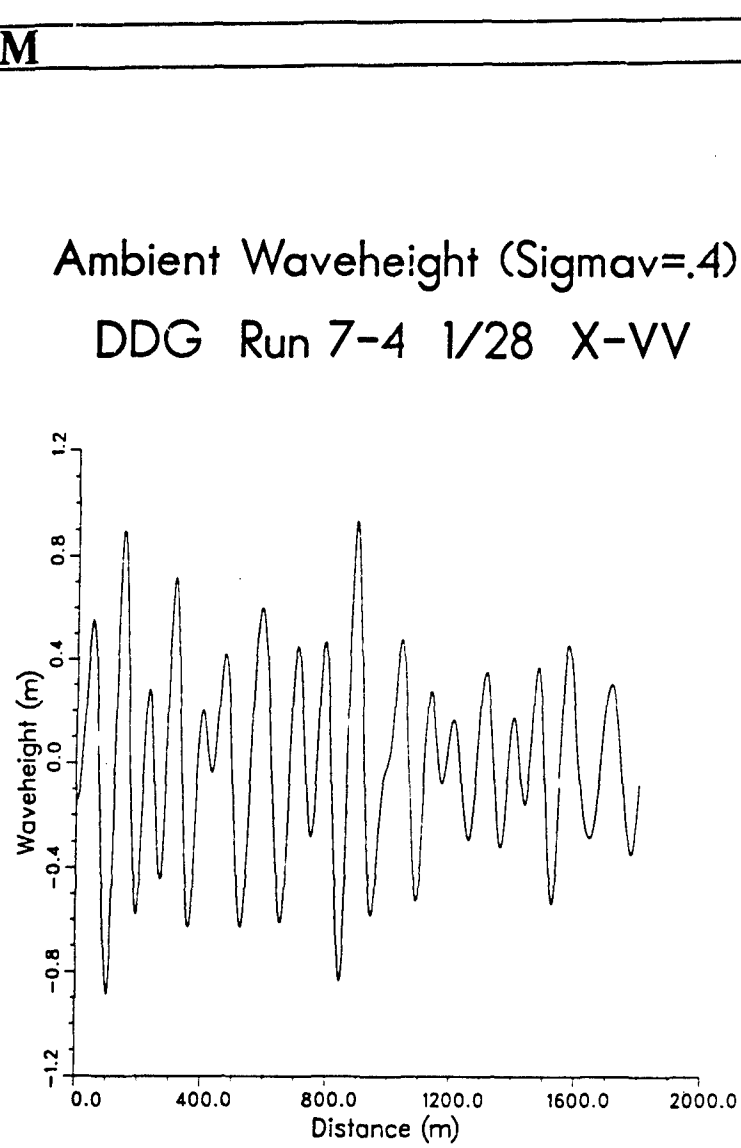

Figure 4-24. Ambient Waveheight Scan for Run 7-4, X-VV

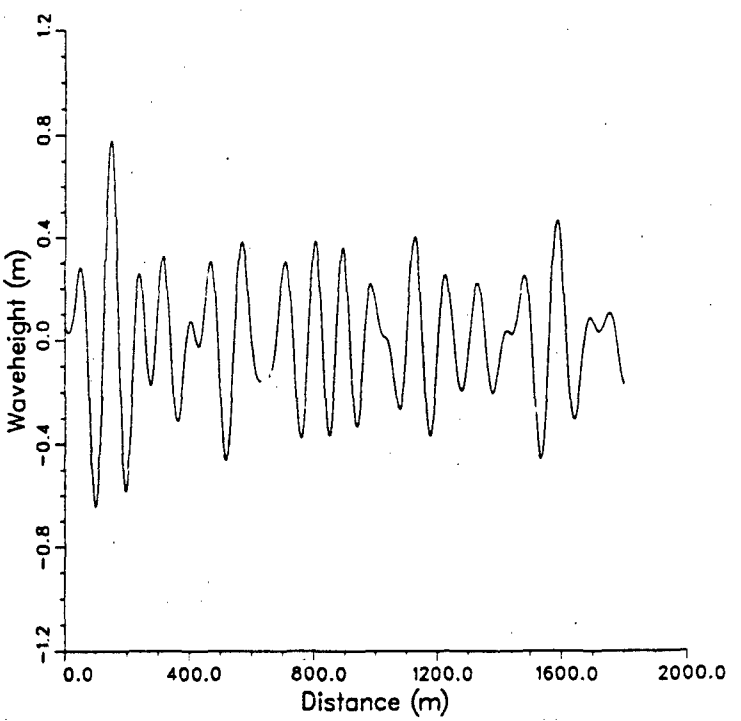

Figure 4-25. Ambient Waveheight Scan for Run 7-4, L-VV

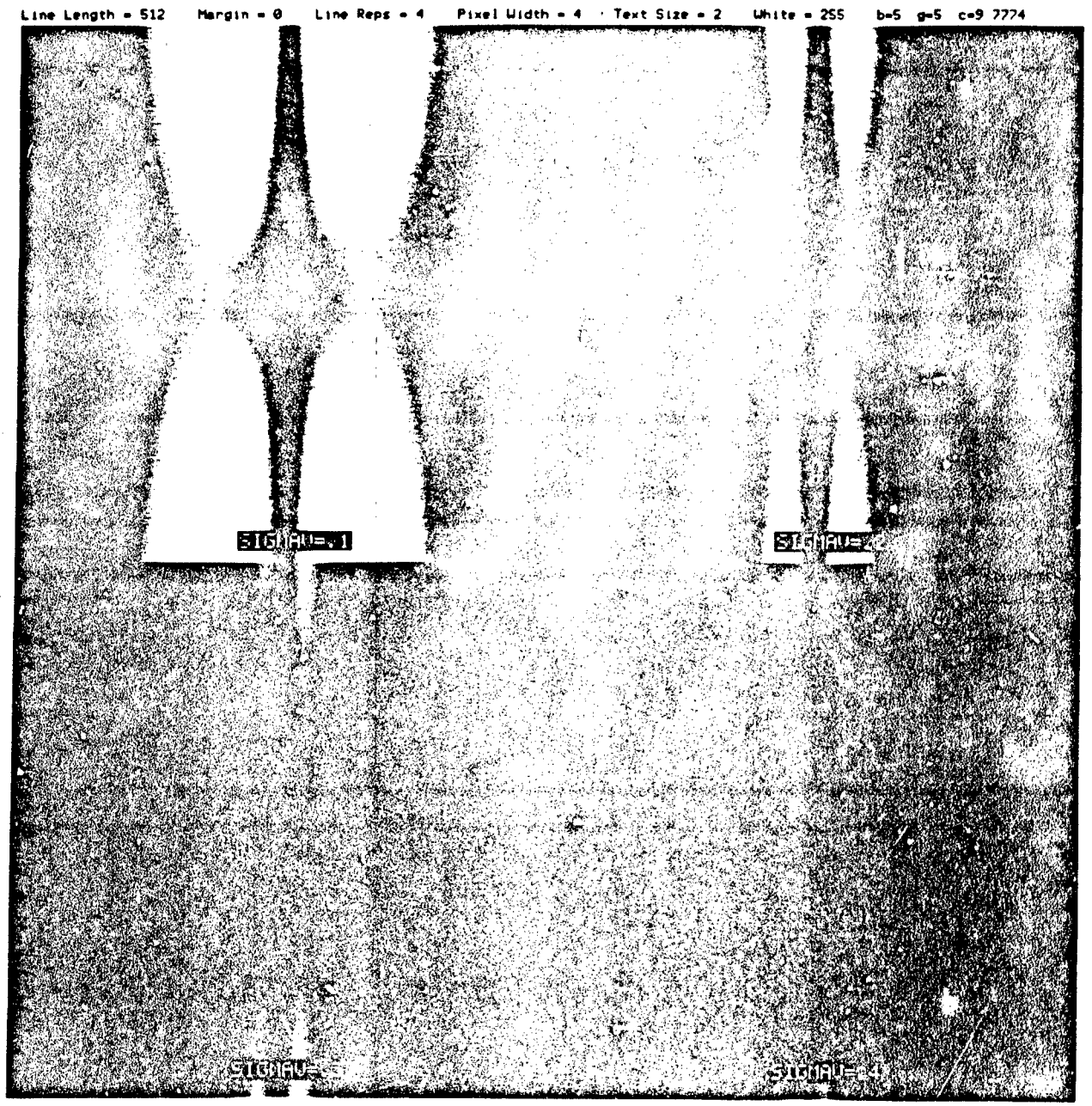

Figure 4-26. SAR Modulation Transfer Functions for Four Values of r.m.s. Surface Velocity

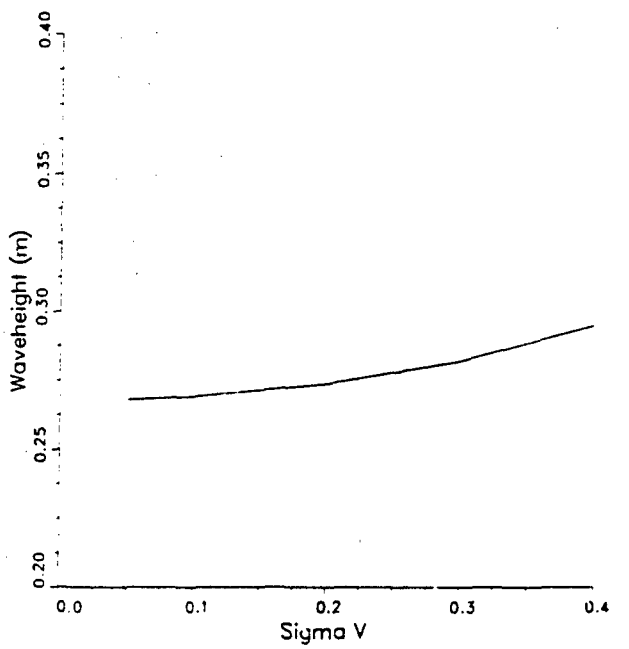

Figure 4-27. Estimated Waveheight Versus Assumed Value of r.m.s. Surface Velocity

Imagery of these areas are shown in Figures 3-3 through 3-6. Subsets of this imagery taken around the wake feature were used for analysis. The algorithm described above was applied to these data sets and the results follow.

Figure 4-28 contains the intensity image, resulting spectrum, and calculated waveheight image for DDG Run 4-1 (X-Band VV) which is the near-shore wake image. The hourglass shape of the Kelvin wake spectral response is clearly visisble. Because the value of σ_v is unknown, waveheight estimates are calculated for two values of σ_v which bracket a reasonable value for this parameter, σ_v=0.2 m/s and σ_v=0.4 m/s. Figure 4-29 contains waveheight measurements for DDG Run 4-1 (X-VV) for both the Port and Starboard Arms along the cusp of the wake at both σ_v values. There is a significant difference in the measured waveheight for these different values of σ_v. At σ_v=.2 m/s the peak waveheight for both arms of the wake is about 0.2 meters while this value is about .5 meters for σ_v=.4 m/s. Note the amplitude falls off with increased distance behind the wake along this cut. The corresponding L-Band imagery and scans are shown in figures 4-30 and 4-31 respectively. The measured L-band waveheight is smaller than that of X-band with the peak waveheights being about 0.1 meters for σ_v=.2 m/s and about 0.4 meters for σ_v=.4 m/s. Note that for the L-band data, the values are not the same for both the port and starboard arms. This asymmetry may be due to a difference in surface conditions (sea state) between the two areas.

Figure 4-32 contains the intensity image, resulting spectrum, and calculated waveheight image for DDG Run 7-4 (X-Band VV) which is the open-water azimuth traveling wake image. The Kelvin wake is less pronounced than in Run 4-1 but is still clearly visible. Scans of the X-band waveheight are shown in figure 4-33 for the two values of σ_v. The measurements show a peak waveheight of about 0.15 meters for σ_v=.2 m/s and 0.2 meters for σ_v=.4 m/s. The difference between these values and those for Run 4-1 may be due to sea state effects. The corresponding L-band

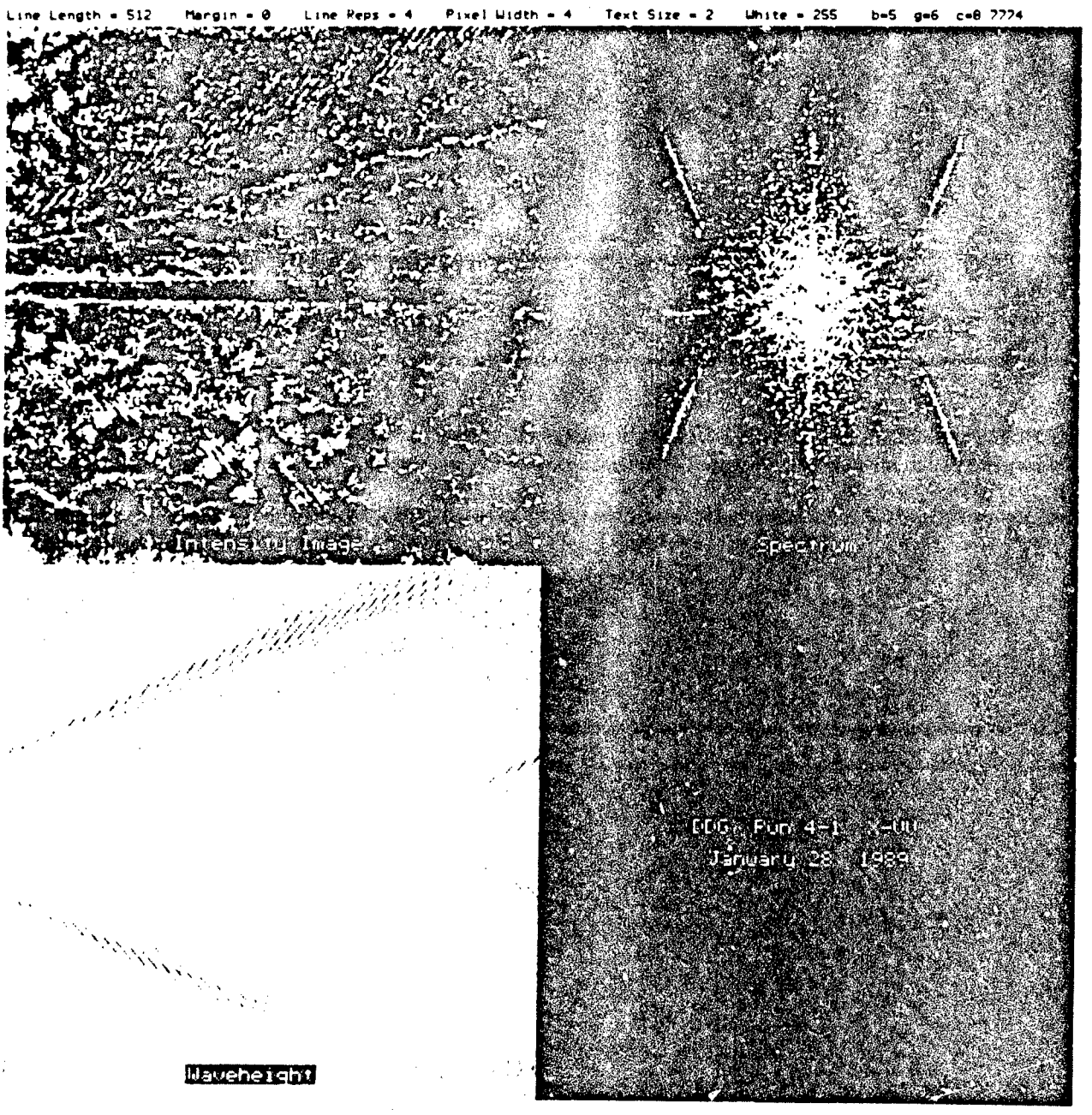

91-12085

Figure 4-28. (a) Image Subset (b) Image Spectrum, and (c) Waveheight Image for Run 4-1, X-VV

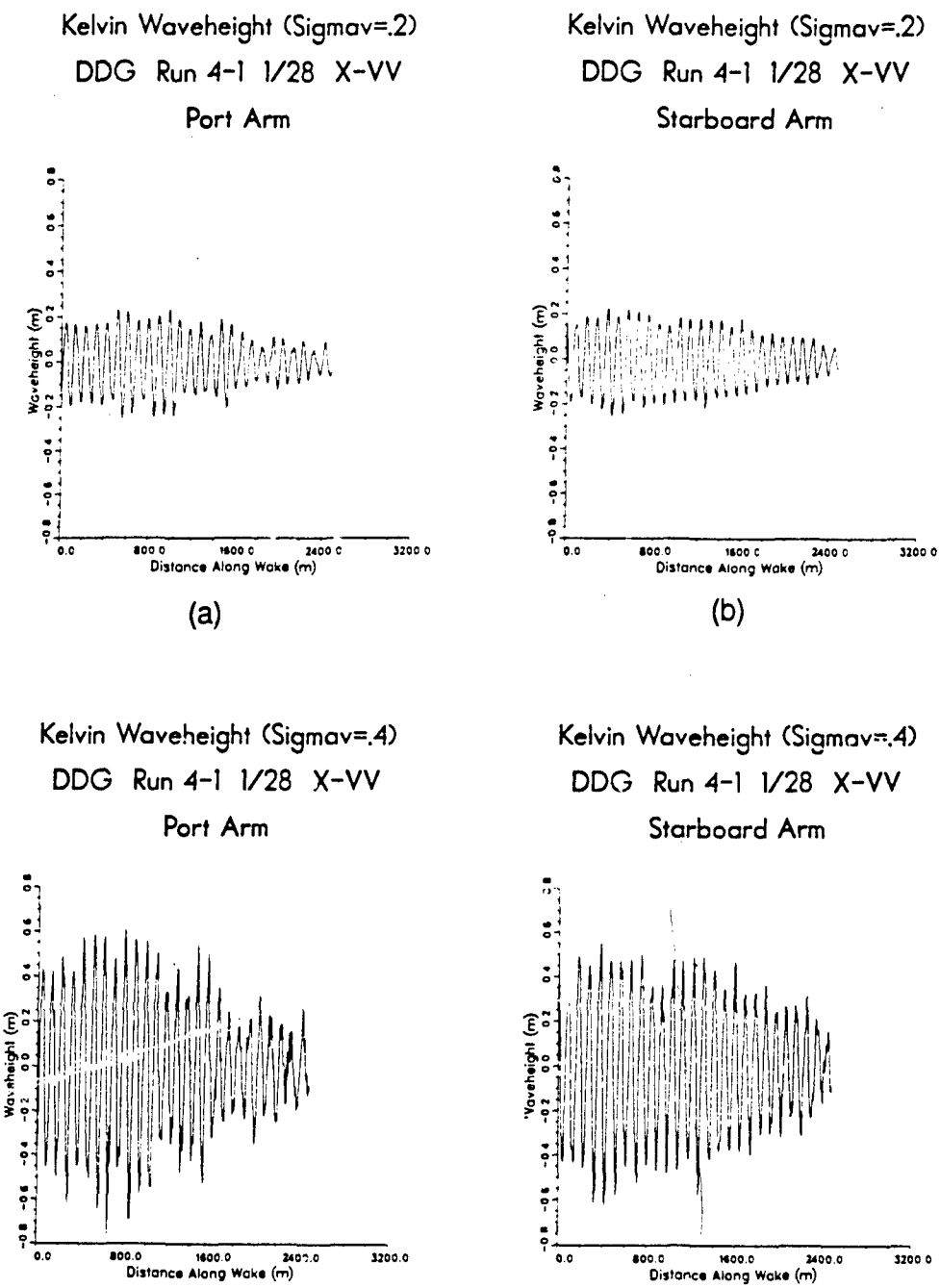

Figure 4-29. Kelvin Waveheight Estimates for Cusp Waves Along Port and Starboard Arms for Pass 4-1 Using σ_v = 0.2 m/s and 0.4 m/s

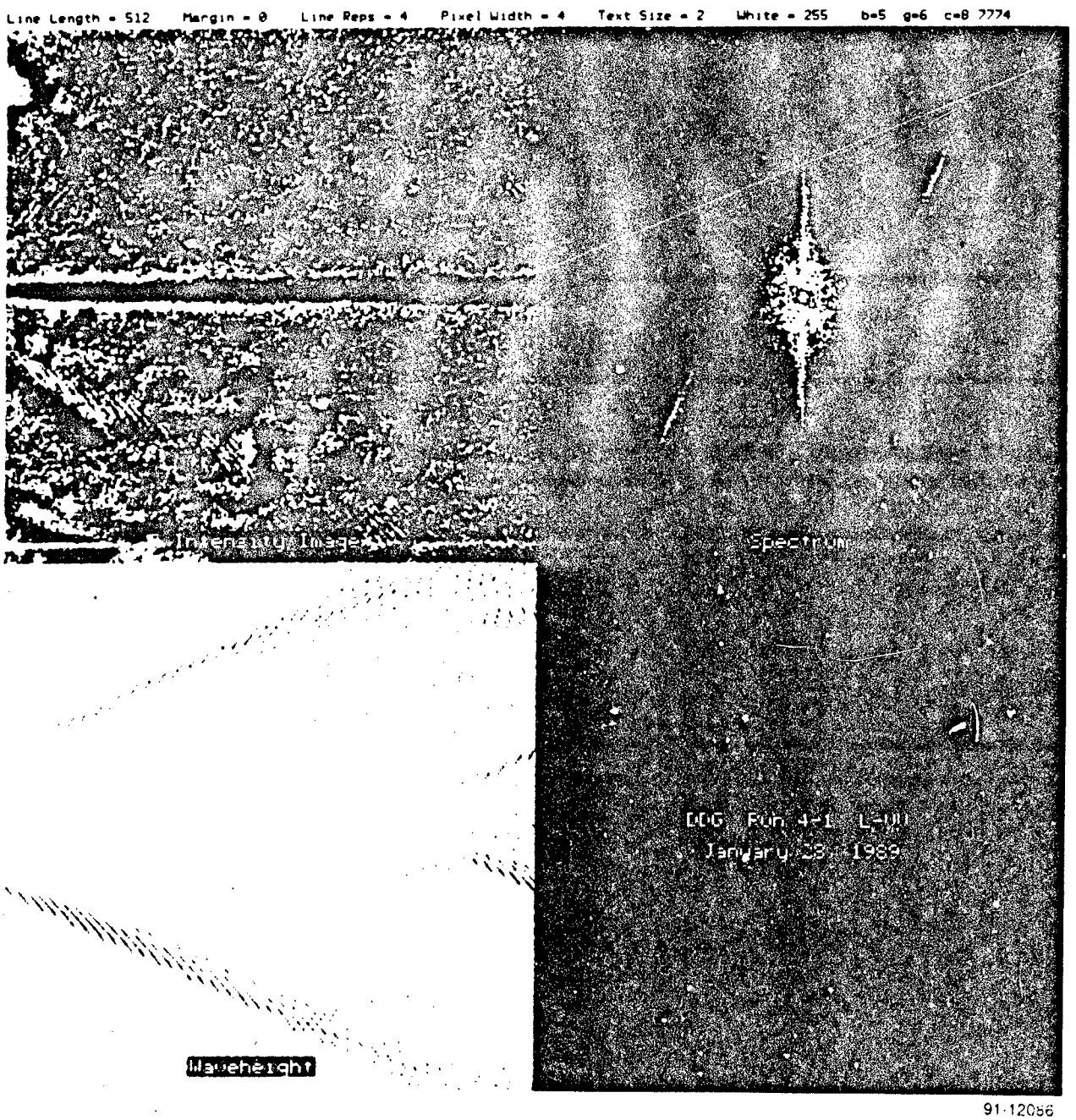

Figure 4-30. (a) Image Subset, (b) Image Spectrum, and (c) Kelvin Waveheight Image for Run 4-1, L-VV

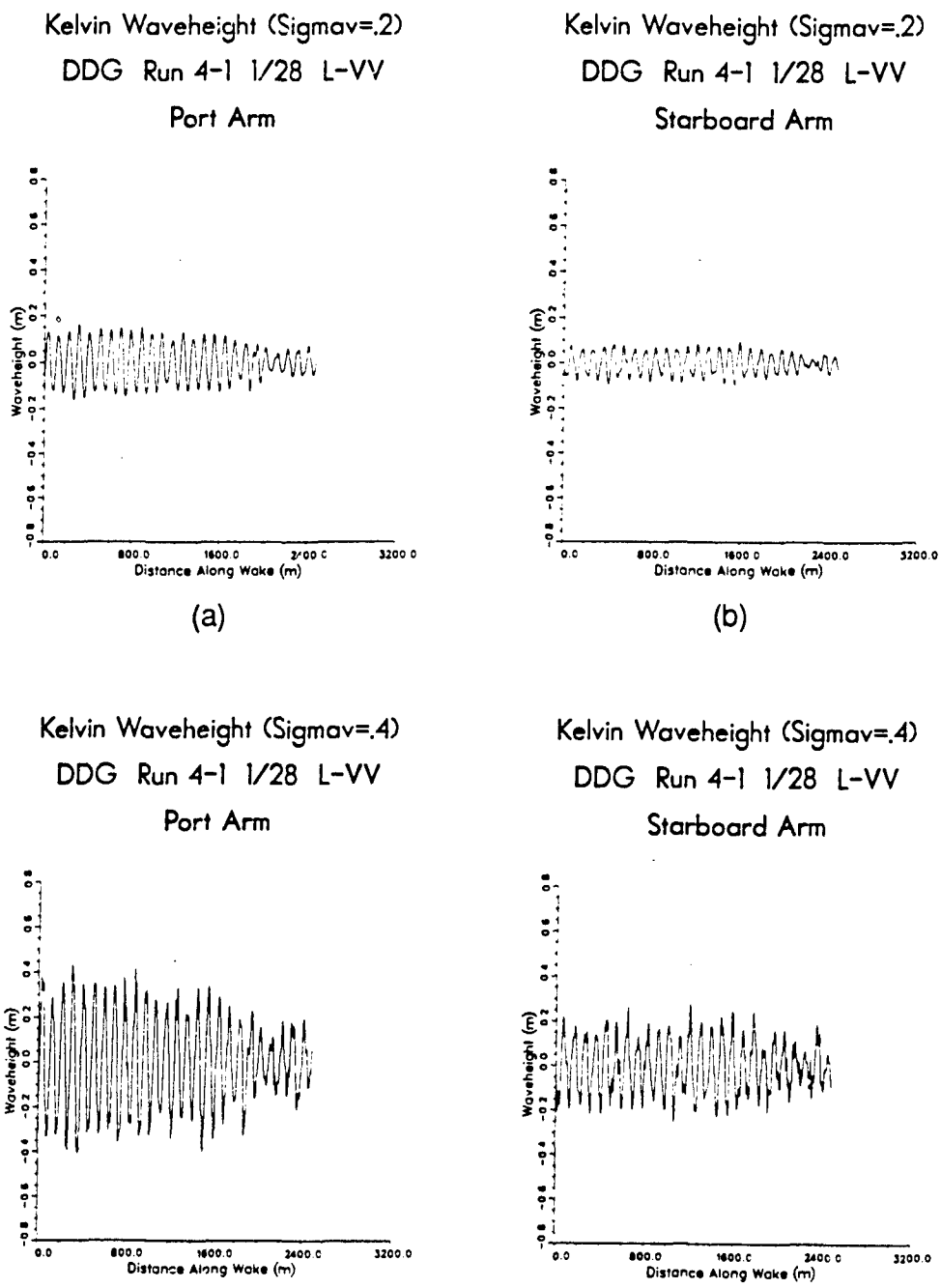

Figure 4-31. Kelvin Waveheight Estimates for Cusp Waves Along Port and Starboard Arms for Pass 4-1 Using σ_v = 0.2 m/s and 0.4 m/s

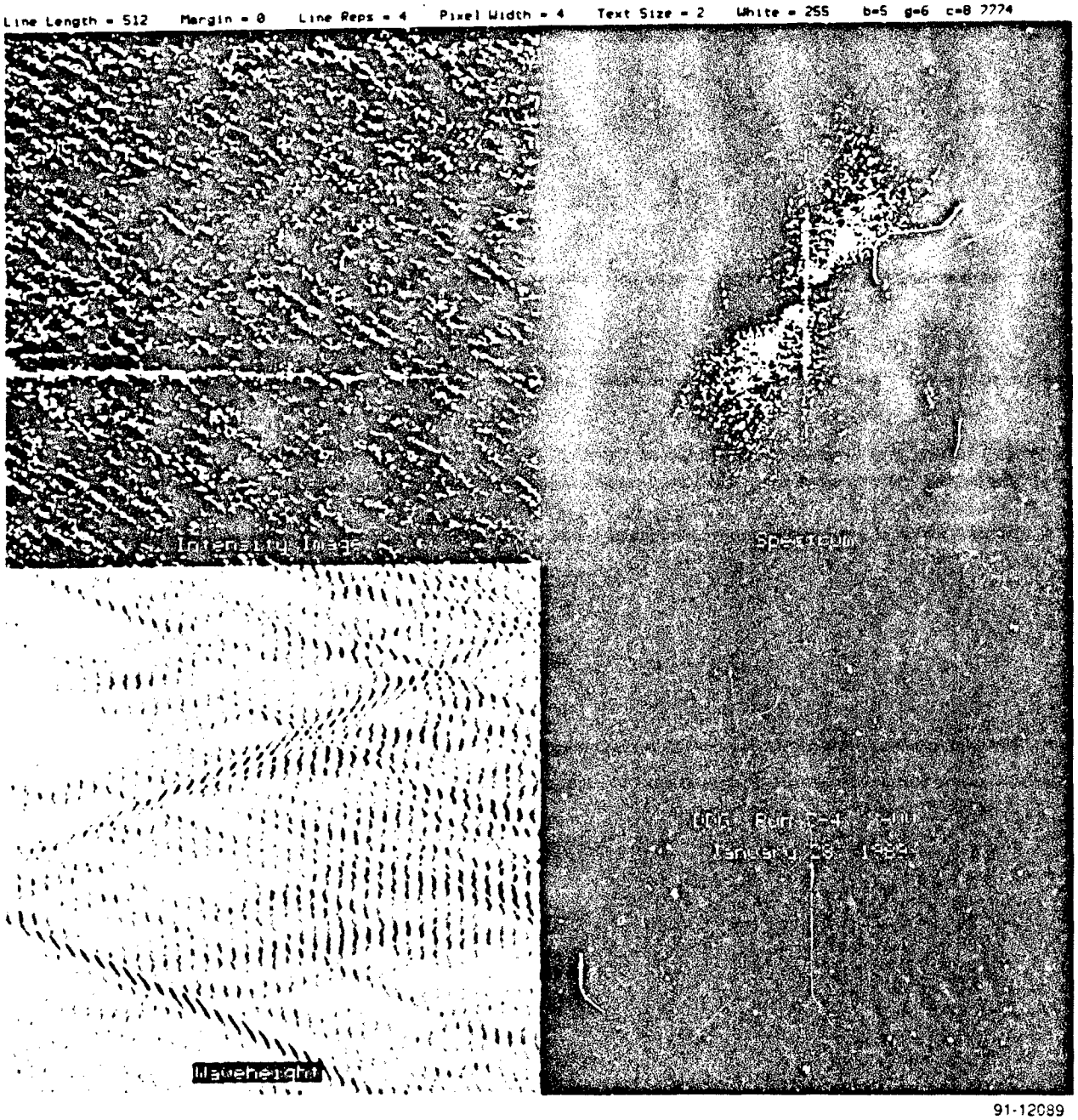

Figure 4-32. (a) Image Subset, (b) Image Spectrum, and (c) Kelvin Waveheight Image for Run 7-4, X-VV

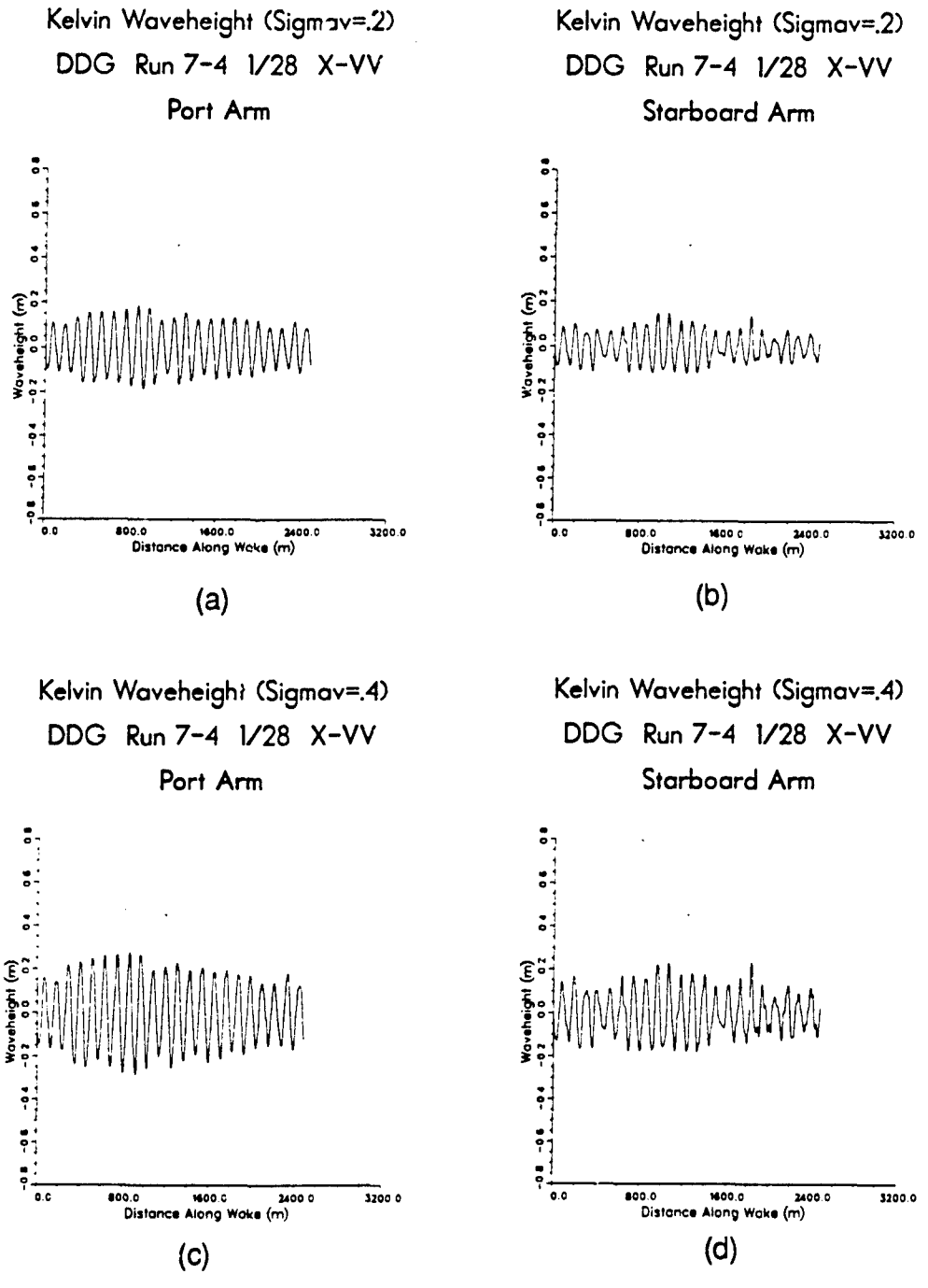

Figure 4-33. Kelvin Waveheight Estimates for Cusp Waves Along Port and Starboard Arms for Pass 7-4 Using σ_v = 0.2 m/s and 0.4 m/s

results are shown in figures 4-34 and 4-35 which show the same characteristics as the X-band data.

Figures 4-36 and 4-38 contain the intensity image, resulting spectrum, and calculated waveheight image for DDG Run 7-2 (X-Band VV and L-Band VV respectively) which is the open-water range-traveling wake image. Scans of the calculated waveheight are shown in figures 4-37 and 4-39 for both the X-band and L-band data sets for σ_v=.2 m/s only. These figures show the peak waveheight to be about .15 m for X-band data and about .10 m for L-band data along the cusp although waveheights as large as 0.3 m are measured for the stern wave component directly behind the ship. Because of the SAR MTF effects, the predominant Kelvin wake component is the transverse component which leads to relatively more wake energy in the stern wave component.

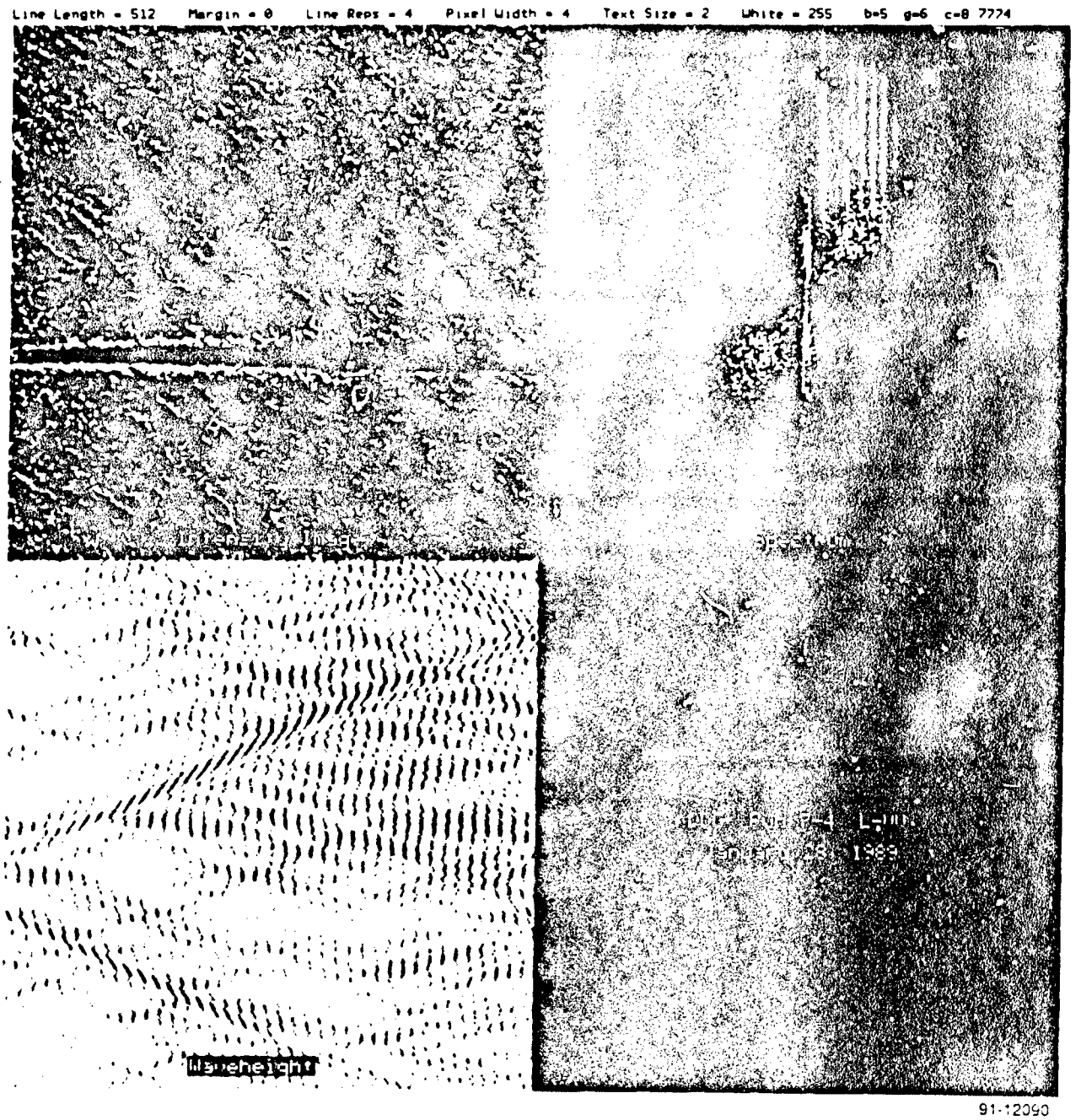

Figure 4-34. (a) Image Subset, (b) Image Spectrum, and (c) Kelvin Waveheight Image for Run 7-4, L-VV

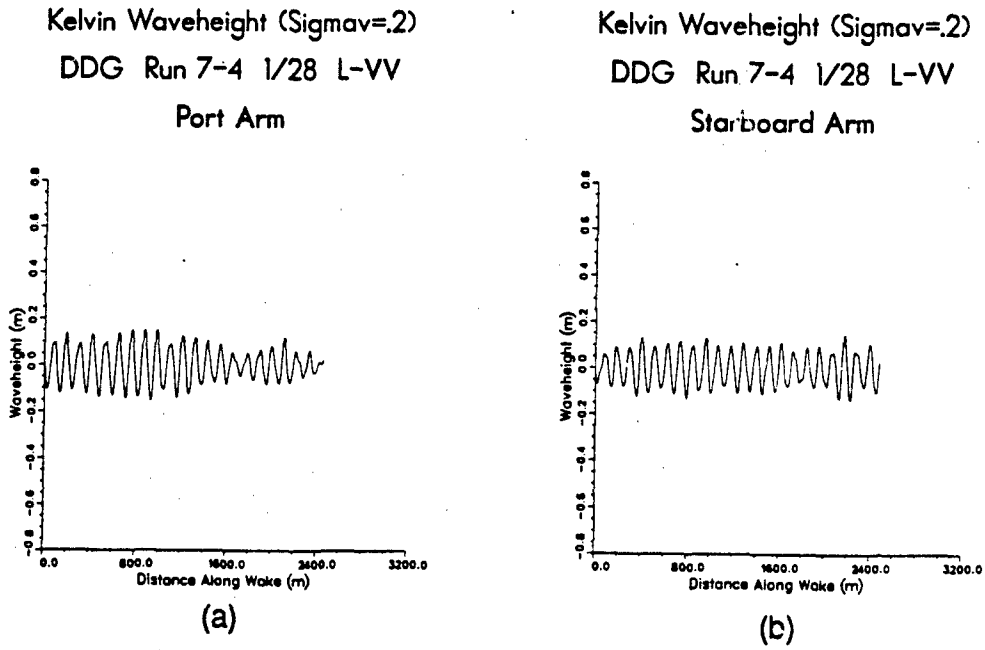

Figure 4-35. Kelvin Waveheight Estimates for Cusp Waves Along Port and Starboard Arms for Pass 7-4 Using σ_v = 0.2 m/s and 0.4 m/s

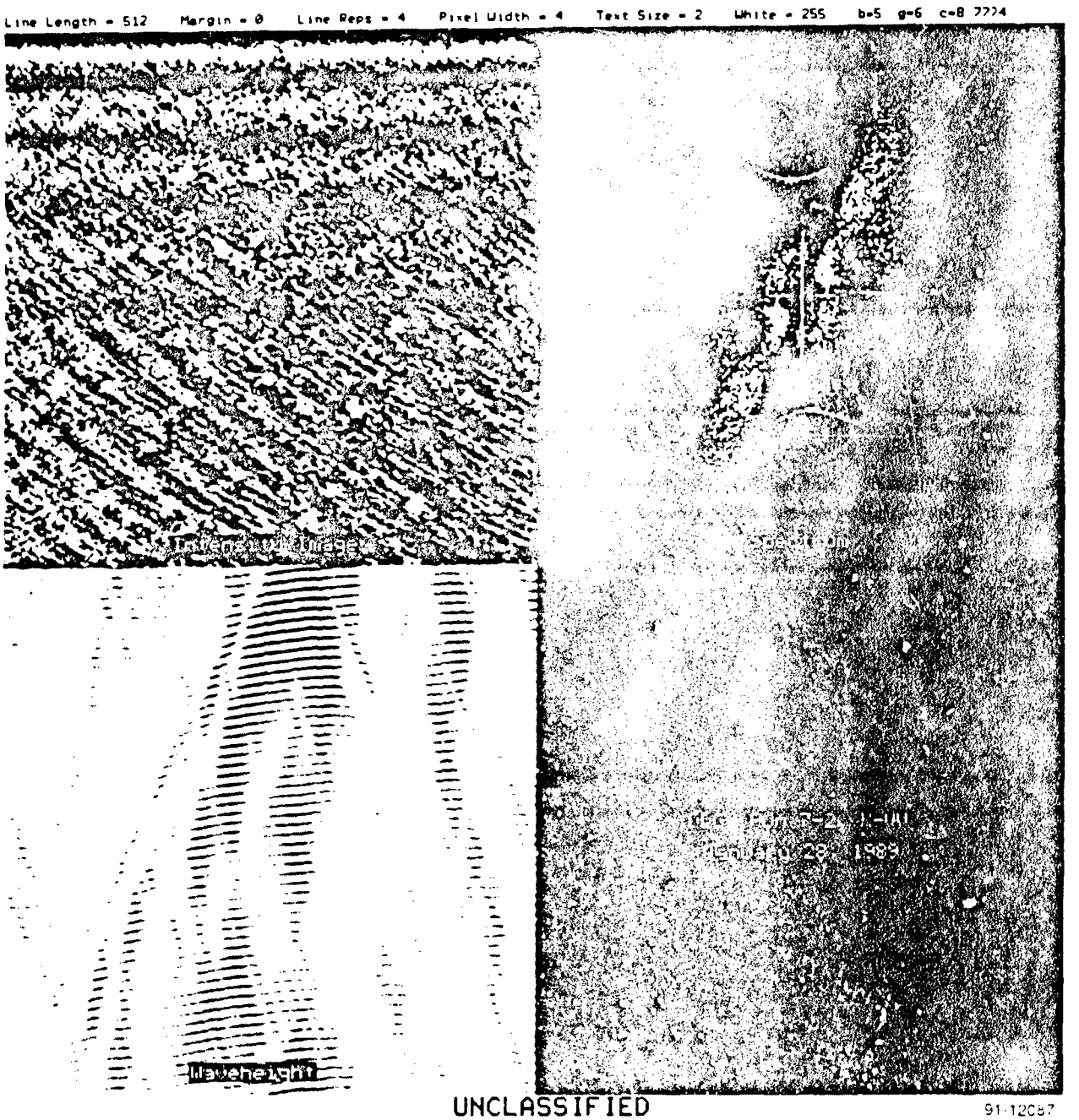

Figure 4-36. (a) Image Subset, (b) Image Spectrum, and (c) Kelvin Waveheight Image for Run 7-2, X-VV

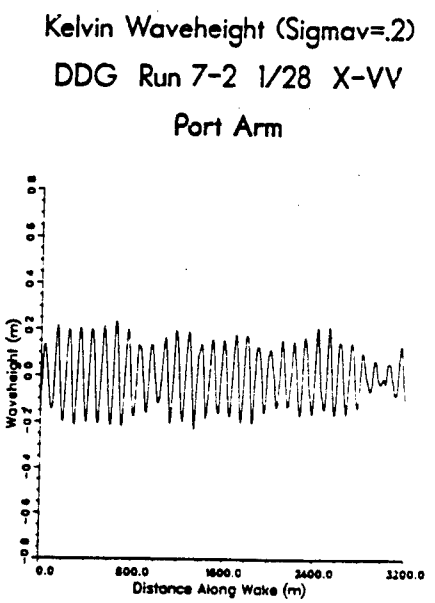

(a)

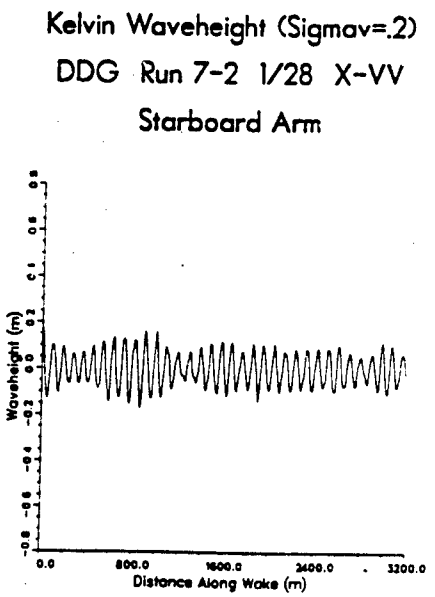

(b)

Figure 4-37. Kelvin Waveheight Estimates for Cusp Waves Along Port and Starboard Arms for Run 7-2, X-VV Using σ_v = 0.2 m/s and 0.4 m/s

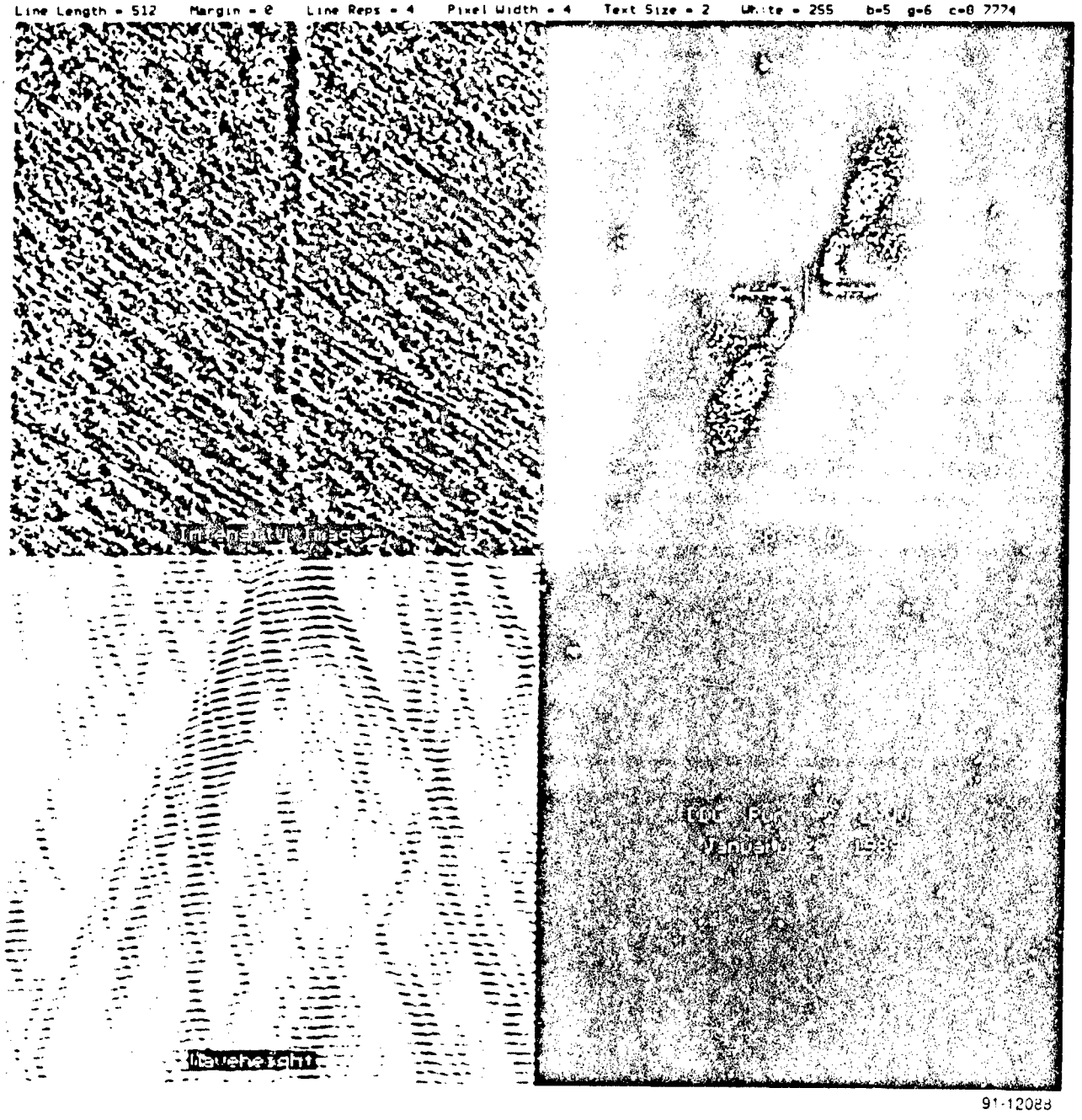

Figure 4-38. (a) Image Subset, (b) Image Spectrum, and (c) Kelvin Waveheight Image for Run 7-2, L-VV

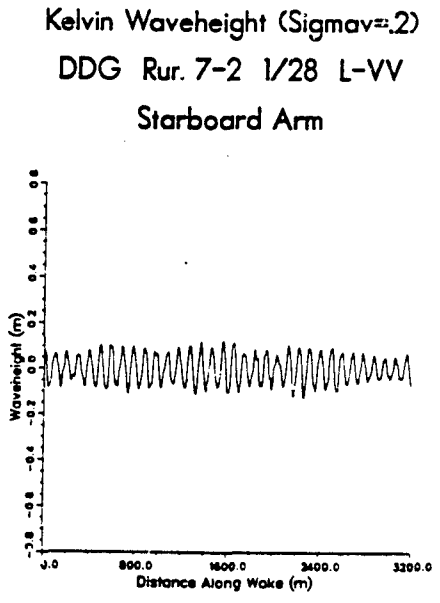

(a)

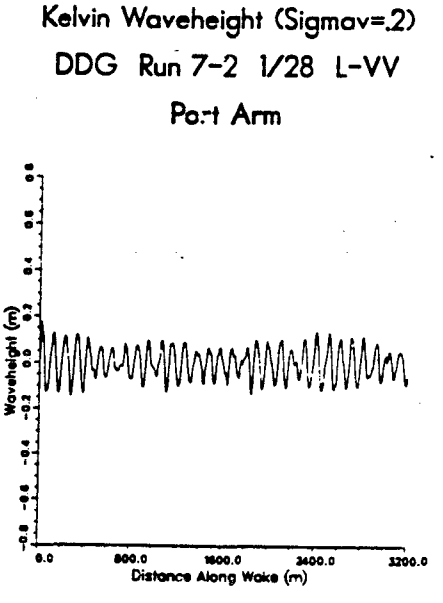

(b)

Figure 4-39. Kelvin Waveheight Estimates for Cusp Waves Along Port and Starboard Arms for Pass 7-2 Using σ_v = 0.2 m/s and 0.4 m/s

5.0 SUMMARY AND CONCLUSIONS

The dependence of the SAR modulation transfer function on azimuth angle and polarization was investigated by examining ocean wave image spectra extracted from collected imagery and by modeling the corresponding image spectra. Good agreement was observed between the empirical and modeled spectra although some differences were observed near the range wavenumber axis, probably due to errors in the hydrodynamic modulation transfer function. The close correspondence suggests that the model of the SAR modulation transfer function summarized in section 2.1 is reasonably accurate for the conditions under which this data was collected.

The success of the modeling effort also encouraged us to attempt an estimation of the wave height field for both ambient and Kelvin wake waves. The ambient wave height estimates were in good agreement with measured wave heights. Although no measurements of the DDG Kelvin wave heights were available for comparison, the values estimated from the SAR imagery were felt to be reasonable. However, it should be noted that the estimated values were in some cases quite sensitive to the assumed value of the surface radial velocity variance. Since this parameter is not well known, this leads to a significant uncertainty in the wave height estimates for some viewing geometries.

6.0 REFERENCES

Bruning, C., W. Alpers, L.F. Zambresky and D.G. Tilley, Validation of a Synthetic Aperture Radar Ocean Wave Imaging Theory by the Shuttle Imaging Radar-B Experiment Over the North Sea, J. Geophys. Res., vol. 93, pp. 15403-15425, 1988.

Chapman, R.D., ONR Ship Wake Experiment Operations Summary, Johns Hopkins University Applied Physics Laboratory Report No. STD-N-609, February 1989.

Gasparovic, R.F. and W.R. Drummond, Meteorological Data Summary ONR Ship Wake Experiment, Johns Hopkins University Applied Physics Laboratory Report No. STD-N-639, September 1989.

Gasparovic, R.F., ONR Ship Wake Experiment Wave Data Report, Johns Hopkins University Applied Physics Laboratory Report No. STD-N-658, September 1989.

Cordey, R.A. and J.T. Macklin, Complex SAR Imagery and Speckle Filtering For Wave Imaging, IEEE Trans. Geosci. Remote Sensing, vol GE-27, pp. 666-673, 1989.

Lyzenga, D.R., Numerical simulation of synthetic aperture radar image spectra for ocean waves, IEEE Trans. Geosci. Remote Sensing, vol GE-24, pp. 863-872, 1986.

Lyzenga, D.R., An analytical representation of the synthetic aperture radar image spectrum for ocean waves, J. Geophys. Res., vol 93, pp. 13859-13865, 1988.

Oliver, C.J., The interpretation and simulation of clutter textures in coherent images, Inverse Problems, vol. 2, pp 481-518, 1986.

Reed, I.S., On a moment theorem for complex gaussian processes, IRE Trans. Information Theory, pp. 194-195, 1962.

Rotheram, S. and J. T. Macklin, Inverse methods for ocean wave imaging by SAR, in Inverse Methods in Electromagnetic Imaging, Part 2, W.- M. Boerner (ed.), D. Reidel Publishing Co., pp 907-930, 1985.

Schuler, D.L., W.J. Plant, A.B. Reeves, and W.P. Eng, Removal of clutter background limitations in dual-frequency scattering from the ocean, Int. J. Remote Sensing, vol 6, pp. 1091-1112, 1985.

6.0 REFERENCES (Continued)

Sullivan, R., A. Nichols, R. Rawson, C. Haney, F. Darreff, and J. Schanne, Jr., Polarimetric X/L/C-band SAR, Proceedings of the 1988 National Radar Conference, Ann Arbor, MI, pp. 9-14, 1988.

Tricker, R.A.R., Bores, Breakers, Waves and Wakes, American Elsevier Publ. Co., 1964.